

UTRECHT UNIVERSITY
INSTITUTE FOR THEORETICAL PHYSICS

TOPOLOGY OF WEYL SEMIMETALS
with non-orientable Brillouin zones

by

Thijs DOUWES

A THESIS

Submitted to the Department of Physics
in partial fulfilment of the requirements
for the degree of

Master of Science

under the joint supervision of

First supervisor

Prof. Cristiane MORAIS SMITH
Department of Physics

Daily supervisor

Dr. Marcus STÅLHAMMAR
Department of Physics

Second supervisor

Dr. Lars FRITZ
Department of Physics

June 2025

Acknowledgements

More than just being the result of a year of research, this thesis marks the end of a twenty-six year winding road through the education system, ten of which have been spent at this university. I have had a lot to learn besides just physics, and I could not be prouder of how far I have come; this document stands as a testament to that. It is my great pleasure to use this space to extend gratitude to all those who have been with me through this phase of my life.

First of all, a name on the front cover does not begin to do justice to the positive impact that Cristiane and Marcus have had on my personal growth and well-being over the past year. I could not have asked for a more understanding and encouraging duo of supervisors. Cris, you went to great lengths this year to invest additional time and energy in me, despite having so little time to spare. Your uncompromising faith in the ability of others is an inspiration, and it has had a contagious effect on me. I never felt like you doubted me for a moment, even when I had nothing to show for it—and look how I proved you right.

Marcus, I may not have been the most straightforward first student to supervise, but I have a lot of respect for the way you handled things. Your willingness to normalise and prioritise mental health over work when needed has been a great encouragement; this year might have looked very different for me if I had not felt comfortable opening up to you in the first months. In the moments when we did get around to discussing the content, you always had insightful comments, and I think back fondly to us geeking out over cool topology together.

The rest of the research group has also been like a warm blanket (we still use the one we won at Sinterklaas!). I may not have interacted with all of you as much as I would have liked, but I really appreciated the sense of friendship and support in the group. I especially thank Lumen and Anouar for some insightful discussions, and Robin for being a great example and taking the time to chat about neurodivergence.

Outside of the studies, more people have impacted my life than I can reasonably find the space to thank here. The family and in-laws who never stopped believing in me; the friends who lent me their ears, kept me close to Christ and distracted me with board games; my therapist André and all those in my support group who have encouraged me to grow—you all know who you are, and I could not have done this without you.

Finally, my greatest thanks go out to my wife and favourite human being Annemarijn, to whom it is my absolute pleasure to dedicate this thesis. Your love and support have been unwavering, even through the hardest years of my life, and words can never adequately express how much I appreciate you.

Abstract

Weyl semimetals (WSMs) are a class of 3D materials that feature point-like band crossings in momentum space. These crossings are called Weyl points, since they represent Weyl fermion-like chiral modes in the material. In a generic WSM, the so-called Nielsen–Ninomiya theorem restricts the chiralities of these Weyl points to add to zero on the momentum space unit cell—commonly referred to as the Brillouin zone. This cancellation prevents global chiral anomalies from appearing in a material.

However, recent work indicates that the Nielsen–Ninomiya theorem is circumvented when the Brillouin zone is non-orientable—a condition which can be physically realised under certain symmetries. For example, two isolated Weyl points with the same charge may appear in this scenario.

The aim of this thesis is to shed light on this and other features of non-orientable WSMs. We do this by extending an existing algebraic topology framework, which studies WSMs in terms of cohomology and homology, to the non-orientable case. This allows the physics of these systems to be studied in a more rigorous, coordinate-free setting. In particular, we are able to pinpoint the mechanism behind the circumvention of the Nielsen–Ninomiya theorem and assess its physical consequences. In addition to this, we generalise the setting to previously unstudied non-orientable Brillouin zones and other forms of orientation-reversing symmetry.

Contents

1	Introduction	1
1.1	Setting	2
1.2	Research questions	3
1.3	Outline	3
2	Prerequisites	5
2.1	Concepts in condensed matter	5
2.1.1	Core assumptions	5
2.1.2	Berry phase	7
2.2	Homology and cohomology	9
2.2.1	Homology	10
2.2.2	Cohomology	14
3	Topological states of matter & symmetries	17
3.1	The Su–Schrieffer–Heeger model	18
3.2	The tenfold way of topological matter	24
3.3	Higher-dimensional examples	27
3.3.1	The Chern insulator	27
3.3.2	Quantum spin Hall effect	29
3.3.3	3D strong and weak insulators	29
4	Weyl semimetals	31
4.1	Physical aspects	32
4.1.1	Weyl points	32
4.1.2	Global features	35
4.1.3	Semimetals with symmetries	36
4.2	Topological description	38
4.2.1	3D Chern insulators	38
4.2.2	Topology with Weyl points	41
4.2.3	The semimetal Mayer–Vietoris sequence	46
4.2.4	Time-reversal symmetric Weyl semimetals	49

5 Non-orientability and Weyl points	53
5.1 Review of recent literature	54
5.1.1 Non-orientable Weyl semimetals	56
5.2 Topological exploration	60
5.2.1 Preliminary clarifications	61
5.2.2 Classification scheme	64
5.2.3 Computation of invariants on $K^2 \times S^1$	69
5.2.4 Classification of K^2 surface states	76
5.3 Other non-orientable Brillouin zones	79
5.4 Inversion-symmetric semimetal topology	83
5.4.1 Existing insulating classifications	83
5.4.2 Semimetal classification ansatz	85
6 Conclusions and outlook	91
6.1 Summary of main results	91
6.2 Research recommendations	93

Chapter 1

Introduction

The goal of the mathematical field of topology is to identify properties of systems which are invariant to continuous deformations. Its applications to theoretical physics have traditionally been limited to high-energy physics [1], but interest in topological condensed-matter physics has surged in recent decades. Beginning with the discovery of the integer quantum Hall effect in 1980—for which Klaus von Klitzing was awarded the Nobel Prize in Physics [2]—it was realised that states of matter exist which are electrically insulating in the bulk, but which cannot be continuously transformed into a conventional insulator; see Figure 1.1. These features have turned out to be well described using tools from topology, earning such materials the name of topological insulators.

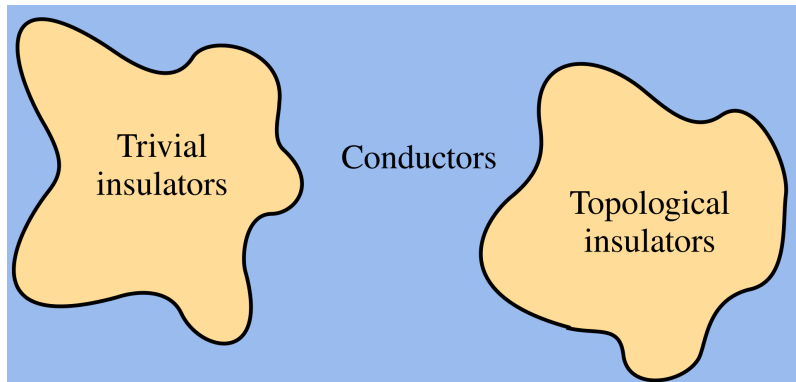


Figure 1.1: Schematic phase diagram showing how different types of materials relate. Topological insulators occupy a separate region in phase space from regular insulators, meaning that a Hamiltonian associated with either one cannot be continuously transformed to that of the other without describing a conductor at some intermediate point.

Topological insulators have been shown to be a naturally occurring phenomenon [3, 4], and they are host to many interesting properties. Perhaps the most distinctive of these properties is the existence of boundary currents: because a topological insulator cannot be continuously connected to a normal insulating state such as the vacuum, conducting states are forced to appear on its interface. These states are protected by the topology of the system, which makes them highly robust to disorder

in many cases—a property which may prove to be valuable in applications such as quantum computing, where sensitivity to disorder is one of the main challenges to overcome.

Since the discovery of topological insulators, the study of topology in matter has become an active and rapidly evolving field, eliciting another shared Nobel Prize in Physics as recently as 2016 [5]. Its realm of applicability has been extended to superconductors [6], semimetals [7] and even fully conducting states in metals [8]. It is the semimetals that we are concerned with in this work; these are materials in which the conducting states disperse around certain specific momenta.

1.1 Setting

The main focus of this thesis is on a three-dimensional class of materials called Weyl semimetals, in which the conducting modes resemble the chiral fermions described by Hermann Weyl in 1929 [9]. The study of these materials is a relatively recent development, with the name first being coined in 2011 [10]. Weyl semimetals have since been experimentally realised starting in 2015 [11–14], and they have been found to have exotic transport properties which may have useful applications [15–17].

The chirality associated with left-handed and right-handed Weyl fermions manifests itself as a topological feature in Weyl semimetals: the momenta at which these Weyl modes appear—the so-called Weyl points—have a topological charge associated with them which determines their chirality. Similar to the way in which one left-handed and one right-handed Weyl fermion are paired in the description of a Dirac fermion, the charges in a Weyl semimetal are subject to a cancellation condition known as the Nielsen–Ninomiya theorem [18, 19]. Concretely, this theorem acts on the unit cell of the momentum-space reciprocal lattice, known as the Brillouin zone: the statement is that the total chirality of all Weyl points in the Brillouin zone should add up to zero. One physical manifestation of this comes in the form of Fermi arcs, which are conducting surface states that connect the projections of oppositely charged Weyl points; see Figure 1.2.

However, recent works have begun to explore materials in which the presence of certain symmetries forces the Brillouin zone to become non-orientable [21–24]. Non-orientability is a topological property which implies that there is no longer an inherent sense of handedness to a space. A 2024 paper by André Grossi Fonseca, Sachin Vaidya et al. has explored the consequences of applying this non-orientable setting to the intrinsically chiral Weyl semimetals [25], and it is this paper that provides the main motivation for this thesis. The authors of Ref. [25] find that the Nielsen–Ninomiya theorem no longer straightforwardly applies in the non-orientable case. Instead, the total chirality on the Brillouin zone is only constrained to add to an even number, and Fermi arcs may connect Weyl points with the same chirality under certain circumstances.

However, the description given in Ref. [25] is explicitly coordinate dependent, leading to ambiguity in the physical interpretation of the results. Some confusion is also present about the way in which the circumvention of the Nielsen–Ninomiya theorem should be interpreted mathematically.

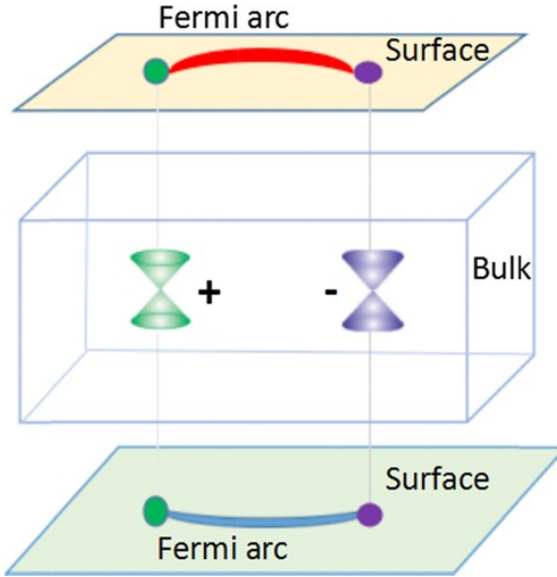


Figure 1.2: Figure from Ref. [20]. Schematic Weyl semimetal Brillouin zone featuring two oppositely charged Weyl points, whose projections on two different surfaces are shown to be connected by Fermi arcs.

1.2 Research questions

In this thesis, we aim to provide a deeper understanding of the features found in Ref. [25], both at a mathematical and at a physical level. In particular, we set out to clarify whether the lack of complete charge cancellation can give rise to any phenomenological consequences.

We achieve this by studying non-orientable Weyl semimetals in a more rigorous mathematical framework. To this end, we develop an extension of an existing description in terms of the topological tools of homology and cohomology, first introduced by Varghese Mathai and Guo Chuan Thiang [7, 26]. We study how this framework needs to be modified to account for non-orientability, and how the subsequent results differ qualitatively from the orientable setting.

From this more abstract mathematical point of view, we also examine how and to what extent the setting of non-orientable Weyl semimetals can be generalised, both to different non-orientable Brillouin zones and to more general orientation-reversing symmetries.

1.3 Outline

We offer a brief overview here of the organisation of this work. We begin in Chapter 2 by introducing some of the prerequisite physical and mathematical concepts. On the physical side, we review some basic aspects of condensed-matter physics, with an emphasis on the core assumptions used in our model. On the mathematical side, we offer a relatively low-level overview of the concepts of homology and cohomology.

Chapter 3 is a review of different gapped topological states of matter, with an emphasis on those systems which are relevant to the later description of semimetals.

Special attention is also paid to the role that symmetries play in determining the topology of a material, with the tenfold classification of symmetry classes taking centre stage.

A review of the theory of Weyl semimetals is provided in Chapter 4. The first portion of this chapter is dedicated to describing the essential physical properties of these systems, and its remainder delves into the mathematical description in terms of homology and cohomology that is given in Ref. [7].

Chapter 5 focuses on non-orientable topology, and it is this chapter that contains the bulk of our results. We begin with a review of the existing literature on non-orientable materials, culminating in a treatment of Ref. [25] on Weyl semimetals. We then spend the remainder of the chapter explicating a rigorous framework in which these systems can be studied, and exploring some of the consequences of this description. This part of the work is original.

Finally, the main conclusions of our research are summarised in Chapter 6, and some recommendations for further avenues of research are given.

Chapter 2

Prerequisites

In this chapter, we briefly review some of the more fundamental concepts on which the rest of this work is built. Section 2.1 covers some essentials of condensed matter physics, to the degree that is necessary here; in particular, some of the key assumptions underlying our description are highlighted, and the significance of the Brillouin zone and the Berry phase are explained. Section 2.2 provides the necessary mathematical background; in particular, the topological tools of homology and cohomology are treated. Readers who are at least somewhat familiar with the concepts in either section are free to skip over them, and refer back to their contents later as needed.

2.1 Concepts in condensed matter

We offer here a brief review of the physics of electronic materials, to the extent that is relied on in this thesis. The concepts set out here are explored in great generality in standard reference works such as Ref. [27], but we will only require a select few specialised details.

The electronic transport properties of materials can be understood in terms of the energy levels that the electronic states that inhabit them may occupy, in close analogy to the electronic orbitals in a single atom; in a material, these levels are referred to as *energy bands*. In the ground state of a material, the Pauli exclusion principle ensures that the energy bands are occupied up to a certain level, known as the Fermi energy. The manner in which electricity is (or is not) conducted in a system is then determined by the way in which the bands are organised around the Fermi energy; this is illustrated in Figure 2.1. In general, partially occupied bands give rise to mobile electron states at the Fermi energy, allowing for conduction. This is closely related to the microscopic picture in which the partially occupied outer electron orbits in metal atoms allow mutual exchange of electrons. Here, we will use the common convention of setting the Fermi energy to $E_F = 0$.

2.1.1 Core assumptions

We follow three commonly made assumptions in this work in order to make the energy band description mathematically tractable. The first is that the atomic orbitals in

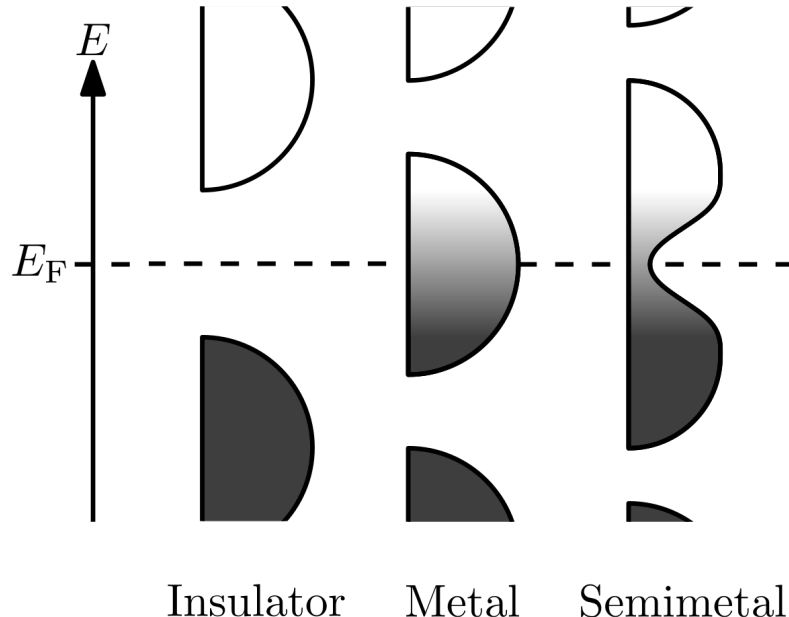


Figure 2.1: Schematic illustration of the energy bands related to different types of materials. Occupied states are indicated in grey, while unoccupied states are white. In an insulator, the Fermi energy lies between a fully occupied valence band and a fully empty conduction band. On the other hand, metals and semimetals are characterised by bands which overlap or touch at the Fermi energy, respectively. The colour gradient across the Fermi energy E_F indicates that the system is not in the ground state, and the electrons in these states are mobile.

the material do not overlap significantly between atomic sites. This is known as the *tight-binding approximation*, and it ensures that the bands exist at discrete energy levels, without being split into different ranges of energies.

The second assumption we make is that the physical properties of the systems under consideration are well approximated by just two energy bands. This is often the case in insulators and semimetals, where the Fermi energy lies between two bands: in this case, the highest occupied band is called the *valence band* and the lowest empty band is the *conduction band*.

The two-band tight-binding model allows for the system to be described by a 2×2 Hamiltonian operator. In momentum space, a 2×2 Hermitian operator takes on the generic form

$$\mathcal{H}(\mathbf{k}) = h_0(\mathbf{k})\mathbb{1} + \mathbf{h}(\mathbf{k}) \cdot \boldsymbol{\sigma}, \quad (2.1)$$

where $\boldsymbol{\sigma} = (\sigma_x, \sigma_y, \sigma_z)^\top$ is the vector of Pauli matrices, and the number of components in \mathbf{k} depends on the dimensionality of the material. In practice, the trace term parametrised by h_0 turns out to not affect the topology of the bands, and as such we will often assume $h_0(\mathbf{k}) = 0$.

The actual energy bands are now the eigenvalues of this Hamiltonian,

$$E(\mathbf{k}) = h_0(\mathbf{k}) \pm |\mathbf{h}(\mathbf{k})| = h_0(\mathbf{k}) \pm \sqrt{h_1^2(\mathbf{k}) + h_2^2(\mathbf{k}) + h_3^2(\mathbf{k})}.$$

It follows that the two bands only touch when $\mathbf{h}(\mathbf{k}) = 0$. Under the assumption that $h_0(\mathbf{k}) = 0$, this means that the system is insulating whenever $\mathbf{h}(\mathbf{k})$ is non-zero.

The final key assumption that we adhere to is that the materials under consideration are crystalline, i.e. that they are described by a periodic lattice. In this context, a result known as *Bloch's theorem* applies [28], which tells us that the real-space eigenstates $\psi(\mathbf{r})$ of any Hamiltonian can be expressed in terms of plane waves and periodic functions:

$$\psi(\mathbf{r}) = e^{i\mathbf{k}\cdot\mathbf{r}} u(\mathbf{r}),$$

where $u(\mathbf{r})$ respects the periodicity of the lattice. Consequently, different momenta \mathbf{k} can describe the same eigenstate $\psi(\mathbf{r})$, as long as the resulting values of $\mathbf{k} \cdot \mathbf{r}$ differ by a multiple of 2π . As a result, there is a bounded region of momentum space containing only momenta which correspond to distinct eigenstates $\psi(\mathbf{r})$. This region is referred to as the *Brillouin zone*, and it is precisely the unit cell of the reciprocal lattice; see Figure 2.2.

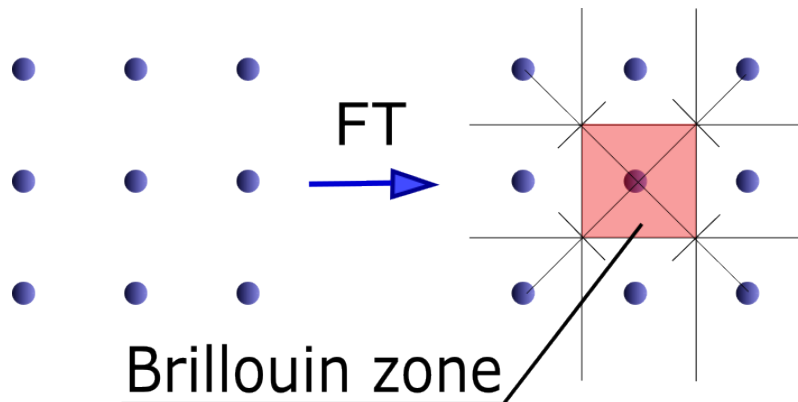


Figure 2.2: Figure by Gang65, licensed under CC BY-SA 3.0. The Fourier transform of a real-space crystal lattice (left) is a reciprocal lattice in momentum space (right). The Brillouin zone is the unit cell of this reciprocal lattice.

The boundaries of the Brillouin zone contain momenta which are separated by exactly one unit cell, and these momenta need to be identified with each other to obtain a completely unambiguous description. In d dimensions, the reciprocal lattice is periodic in d directions, so that these boundary identifications give the Brillouin zone the topology of the d -dimensional torus $\mathbb{T}^d = (S^1)^d$; see Figure 2.3. Therefore, the Hamiltonian in Equation (2.1) can be considered a function on the torus in this setting; in particular, the vector $\mathbf{h}(\mathbf{k})$ becomes a map $\mathbf{h} : \mathbb{T}^d \rightarrow \mathbb{R}^3$.

2.1.2 Berry phase

One of the most fundamental concepts in the theory of topological matter is that of the Berry phase [30]. The underlying idea is that each electronic eigenstate $\psi(\mathbf{k})$ of the Hamiltonian carries a complex phase ϕ in the electromagnetic gauge group $U(1)$

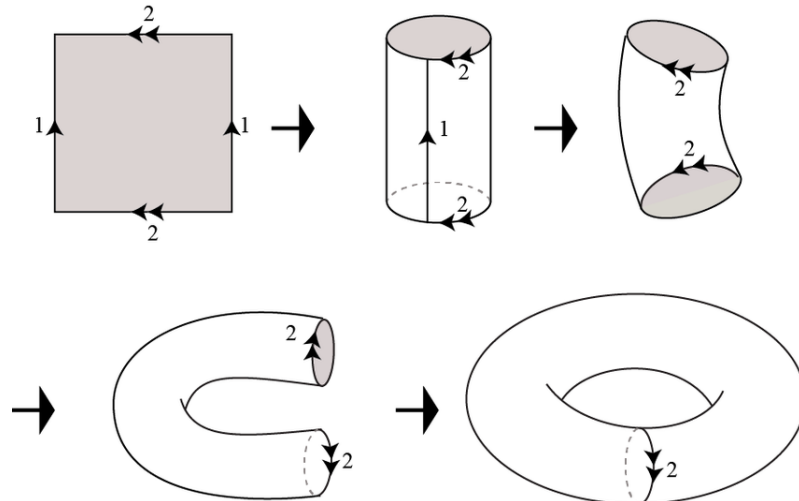


Figure 2.3: Figure from Ref. [29]. The square on the top left represents a two-dimensional Brillouin zone, with the necessary boundary identifications indicated by numbered arrows. This identification is topologically equivalent to “gluing” the boundaries together, which gives rise to the 2-torus $\mathbb{T}^2 = S^1 \times S^1$.

(i.e. the complex unit circle).¹ This phase may change as the state $\psi(\mathbf{k})$ is parallel transported across momentum space; see Figure 2.4.

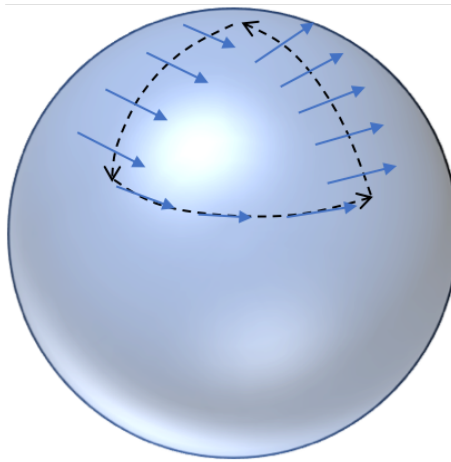


Figure 2.4: Figure from Ref. [31]. Schematic illustration of parallel transport. The complex phase ϕ of a state is represented by the blue arrows. As the state is transported along a closed loop, the phase is kept locally constant, but a non-zero Berry curvature (represented here by the curvature of a sphere) results in a net phase change.

The notion of parallel transport is perhaps most familiar in the context of general relativity: there, four-vectors may be transported across spacetime using the Levi–Civita connection. Depending on the Riemann curvature of the intervening

¹Formally, ϕ depends on the U(1) gauge used, but the relative phase change discussed later does not suffer this problem.

spacetime, the orientation of a vector may change as it is transported along a closed loop. The situation is similar for the U(1) phase of electronic states: the so-called *Berry connection* can be defined as the differential 1-form

$$\mathcal{A} = A_\mu dk^\mu = i \langle \psi(\mathbf{k}) | \partial_\mu | \psi(\mathbf{k}) \rangle.$$

Parallel transport along a line $l \subset \mathbb{T}^d$ in the Brillouin zone is then given by integration of this 1-form, and it induces a change of phase:

$$\Delta\phi = \int_l \mathcal{A}.$$

This change of phase is exactly what is known as the Berry phase.

Just as the Levi–Civita connection gives rise to Riemann curvature, there is also a *Berry curvature* associated with the Berry connection. This curvature is the differential 2-form given by the exterior derivative of the connection,²

$$\mathcal{F} = d\mathcal{A} = (\partial_\mu A_\nu - \partial_\nu A_\mu) dk^\mu dk^\nu.$$

This curvature 2-form can be integrated over any two-dimensional subspace $S \subset \mathbb{T}^d$ of the Brillouin zone, and by Stokes’ theorem, the result is a measure of the phase change around the boundary of S :

$$\int_S \mathcal{F} = \int_S d\mathcal{A} = \oint_{\partial S} \mathcal{A}.$$

This phase change along closed loops needs to be an integer multiple of 2π to ensure that the electronic states are defined consistently. This puts topological constraints on the Berry curvature, allowing it to be used to study the topology of the system.

2.2 Homology and cohomology

The concepts of homology and its dual counterpart cohomology are indispensable tools in the mathematical field of algebraic topology. While seemingly abstract from a physics point of view, many fundamental elements of the physicist’s toolbox—such as Stokes’ theorem—are formulated most naturally in the context of this theory. Additionally, there are deep results relating the cohomology of a space to the classification of different types of vector bundles over this space. Physically, this relates closely to the classification of topological phases of matter to which this work is dedicated.

Here, we offer a brief introduction to these concepts, aimed at the uninitiated physicist. The goal is not to be completely rigorous, but to give a sufficiently comprehensive understanding that the applications discussed in later chapters may be understood in their proper context. For a more complete picture, the interested reader is referred to standard texts in algebraic topology such as Refs. [32] and [33]. A more geometric treatment relying on differential forms is also found in Ref. [34].

²To be precise, the Berry curvature is *locally* defined as the exterior derivative, but \mathcal{A} may need to be defined in multiple gauges to obtain the full curvature.

The basic idea underlying homology is that information about the topology of a space M can be gained from studying non-trivial subspaces of M of various dimensions. Perhaps the simplest conceptual realisation of this idea exists in the closely related *homotopy* theory. In this theory, one defines the n th homotopy group $\pi_n(M)$ in terms of maps from the n -dimensional sphere S^n into M . For example, the first homotopy group $\pi_1(M)$ (also known as the *fundamental group*) records the topologically different ways in which loops $\gamma : S^1 \rightarrow M$ can sit inside M . If two such loops cannot be transformed continuously into each other, then they represent different elements of $\pi_1(M)$.³ This fundamental group forms the conceptual basis behind some topological invariants in physics as well, such as that of the Su–Schrieffer–Heeger model discussed in Section 3.1.

Despite their conceptual simplicity, homotopy groups can be rather unwieldy in practice: they are generally difficult to compute and may have unpredictable structures. For example, even maps from S^n to a lower-dimensional S^m with $m < n$ may be non-trivial, and calculating the associated higher homotopy groups $\pi_n(S^m)$ of the spheres is an important open problem in algebraic topology.

This is where the closely related homology enters the stage. It is conceptually somewhat more involved than homotopy, and strictly speaking it contains less information. However, there is a great payoff: homology groups are generally much easier to compute and structurally simpler than their homotopy counterparts. Moreover, homology can be dualised into cohomology, which is a construction which is both mathematically and physically very natural.

2.2.1 Homology

The basic building blocks of homology theory are oriented subspaces of a space M .⁴ Some such subspaces are illustrated for the two-dimensional torus in Figure 2.5. Topological information can be gained from these subspaces by studying their (oriented) boundaries. The goal of homology is to find subspaces such as d and e in Figure 2.5, which do not have a boundary, but cannot themselves be written as the boundary of another subset either—unlike c , for instance, which is the boundary of S . Spaces like d and e detect topological features of the space, such as the hole in the centre of the torus.

To properly define oriented boundaries, we must work in the context of so-called *n -chains*, which are linear combinations of n -dimensional subspaces of M . For example, $a + b$ is a 1-chain on the torus in Figure 2.5, as is $3a - 2c$. Using n -chains makes boundaries well-behaved under addition. For example, we may define the boundary of a as the 0-chain $\partial a = p - q$, and similarly $\partial b = q - r$; adding these up,

³These deformations may include self-intersections. In particular, this means that different knots (i.e. embeddings of S^1 in \mathbb{R}^3) cannot be distinguished by homotopy. In this context, one needs to use a form of *isotopy* instead, which does not allow self intersections as maps are deformed into each other.

⁴There are different ways of formally defining these oriented subspaces, such as mapping simplices (the n -dimensional analogue of triangles) into M or defining a so-called *cell structure* on M . Importantly, these different constructions usually give rise to the same homology groups. Therefore, we will be agnostic to the details and focus on the conceptual basis instead.

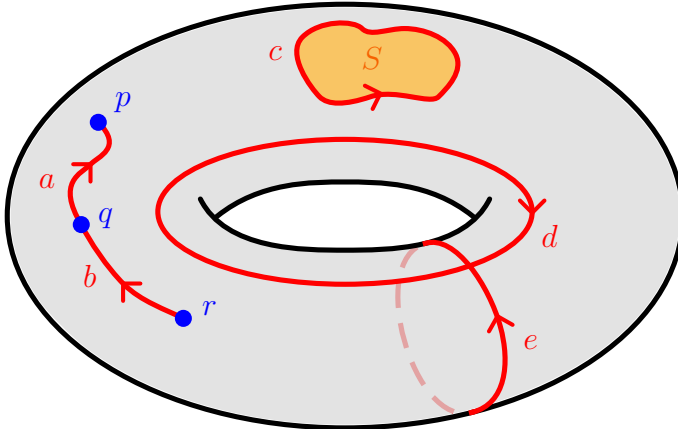


Figure 2.5: The two-torus \mathbb{T}^2 . Some of the oriented subspaces that make up chains in the homology theory are highlighted: components of 0, 1, and 2-chains are coloured blue, red and orange, respectively. The orientation of the 0D and 2D subspaces can be canonically induced from an orientation on the torus in this case.

we obtain

$$\partial a + \partial b = (p - q) + (q - r) = p - r,$$

which is precisely the boundary of the 1-chain $a + b$.

Formally, an n -chain takes the form

$$\sum_i c_i X_i,$$

where $X_i \subset M$ are oriented n -dimensional subsets of M . The coefficients c_i are usually taken to be integers in \mathbb{Z} , but they may also be e.g. real numbers, rationals or elements of \mathbb{Z}_2 ; to be precise, they must be elements of any fixed Abelian group G , which is called the *coefficient group*. A powerful result called the universal coefficient theorem implies that taking coefficients in the integers $G = \mathbb{Z}$ always results in the richest possible homology theory [32, §3.A]; this is why the coefficients are usually assumed to be elements of \mathbb{Z} unless explicitly stated otherwise.

The n -chains on M naturally form a group under addition in the coefficient group G , which we notate $C_n(M; G)$ —or simply $C_n(M)$ when $G = \mathbb{Z}$. The inverses in this group act to invert the orientation of a chain: for example, the chain $-c$ on the pictured torus looks like c with the arrow pointing in the opposite direction.

The boundary of an n -chain is always an $(n - 1)$ -chain. This is even true for $n = 0$; points have no boundary, so their boundary is the empty “ (-1) -chain” in $C_{-1}(M; G) = 0$. This means taking the boundary defines⁵ a map ∂_n from $C_n(M; G)$ to $C_{n-1}(M; G)$ for every integer n . These maps are group homomorphisms—that is, for integer or real coefficients, they are linear: for instance, we have already seen that $\partial(a + b) = \partial a + \partial b$ on the torus.

⁵The precise definition of the boundary map depends on the way subspaces are defined, but the properties we discuss here are universal.

The boundary maps ∂_n can be used to arrange the chain groups in a so-called *chain complex*:

$$0 \xleftarrow{\partial_0} C_0(M; G) \xleftarrow{\partial_1} C_1(M; G) \xleftarrow{\partial_2} C_2(M; G) \xleftarrow{\partial_3} \dots.$$

These chain complexes are usually finite: for example, the 2-torus in Figure 2.5 has no 3-dimensional subspaces, so its chain complex (with integer coefficients) reads

$$0 \xleftarrow{\partial_0} C_0(\mathbb{T}^2) \xleftarrow{\partial_1} C_1(\mathbb{T}^2) \xleftarrow{\partial_2} C_2(\mathbb{T}^2) \xleftarrow{\partial_3} 0.$$

In practice, the subscript on the maps ∂_n is often dropped when talking about specific subspaces.

A very important property of the chain complex is that composing two boundary maps always yields zero; this is often abbreviated as $\partial^2 = 0$. In other words, boundaries have no boundaries. An example of this can be seen in Figure 2.5: the 1-chain c is the boundary of the 2-chain S , but it does not have a boundary itself. In homology terms, chains like c which have no boundaries are called *cycles*. The set of n -cycles is denoted Z_n and it forms a subgroup of the n -chain group. It is defined in terms of the kernel of ∂_n , i.e. the n -chains that map to the empty chain 0:

$$Z_n(M; G) := \ker(\partial_n) \subset C_n(M; G).$$

The property $\partial^2 = 0$ implies that all boundaries are cycles, but crucially, it does not imply the opposite: there may be cycles which are not boundaries. In Figure 2.5, d and e are such 1-cycles: we cannot find a 2-chain of which d is the boundary, for instance. This implies that the set of n -chains which are boundaries is a subgroup of the group of n -cycles Z_n . The former group is called the group of n -boundaries and denoted B_n . It is defined as the image of ∂_{n+1} :

$$B_n(M; G) := \text{im}(\partial_{n+1}) \subset Z_n(M; G) \subset C_n(M; G).$$

We can now finally define the homology on M . The n th homology group H_n is the quotient group consisting of all n -cycles modulo n -boundaries:

$$H_n(M; G) := \frac{Z_n(M; G)}{B_n(M; G)} = \ker(\partial_n) / \text{im}(\partial_{n+1}).$$

Again, the coefficient group G is often dropped from the notation under integer coefficients $G = \mathbb{Z}$. The elements of H_n are called *homology classes*, and they are equivalence classes of n -cycles. Two n -cycles γ_1 and γ_2 are called *homologous* if they differ only by a boundary, i.e. if $\gamma_1 = \gamma_2 + \partial\Gamma$ for some $n+1$ chain Γ . In this case they represent the same homology class, and we write $[\gamma_1] = [\gamma_2] \in H_n(M; G)$. For example, the 1-cycle c in Figure 2.5 is the boundary of the 2-chain S , and so it is homologous to the empty cycle: $c = 0 + \partial S$, meaning $[c] = 0 \in H_1(\mathbb{T}^2)$. Similarly, any n -boundary represents the trivial class in H_n in general. Intuitively, this is because a boundary can always be continuously retracted to a point (for example, c can be retracted by shrinking S), where it vanishes and becomes the empty cycle.

Another important example of homologous cycles is illustrated in Figure 2.6. In

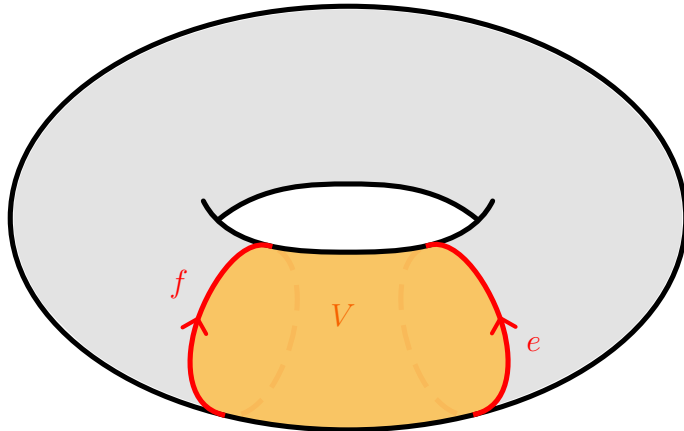


Figure 2.6: The 2-torus \mathbb{T}^2 , featuring the same 1-cycle e as before, and also a 1-cycle f which is obtained by moving e along the torus. The boundary of the 2-chain V indicated in orange is precisely the difference of these cycles: $\partial V = e - f$. Since e and f differ by a boundary, they are homologous, i.e. $[e] = [f] \in H_1(\mathbb{T}^2)$.

this case, we see that non-trivial cycles may also represent the same homology class if they can be deformed into each other continuously.

These examples demonstrate an important general property: the homology group classifies cycles that differ from each other topologically, i.e. cannot be deformed into one another. As a result, the homology groups H_n have a much simpler structure than the underlying chain groups. For example, the first homology group of the 2-torus $H_1(\mathbb{T}^2)$ consists precisely of elements of the form

$$m_d[d] + m_e[e], \quad m_d, m_e \in G = \mathbb{Z},$$

where d and e are as in Figure 2.5. It follows that this group looks like two copies of \mathbb{Z} :

$$H_1(\mathbb{T}^2) \cong \mathbb{Z}^2.$$

The 0th homology group can be obtained by similar logic: all single points on \mathbb{T}^2 can be continuously moved to a single point p , so that elements of $H_0(\mathbb{T}^2)$ are of the form

$$m_p[p], \quad m_p \in \mathbb{Z},$$

and consequently

$$H_0(\mathbb{T}^2) \cong \mathbb{Z}.$$

For similar reasons, if M consists of k connected components, then $H_0(M) = \mathbb{Z}^k$ in general.

Finally, the only two-dimensional subspace of \mathbb{T}^2 that represents a non-trivial homology class turns out to be the whole torus itself; as a result, H_2 also has a single generator:

$$H_2(\mathbb{T}^2) \cong \mathbb{Z}.$$

These three groups completely classify the homology of the 2-torus, since it only admits n -chains for $0 \leq n \leq 2$. This is a general property of homology: unlike

homotopy, where higher homotopy groups may have a highly non-trivial structure, the homology groups H_n of a d -dimensional manifold are always 0 for $n > d$ and $n < 0$.

2.2.2 Cohomology

The chain complex structure underlying homology allows for a natural counterpart called cohomology, which is obtained by *dualising* the chain complex. Dualisation is a concept that shows up all over mathematics; the basic idea is that a mathematical object can be paired with a different object—its *dual*—in order to obtain something like a simple number. A familiar example from physics is that of a covector: in physics notation, any vector V^μ can be paired with any covector ω_μ to obtain a scalar $\omega_\mu V^\mu \in \mathbb{R}$. Formally, a covector is defined as a linear function from the underlying vector space to \mathbb{R} .

A similar construction is used to define *cochains* on a manifold M . An n -cochain is a homomorphism from the n -chain group $C_n(M; G)$ into the coefficient group G ; under the usual integer coefficients, this is a function $C_n(M) \rightarrow \mathbb{Z}$ that assigns an integer to each n -chain linearly. The cochains form a group which has a very similar structure to the chain group itself. We denote the n -cochain group with a raised index:

$$C^n(M; G) := \text{Hom}(C_n(M; G), G).$$

There is an interpretation of cochains with coefficients in \mathbb{R} which is of special relevance to physicists. This comes in the form of integration on differential forms: for example, a 1-form \mathcal{A} can be paired with an oriented 1-dimensional subspace $\ell \subset M$ in a line integral, to obtain a real number $\int_\ell \mathcal{A} \in \mathbb{R}$. The definition of integration can be readily generalised from subspaces of M to chains, so that a differential n -form becomes a linear map on the chain group:

$$\omega : C_n(M; \mathbb{R}) \rightarrow \mathbb{R}, \quad c := \sum_i c_i X_i \mapsto \int_c \omega := \sum_i c_i \int_{X_i} \omega,$$

where as before, X_i are oriented n -dimensional subspaces of M and c_i are coefficients in \mathbb{R} . This definition of integration gives rise to a complete cohomology theory in terms of differential forms, called *de Rham cohomology*. This theory is fully equivalent to more abstractly defined cohomology with \mathbb{R} coefficient, and offers a useful link to physical observables: the existence of de Rham cohomology means that many topological invariants can be expressed in terms of integrals over differential forms such as the Berry flux 1-form \mathcal{A} and the Berry curvature 2-form \mathcal{F} .

The main shortcoming of de Rham cohomology lies in its real coefficients. As mentioned before, the universal coefficient theorem implies that \mathbb{Z} coefficients may provide richer homology groups, and the same also holds for cohomology. This is especially true when the homology and cohomology groups contain $\mathbb{Z}_2 := \mathbb{Z}/2\mathbb{Z}$ factors (referred to as *torsion*⁶), corresponding to \mathbb{Z}_2 physical invariants; these appear especially often on the non-orientable manifolds studied in this work. These factors

⁶Formally, torsion also includes more general factors \mathbb{Z}_k , but these do not tend to appear in the physics literature as often.

disappear under \mathbb{R} coefficients, relating to the fact that $\mathbb{R}/2\mathbb{R} = 0$. Still, many of the associated invariants may be expressed using modified integral formulas, and in any case, the de Rham theory offers a physically intuitive perspective on cohomology. For these reasons, we will continue to use it as an analogy for the more abstract concepts of integer-valued cohomology.

Just as in homology, the cochain groups of cohomology are gathered into a *cochain complex*: for example, the cochain complex of the 2-torus is

$$0 \xrightarrow{\delta_{-1}} C_0(\mathbb{T}^2) \xrightarrow{\delta_0} C_1(\mathbb{T}^2) \xrightarrow{\delta_1} C_2(\mathbb{T}^2) \xrightarrow{\delta_2} 0.$$

The maps $\delta_n : C^n \rightarrow C^{n+1}$ are called *coboundary* maps, and they are a natural result of dualising the boundary maps $\partial_{n+1} : C_{n+1} \rightarrow C_n$, meaning they are uniquely defined by the property

$$\delta\omega(c) = \omega(\partial c). \quad (2.2)$$

This duality takes on a familiar form in de Rham cohomology: there, the coboundary map is the exterior derivative d on differential forms, and the duality above becomes

$$\int_c d\omega = \int_{\partial c} \omega,$$

which is precisely Stokes' theorem. For example, suppose a Berry connection 1-form \mathcal{A} (as defined in Section 2.1.2) exists on the 2-torus in Figure 2.5. Then the Berry curvature 2-form \mathcal{F} can locally be written as $\mathcal{F} = d\mathcal{A}$, and Stokes' theorem tells us that

$$\int_S \mathcal{F} = \int_S d\mathcal{A} = \int_{\partial S} \mathcal{A} = \int_c \mathcal{A}.$$

This dual property of the coboundary maps also ensures that the cochain complex inherits the $\delta^2 = 0$ property of the chain complex: for any n -cochain ω and $n+2$ -chain c , we find

$$\delta^2\omega(c) = \omega(\partial^2 c) = \omega(0) = 0,$$

so that there is a similar $\delta^2 = 0$ property here.

The construction of the cohomology groups from the cochain complex proceeds completely analogously to that of the homology groups. Just as an n -cycle is an n -chain with no boundary, an n -cocycle is a cochain ω which has no coboundary, i.e. for which $\delta\omega = 0$. In de Rham cohomology, cocycles are called *closed* differential forms (i.e. those with $d\omega = 0$). The n -cocycles form a group which is denoted (again using a raised index) as

$$Z^n(M; G) := \ker(\delta_n).$$

Similarly, an n -coboundary is defined as an n -cochain ω which can be written as $\omega = \delta\eta$ for some $(n-1)$ -cochain η . In the context of de Rham cohomology, the coboundaries are referred to as *exact* differential forms (i.e. forms which can be written as $\omega = d\eta$). Again, the n -coboundaries form a group which is denoted

$$B^n(M; G) := \text{im}(\delta_{n-1}).$$

The $\delta^2 = 0$ property of the cochain complex implies that all coboundaries are cocycles. In de Rham cohomology, this corresponds precisely to the Bianchi identity

$d^2 = 0$, which says that all exact forms are closed. As before, this implies that B^n is a subgroup of Z^n , and we can define the n th *cohomology group* as their quotient:

$$H^n(M; G) := \frac{Z^n(M; G)}{B^n(M; G)} = \ker(\delta_n)/\text{im}(\delta_{n-1}).$$

The elements of this group are called *cohomology classes*. In the de Rham picture, non-trivial cohomology classes are represented by forms which are closed, but not exact. For example, this can be the case for the Berry curvature 2-form \mathcal{F} : while it can always be written as $d\mathcal{A}$ *locally*, this depends on a local choice of gauge. Globally, there may be gauge singularities preventing \mathcal{A} from being well defined everywhere. As a result, an expression like $\int_{\mathbb{T}^2} \mathcal{F}$ may have a non-zero value, precisely because \mathbb{T}^2 itself is a 2-cycle with non-trivial global topology. In this case, \mathcal{F} represents a non-zero cohomology class $[\mathcal{F}] \in H^2(\mathbb{T}^2; \mathbb{R})$.

This close link between cohomology classes and non-trivial cycles ensures that the cohomology groups H^n are intimately related to the homology groups H_n in their structure; in fact, in the absence of the aforementioned \mathbb{Z}_2 torsion factors, there is a direct isomorphism $H^n(M) \cong H_n(M)$ for every $n \in \mathbb{Z}$.⁷ This means that for instance, the cohomology groups of the 2-torus are the same as the homology groups:

$$H^0(\mathbb{T}^2) \cong \mathbb{Z}; \quad H^1(\mathbb{T}^2) \cong \mathbb{Z}^2; \quad H^2(\mathbb{T}^2) \cong \mathbb{Z}.$$

There is a straightforward interpretation of these groups in terms of their homology counterparts: for example, $H^1(\mathbb{T}^2)$ is generated by the cocycles (1-forms) that evaluate to 1 on either of the two non-trivial loops that generate $H_1(\mathbb{T}^2)$, and to 0 on the other.

Finally, we should reiterate what the value in this whole process of dualisation is, given that the cohomology groups are so easily computed from their homology counterparts. The answer is that cohomology, despite being seemingly more involved than homology, is in some ways a more natural theory from both a physical and a mathematical point of view. Physically, the interpretation in terms of differential forms allows topological invariants to be written as integrals of physical quantities. Mathematically, it turns out that there are deep links between cohomology theory and the topological classification of vector bundles; for example, the complex line bundles over a manifold M are always fully classified by $H^2(M)$. These line bundles turn out to be in direct correspondence to certain topological states of matter in a two-band model. The full classification of vector bundles is the subject of an advanced area of mathematics known as K-theory, which is really a generalised cohomology theory. K-theory in turn plays an important role in the more general classification of topological phases of matter [35, 36].

⁷To be precise, when there are torsion factors in some homology group H_n , they will appear “one dimension up” in the cohomology group H^{n+1} instead of H^n . Incidentally, since there is no torsion in de Rham cohomology, this means that $H^n(M; \mathbb{R}) \cong H_n(M; \mathbb{R})$ in full generality.

Chapter 3

Topological states of matter & symmetries

In recent years, innumerable forms of topological matter have been studied in many different contexts, using many different methods. Their study has revealed a richness of systems with widely varying physical properties [6, 37–39]. We cannot hope to offer a comprehensive overview of such a diverse and rapidly developing field, but there are some common threads to be found across much of it that are worth highlighting.

The first of these commonalities is that symmetries always play a crucial role in determining how many topologically distinct phases a system has. This interplay between symmetry and topology is subtle: on the one hand, certain topological phases may only be distinct if a symmetry is assumed, in which case the topology is said to be protected by the symmetry. On the other hand, certain topological states are inherently asymmetrical in some way, so that introducing a symmetry may prevent non-trivial topology from arising altogether.

Another very important characteristic that is shared by most topological phases of matter lies in the appearance of boundary states. For example, a topological insulator may conduct electricity on its surface, in a way that is determined and protected by the topology of the insulating bulk of the material. This correspondence between bulk topology and surface behaviour is known as the *bulk-boundary correspondence*, and it is a central tenet of the theory of topological solids.

In this chapter, we offer a brief overview of some of the most important models of topological matter, in order to see these general features in action and explore different ways in which topological phases can be classified. Our treatment of these models is somewhat non-standard: whereas most reference works take a “physics-first” approach where one starts with a physical system and then studies the topology that arises from it, we choose to place greater emphasis on the topological description of each model first, and then discuss the physical realisations of the model. This better aligns with the highly topological approach that we take to studying Weyl semimetals in later chapters, and it is our hope that it paints a somewhat clearer picture of how seemingly very different topological systems relate to each other. Still, much of our exposition here borrows from or reframes the more standard approaches in Refs. [6, 37–39].

We begin in Section 3.1 by studying the Su–Schrieffer–Heeger model, a one-

dimensional model which is arguably the most basic example of a topological insulator. We then review the role of symmetry somewhat more explicitly in Section 3.2, based on a widely used classification scheme known as the tenfold way. In Section 3.3, this knowledge is applied to several models in two and three dimensions, with a special focus on those which prove to be relevant to this work.

3.1 The Su–Schrieffer–Heeger model

One of the prototypical examples of a topological insulator, and perhaps the simplest incarnation of the concept, comes in the form of a one-dimensional model called the Su–Schrieffer–Heeger (SSH) model. In somewhat of a departure from the usual treatment, we will begin from basic topological considerations and observe how the SSH model arises naturally from studying the simplest possible distinct topological phases.

Concretely, consider an infinite one-dimensional chain of unit cells indexed by $n \in \mathbb{Z}$. At this point, we make no assumptions on the internal structure of these unit cells; they may contain any number of atomic sites in principle. A boundary will be introduced later, but its relevant properties will turn out to be determined by the crystal’s bulk topology. Suppose the real-space Hamiltonian of the system is periodic in the unit cells. By Bloch’s theorem, two crystal momenta k and k' are then equivalent if they differ by an integer multiple of 2π . This means that the Brillouin zone B can be taken to be the interval $[-\pi, \pi]$, with the points $-\pi$ and π identified; this space is homeomorphic to the circle S^1 .

We might begin with a simple two-band Bloch Hamiltonian $\mathcal{H}(k) = \mathbf{h}(k) \cdot \boldsymbol{\sigma}$, with

$$\mathbf{h} : B \cong S^1 \rightarrow \mathbb{R}^3, \quad k \mapsto \begin{pmatrix} h_x(k) \\ h_y(k) \\ h_z(k) \end{pmatrix}.$$

Such a Hamiltonian describes a gapped phase precisely when the map \mathbf{h} is non-zero everywhere, so that the topological classification of these phases is given by classes of maps from S^1 to \mathbb{R}^3 minus the origin—that is, homotopy classes of loops in $\mathbb{R}^3 \setminus \{0\}$. However, this space has a trivial fundamental group $\pi_1(\mathbb{R}^3 \setminus \{0\}) \cong 0$, meaning that all such loops can be contracted to a point; in other words, all gapped Hamiltonians are adiabatically connected, and there are no topologically interesting phases.

This situation can be remedied by imposing a constraint on the Hamiltonian: we require that $h_z(k) = 0$. Doing this effectively reduces \mathbf{h} to a two-dimensional map:

$$\mathbf{h} : B \cong S^1 \rightarrow \mathbb{R}^3, \quad k \mapsto \begin{pmatrix} h_x(k) \\ h_y(k) \end{pmatrix}.$$

The gapped phases are now classified by the non-trivial fundamental group

$$\pi_1(\mathbb{R}^2 \setminus \{0\}) \cong \mathbb{Z}.$$

This group is indexed by winding number: loops that wind around the origin $a \in \mathbb{Z}$ times cannot be deformed into those with a different winding number $b \neq a$. In

particular, loops with a non-zero winding number cannot be contracted to a point, and the associated phases are considered topological. Note that imposing a constraint on the Hamiltonian has made this system rather more interesting from a topological point of view, even though it seems like it has been simplified. Once we move to the physical picture, we will see that this restriction corresponds to imposing a certain symmetry on the system. For now, we note that the winding number ν itself has a more physical interpretation: it is the number of complete $U(1)$ rotations that the Berry phase picks up when moving around the Brillouin zone S^1 once. This can be calculated using the following expression:

$$\nu = \frac{1}{2\pi} \oint_{S^1} \mathcal{A}, \quad (3.1)$$

where \mathcal{A} is the Berry curvature 1-form as introduced in Section 2.1.2. This calculation in terms of a 1-form implies that the topology may also be classified using first cohomology, and indeed,

$$H^1(S^1) \cong \mathbb{Z} \cong \pi_1(\mathbb{R}^2 \setminus \{0\}).$$

Let us now choose a more specific Hamiltonian to arrive at a concrete physical system. We begin with the simplest possible¹ topologically distinct states, one trivial and one topological:

$$\mathbf{h}_{\text{triv}}(k) = \begin{pmatrix} 1 \\ 0 \\ 0 \end{pmatrix}, \quad \mathbf{h}_{\text{top}}(k) = \begin{pmatrix} \cos(k) \\ \sin(k) \\ 0 \end{pmatrix}.$$

To characterise a phase transition between these two states, we consider the linear combination $\mathbf{h}(k) = v\mathbf{h}_{\text{triv}}(k) + w\mathbf{h}_{\text{top}}(k)$, with $v, w \geq 0$. The phase described by the resulting Bloch Hamiltonian is trivial when $v > w$, gapless (i.e. conducting) when $v = w$, and topological when $v < w$; see Figure 3.1.

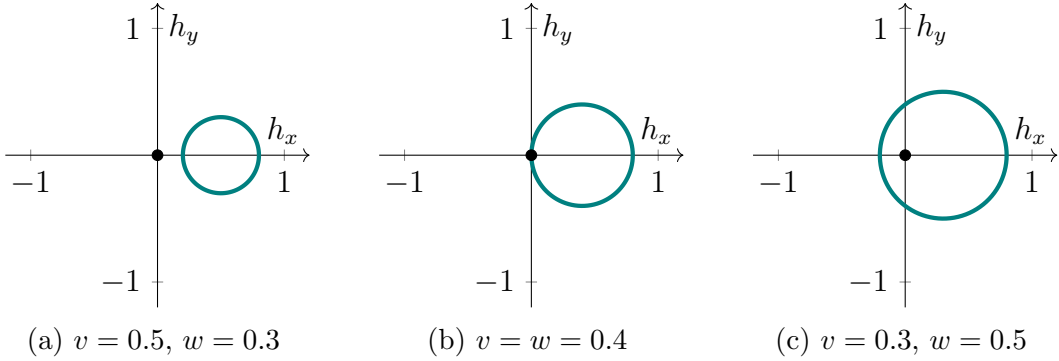


Figure 3.1: Contours in Hamiltonian space for (a) trivial, (b) conducting and (c) topological phases.

¹Our particular choice of x , y , and z coordinates very conveniently leads to the SSH model. However, mathematically speaking, all similar models are related by a simple change of basis.

We are now in a position to start analysing the physics of the system. Concretely, the momentum space Hamiltonian is given by

$$\mathcal{H}(k) = \mathbf{h}(k) \cdot \boldsymbol{\sigma} = [v + w \cos(k)]\sigma_x + w \sin(k)\sigma_y = \begin{pmatrix} 0 & v + w e^{-ik} \\ v + w e^{ik} & 0 \end{pmatrix}.$$

We can set up a Fourier transform to real space by rewriting this suggestively in terms of the unit cell index n :

$$\mathcal{H}(k) = e^{-ik(n-n)} \begin{pmatrix} 0 & v \\ v & 0 \end{pmatrix} + e^{-ik[(n+1)-n]} \begin{pmatrix} 0 & w \\ 0 & 0 \end{pmatrix} + e^{-ik[n-(n+1)]} \begin{pmatrix} 0 & 0 \\ w & 0 \end{pmatrix}$$

The exponentials in this expression are turned into real space delta functions under Fourier transformation, which indicates that the eigenstates are highly confined around certain positions. This is precisely the setting for the tight-binding approximation discussed in Section 2.1. It follows that we can write the Hamiltonian in an exact unit cell basis as

$$\hat{H} = \sum_{n=-\infty}^{\infty} \left[|n\rangle \langle n| \otimes \begin{pmatrix} 0 & v \\ v & 0 \end{pmatrix} + \left(|n+1\rangle \langle n| \otimes \begin{pmatrix} 0 & w \\ 0 & 0 \end{pmatrix} + \text{h.c.} \right) \right], \quad (3.2)$$

where “h.c.” denotes the Hermitian conjugate of the preceding term. This Hamiltonian contains a term which acts within the unit cells, and terms which act between neighbouring unit cells, parametrised by v and w respectively. The structure of these interactions can be made somewhat more transparent by going to a finite chain of length N . The Hamiltonian then becomes

$$\hat{H} = \sum_{n=0}^N |n\rangle \langle n| \otimes \begin{pmatrix} 0 & v \\ v & 0 \end{pmatrix} + \sum_{n=0}^{N-1} \left(|n+1\rangle \langle n| \otimes \begin{pmatrix} 0 & w \\ 0 & 0 \end{pmatrix} + \text{h.c.} \right),$$

where open boundary conditions have been introduced on the ends of the chain to allow the boundary behaviour to be studied. The tensor products can be expanded in order to cast the Hamiltonian into a full $2N \times 2N$ matrix:

$$\hat{H} = \begin{pmatrix} 0 & v & 0 & 0 & & & & \\ v & 0 & w & 0 & & & & \\ 0 & w & 0 & v & & & & \\ 0 & 0 & v & 0 & & & & \\ & & & & \ddots & & & \\ & & & & & \ddots & & \\ 0 & & & & & & 0 & 0 \\ & & & & & & w & 0 \\ & & & & & & 0 & w \\ & & & & & & 0 & v \\ & & & & & & 0 & 0 \end{pmatrix}.$$

A physical interpretation of this system presents itself in the form of this matrix: it describes a chain of $2N$ sites, with alternating hopping amplitudes v and w between neighbouring sites. The unit cells now consist of two of these sites, and v and w are referred to as the *intra-cell* and *inter-cell* hoppings, respectively. When these two hoppings are equal, the system is in the gapless phase $v = w$, corresponding

to a chain where all bonds are equally strong. Intuitively, this homogeneity allows electrons to propagate freely along the chain. On the other hand, in the insulating cases $v \neq w$, one of the two hoppings is stronger than the other, and the electrons tend to be confined around these stronger bonds.

Dividing the unit cells into two individual sites in this way allows us to distinguish two so-called *sublattices* of the crystal, which we label A and B . The notation can then be simplified by labelling quantum states according to the sublattice on which they are localised:

$$|n, A\rangle \equiv |n\rangle \otimes \begin{pmatrix} 1 \\ 0 \end{pmatrix}, \quad |n, B\rangle \equiv |n\rangle \otimes \begin{pmatrix} 0 \\ 1 \end{pmatrix}.$$

In this notation, the Hamiltonian becomes

$$\hat{H} = \left(\sum_{n=0}^N v |n, B\rangle \langle n, A| + \sum_{n=0}^{N-1} w |n+1, A\rangle \langle n, B| \right) + \text{h.c.} \quad (3.3)$$

The tight-binding model of alternating hoppings is precisely the SSH model as it was introduced in 1979 by Wu-Pei Su, John Robert Schrieffer, and Alan J. Heeger [40, 41]. It was devised as a model for polyacetylene, a polymer chain which features alternating single and double covalent bonds; see Figure 3.2. This material displays

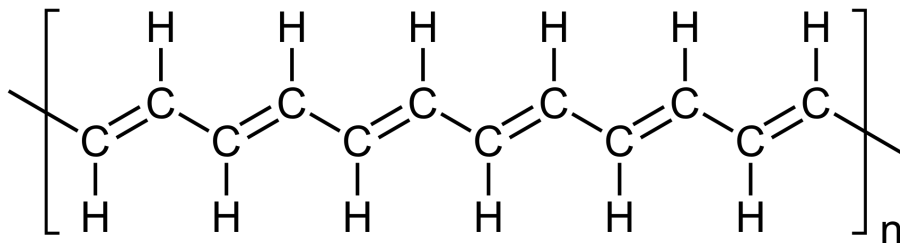


Figure 3.2: Structural diagram of polyacetylene. Electrons are transported more readily along the double bonds, which is modelled using a larger hopping parameter.

unexpectedly high conductivity when doped with halogen impurities, and the SSH model affords an explanation for this.

To understand how this metallic behaviour comes about, the differences between the trivial and the topological phase must be examined more closely. The two phases appear to be identical at a first glance: if the unit cell in polyacetylene is chosen in such a way that the stronger double bond represents the intra-cell hopping v , then the system is in the trivial phase $v > w$, and if instead the unit cell is centred around a single bond, $v < w$ and the phase is topological. In either case, valence electrons are expected to remain localised around the double bonds, leading to the same insulating bulk behaviour.²

²The attentive reader might wonder why the conducting $v = w$ phase does not occur naturally in this system. This is a result of the so-called Peierls transition: in a nutshell, introducing a band gap locally lowers the energy of the (filled) valence band and raises that of the (empty) conduction band. This makes it energetically favourable for atoms in the chain to pair up, in a process referred to as dimerisation.

The difference between the two phases only becomes apparent when the endpoints of the chain are studied. For example, the leftmost atom is not subject to any inter-cell hopping, and it is only connected to the other atom in its unit cell. In the trivial case, this connection is strong and the two atoms share their valence electrons. In the topological phase, on the other hand, the second atom from the left prefers to share electrons with its right-hand neighbour, and the leftmost atom becomes isolated. In the limit where v goes to zero, this isolation becomes complete; this is illustrated in Figure 3.3. and the edge sites carry zero-energy eigenstates. In this case, only the

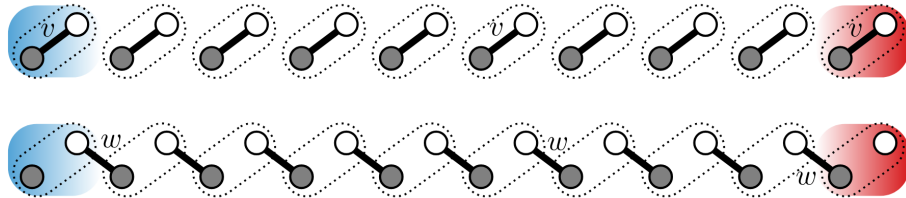


Figure 3.3: Figure from Ref. [38]. Top: when v is the dominant hopping term, the boundaries of the chain (indicated in blue and red) do not feature any interesting topology. Bottom: for small enough v , there is one atomic site at each boundary that becomes individually isolated from the rest of the chain.

second term in the Hamiltonian (3.3) survives, and the edges obey the eigenvalue equations

$$\hat{H} |1, A\rangle = \hat{H} |N, B\rangle = 0.$$

These edge modes can be shown to persist for non-zero $v < w$, in which case they become highly localised and approach zero energy in the $N \rightarrow \infty$ limit [38]. The salient point is that the boundary modes of the topological phase exist inside the energy gap: their energy eigenvalues have a point-like degeneracy at the Fermi level $E_F = 0$.

Something remarkable has happened: we have started from a topological description of a gapped bulk phase, and the resulting physical effects appear as in-gap zero energy modes on the boundary of the material. As will become apparent upon looking at other examples, the existence of edge modes at the Fermi level is a fairly general feature of topological phases of matter,³ captured in the so-called *bulk-boundary correspondence*. It can be thought of as being a result of the inability to go continuously from a topological gapped phase to a trivial one in real space; in particular, the outside boundary of an idealised material connects to the vacuum, which is also considered a trivial gapped phase.

The existence of zero-energy boundary modes is what helps explain the unusual conductivity of doped polyacetylene. It turns out that introducing impurities promotes the formation of domains with different topological phases within the material. The boundaries between these domains carry charge and their zero energy

³This is not a completely general statement: topological phases with edge modes at energies other than E_F have been shown to be theoretically feasible [42]. For our purposes, it will be sufficient to restrict our attention to edge modes at the Fermi level.

ensures that they are mobile. As such, they can be described as moving quasiparticle excitations called *solitons*, and the large current response of the material can be attributed to them. These soliton states have since been observed experimentally [43], as has the change in Berry phase associated with the topological invariant in Equation (3.1) [44].

To close out this section, we return to the physical interpretation of imposing $h_z = 0$, which is the constraint that allowed for non-trivial topology to arise in the first place. This interpretation comes from the fact that the 2×2 matrices in the Hamiltonian in Equation (3.2) act between the two different sublattices A and B . The exclusion of a h_z term ensures that these matrices only have off-diagonal elements; that is, states can hop from sublattice A to sublattice B and vice versa, but never within either of the two sublattices. This is called *sublattice symmetry* or *chiral symmetry*, and it can be captured in terms of operators. This is done by defining the projection onto either sublattice,

$$\hat{P}_A = \mathbb{1} \otimes \begin{pmatrix} 1 & 0 \\ 0 & 0 \end{pmatrix}, \quad \hat{P}_B = \mathbb{1} \otimes \begin{pmatrix} 0 & 0 \\ 0 & 1 \end{pmatrix}.$$

Sublattice symmetry then implies that the Hamiltonian obeys the following relations:

$$\hat{P}_A \hat{H} \hat{P}_A = \hat{P}_B \hat{H} \hat{P}_B = 0.$$

Making use of the fact that $\hat{P}_A + \hat{P}_B = \mathbb{1}$, the chiral symmetry on the Hamiltonian can be expressed in the form

$$\begin{aligned} \hat{H} &= (\hat{P}_A + \hat{P}_B) \hat{H} (\hat{P}_A + \hat{P}_B) \\ &= \hat{P}_A \hat{H} \hat{P}_B + \hat{P}_B \hat{H} \hat{P}_A \\ &= (\hat{P}_A - \hat{P}_B) \hat{H} (\hat{P}_B - \hat{P}_A) \\ &=: -\hat{\mathbf{S}} \hat{H} \hat{\mathbf{S}}, \end{aligned}$$

with $\hat{\mathbf{S}} := \hat{P}_A - \hat{P}_B = \mathbb{1} \otimes \sigma_z$ having the property that $\hat{\mathbf{S}} = \hat{\mathbf{S}}^{-1} = \hat{\mathbf{S}}^\dagger$. We can think of this symmetry as an anticommutation relation,

$$\{\hat{H}, \hat{\mathbf{S}}\} = 0. \tag{3.4}$$

A similar statement holds in momentum space, where σ_z plays the role of $\hat{\mathbf{S}}$: there, chiral symmetry can be expressed as

$$\mathcal{H}(k) = -\sigma_z \mathcal{H}(k) \sigma_z \iff \{\mathcal{H}(k), \sigma_z\} = 0, \tag{3.5}$$

which is precisely the case when the Hamiltonian only has σ_x and σ_y terms.

An immediate consequence of this setup is that the trivial and topological phase become adiabatically connected if we allow for sublattice symmetry breaking ($h_z \neq 0$). This means that the topological phases of the system are dependent on the symmetry remaining unbroken, and as such they are considered to be *protected* by it.

3.2 The tenfold way of topological matter

The SSH model discussed in the previous section demonstrates that the topological nature of a system is inextricably linked to the symmetries that it possesses. It should come as no surprise, then, that this relation between topology and symmetry has comprised one of the principal avenues of research in topological matter. In this section, we review one of the most important results of this endeavour, which comes in the form of a periodic table of gapped topological phases of matter—often referred to as the *tenfold way*. Much of the discussion here is borrowed from the review in Ref. [45].

The idea at the heart of the tenfold way classification is that any symmetry on a quantum mechanical system—not only a crystalline one—can be reduced to several fundamental components. This idea was first developed by Martin Zirnbauer and Alexander Altland around the turn of the current century [46–48]. We summarise the main ideas of the construction here.

First, the system may be subject to a number of ordinary unitary symmetries, such as rotations, reflections, or the spatial translations that define a crystal. Each of these unitary symmetries is represented by a unitary operator \hat{U} that commutes with the Hamiltonian: that is, the symmetry is defined as

$$\hat{H} = \hat{U}\hat{H}\hat{U}^{-1}.$$

It turns out that one can always find a basis for the Hilbert space in which the Hamiltonian is block diagonal, with none of the blocks commuting with any unitary operator individually. As a consequence, the structure of any Hamiltonian can in principle be understood by considering only the symmetries which are not of this form.

Remarkably, it transpires that there are only three basic operations which generate the remainder of the possible symmetries. The first of these three is the chiral or sublattice symmetry \hat{S} that we have already encountered in the context of the SSH model. As seen in Equations (3.4) and (3.5), the chiral symmetry operator is unitary, but it anti-commutes with the Hamiltonian.

The second remaining type of symmetry is time-reversal invariance. It is generated by an anti-unitary operator \hat{T} that commutes with the Hamiltonian,

$$\hat{H} = \hat{T}\hat{H}\hat{T}^{-1}.$$

Anti-unitarity implies that \hat{T} combines a unitary transformation with complex conjugation. This can be seen to hold for time reversal by noting that the reflection $t \mapsto -t$ acts on the time evolution operator $e^{i\hat{H}t}$ as complex conjugation.

Importantly, it can be shown that the time reversal operator \hat{T} must square to $\hat{T}^2 = \pm \mathbb{1}$, with the positive and negative signs corresponding to bosonic and fermionic statistics, respectively. In momentum space, time-reversal symmetry can be written as

$$\mathcal{H}(\mathbf{k}) = U\mathcal{H}^*(-\mathbf{k})U^{-1},$$

where U is a unitary matrix and the momentum vector \mathbf{k} may have any number of dimensions. The sign change in \mathbf{k} is due to the fact that momentum has a time component.

The final possible symmetry of the system is that of charge conjugation, also known as particle-hole symmetry. It is associated with an anti-unitary operator \hat{C} that anti-commutes with the Hamiltonian:

$$\hat{H} = -\hat{C}\hat{H}\hat{C}^{-1}.$$

Just like the time-reversal operator, \hat{C} can square to two different values $\hat{C}^2 = \pm 1$, yielding physically inequivalent systems.

These three basic symmetry operations are subject to the relation

$$\hat{S} = \hat{T}\hat{C},$$

which implies that a system satisfying any two of the symmetries automatically satisfies the third as well. As a result, there are a total of ten distinct ways of combining the three symmetries, each giving rise to a so-called *symmetry class*. These ten symmetry classes are exactly what makes up the titular *tenfold way*, and they are listed on the left hand side of Table 3.1.⁴

Symmetry			Dimension									
Class	T^2	C^2	S	0	1	2	3	4	5	6	7	8
A	0	0	0	\mathbb{Z}	0	\mathbb{Z}	0	\mathbb{Z}	0	\mathbb{Z}	0	\mathbb{Z}
AIII	0	0	1	0	\mathbb{Z}	0	\mathbb{Z}	0	\mathbb{Z}	0	\mathbb{Z}	0
AI	+1	0	0	\mathbb{Z}	0	0	0	$2\mathbb{Z}$	0	\mathbb{Z}_2	\mathbb{Z}_2	\mathbb{Z}
BDI	+1	+1	1	\mathbb{Z}_2	\mathbb{Z}	0	0	0	$2\mathbb{Z}$	0	\mathbb{Z}_2	\mathbb{Z}_2
D	0	+1	0	\mathbb{Z}_2	\mathbb{Z}_2	\mathbb{Z}	0	0	0	$2\mathbb{Z}$	0	\mathbb{Z}_2
DIII	-1	+1	1	0	\mathbb{Z}_2	\mathbb{Z}_2	\mathbb{Z}	0	0	0	$2\mathbb{Z}$	0
AII	-1	0	0	$2\mathbb{Z}$	0	\mathbb{Z}_2	\mathbb{Z}_2	\mathbb{Z}	0	0	0	$2\mathbb{Z}$
CII	-1	-1	1	0	$2\mathbb{Z}$	0	\mathbb{Z}_2	\mathbb{Z}_2	\mathbb{Z}	0	0	0
C	0	-1	0	0	0	$2\mathbb{Z}$	0	\mathbb{Z}_2	\mathbb{Z}_2	\mathbb{Z}	0	0
CI	+1	-1	1	0	0	0	$2\mathbb{Z}$	0	\mathbb{Z}_2	\mathbb{Z}_2	\mathbb{Z}	0

Table 3.1: Tenfold classification of gapped topological states. The names of all ten symmetry classes are listed on the left, together with the choices of symmetries that they represent—in particular, the columns corresponding to \hat{T} and \hat{C} also list the sign of the squared operator. The dashed horizontal line separates the two complex symmetry classes above from the eight real ones below. The right hand side lists all possible topological invariants in each symmetry class in various dimensions, under the assumption of no commuting unitary symmetries. The table of invariants shows Bott periodicity in the number of dimensions: the complex classes repeat after two columns, and the real classes repeat after eight.

The ten different symmetry classes appearing in this scheme each pose their own unique constraints on the Hamiltonians that are allowed in a system. Importantly,

⁴While the names of the classes are seemingly disordered, they are borrowed from mathematician Élie Cartan's 1926 classification of a subtly related set of geometric spaces.

these constraints affect the topology of the abstract space of permissible non-zero Hamiltonians, allowing for the existence of different non-trivial gapless phases. The precise classification of all these phases is rather involved, and for our purposes we will settle for presenting its results on the right hand side of Table 3.1. Still, we have already seen a simple example of these principles play out in the case of the SSH model in Section 3.1: there, imposing chiral symmetry transformed the Hamiltonian space from $\mathbb{R}^3 \setminus \{0\}$ to $\mathbb{R}^2 \setminus \{0\}$, allowing the one-dimensional Brillouin zone S^1 to map into it with a non-trivial \mathbb{Z} -valued winding number. This is reflected exactly in the table of invariants: imposing chiral symmetry takes us from class A to AIII, and in one dimension this changes the invariant group from a trivial 0 to \mathbb{Z} .

One striking feature of this table of invariants is that it is a periodic table, in the most literal sense. That is, there is a repeating pattern in the table across eight dimensions. More specifically, the symmetry classes are divided up into two *complex* classes and eight *real* classes—the latter being so called because the anti-unitary symmetries act similarly to the reality condition $\hat{H} = \hat{H}^*$. There is then a mod 2 periodicity in the complex classes and a mod 8 periodicity in the real classes. These repetitions turn out to be directly related to a deep mathematical result called Bott periodicity. This result manifests itself in different ways across homotopy, K-theory and the theory of Clifford algebras. For example, the generalised cohomology groups in K theory have a mod 2 periodicity, and their real KO counterparts repeat mod 8. Unfortunately, there is no direct analogue of this result in our preferred standard cohomology setting, and we will not pay it too much mind.

The full tenfold way classification of topological invariants has been of immense importance in the study of topological matter, and doubtless many condensed matter physicists have a variation of Table 3.1 affixed to their fridge door. For any given system in any number of dimensions, it immediately informs of the topological phases that can be expected, as long as the basic symmetries are known. Still, there are some important caveats to the interpretation of this table; before we move on to more examples of specific systems, we cover two limitations that are of importance in our own research.

First, this classification scheme assumes a general N -band description. While many of the invariants listed in this table can be obtained equally well in our simplified two-band model of choice, this does not hold across the board. For example, the \mathbb{Z} invariant for a zero-dimensional class A Hamiltonian (i.e. a generic Hermitian matrix) can be interpreted as the number of occupied bands in the system (i.e. the number of negative eigenvalues). In any given scenario, this may reflect both positively and negatively on the usefulness of the two-band model: on the one hand, it can indicate that the two bands do not carry enough degrees of freedom for a full description. On the other hand, topological invariants which are not stable under the addition of bands away from the Fermi level may not be indicative of any transport phenomena, and these may get “filtered out” in the two-band description—we demonstrate a tentative example of this in our treatment of inversion-symmetric Weyl semimetals in Section 5.4.1.

Second, note that this table specifically records only the invariants which are not protected by a commutative unitary symmetry. Such invariants are called *strong* in the sense that they do not rely on any assumption of translation or similar symmetries.

Nevertheless, in a regular crystalline solid, the translation symmetries routinely give rise to additional *weak* invariants, relating to lower-dimensional entries on the table. We will study three-dimensional examples of this in class AII and A, in Sections 3.3.3 and 4.2.1 respectively. Besides translation, the real-space lattice may also be subject to other symmetries such as rotations and reflections. A comprehensive account of the topological effects of these symmetries in three dimensions is given in Ref. [49].

3.3 Higher-dimensional examples

With the tenfold way in hand, we are now in a good position to review some additional examples of non-trivial topological materials. We will be very brief in our treatment of these systems, and approach them from a generic topological point of view. Readers wishing to learn more about the properties of their physical realisations are referred to the more comprehensive physics-minded overviews in standard references such as Refs. [37–39].

3.3.1 The Chern insulator

A very important class of topological insulators are the so-called *Chern insulators*. These are two-dimensional systems with no additional symmetries beyond lattice translation, i.e. in symmetry class A of the tenfold way. In Table 3.1, it is shown that such two-dimensional class A systems have an integer invariant associated with them.

The invariant on these systems is a so-called *Chern number*, and it can be expressed in terms of the total curvature of the Berry connection:

$$C = \frac{1}{2\pi} \int_{\mathbb{T}^2} \mathcal{F}, \quad (3.6)$$

where \mathbb{T}^2 is the two-dimensional Brillouin torus and \mathcal{F} is the Berry curvature 2-form as defined in Section 2.1. This total curvature represents the U(1) phase change picked up by a state after parallel transport around the full \mathbb{T}^2 , and as such it must be quantised to a multiple of 2π .

The Chern number essentially classifies the curvature 2-form \mathcal{F} into different cohomology classes on the Brillouin torus, as outlined in Section 2.2.2. That is, we can consider \mathcal{F} to be a representative of the second cohomology class⁵

$$[\mathcal{F}] \in H^2(\mathbb{T}^2) \cong \mathbb{Z}.$$

The Chern number can then be thought of as an element of this integer group \mathbb{Z} . This means that the cohomology group $H^2(\mathbb{T}^2)$ precisely classifies the different topological

⁵As explained in Section 2.2.2, \mathcal{F} more properly represents a class in the real-valued de Rham cohomology group $H_{\text{dR}}^2(\mathbb{T}^2) \cong \mathbb{R}$. The analogy is strong enough to be considered direct here, but de Rham cohomology is too plain to encode features such as \mathbb{Z}_2 invariants. This is why we make use of the richer integer-valued cohomology theory throughout this work.

phases of a Chern insulator.⁶

Physically, the best-known realisation of the Chern insulator comes in the form of the *quantum Hall effect*, whereby a magnetic field induces a directional current in the edge of a two-dimensional material. Under the right conditions, this current is quantised, leading to discrete plateaus in the Hall conductance of the material [50, 51]. This effect was found to be described by a Chern number [52]. The discovery of the quantum Hall effect in 1980 and its subsequent description in terms of a topological invariant in 1982 can be considered formative events in the field of topological matter, and both have been rewarded with a Nobel Prize in Physics [2, 5].

The conducting edge state that appears in the quantum Hall effect is a manifestation of the bulk-boundary correspondence that was introduced in Section 3.1 in the context of the SSH model. It is the result of the fact that the edge forms a boundary between the topological quantum Hall state and the vacuum, which is a trivial insulator. In terms of dispersion, this edge mode presents itself as a directional band crossing between the valence and conduction bands, on the one-dimensional Brillouin zone of the material boundary; see Figure 3.4. The direction of this band

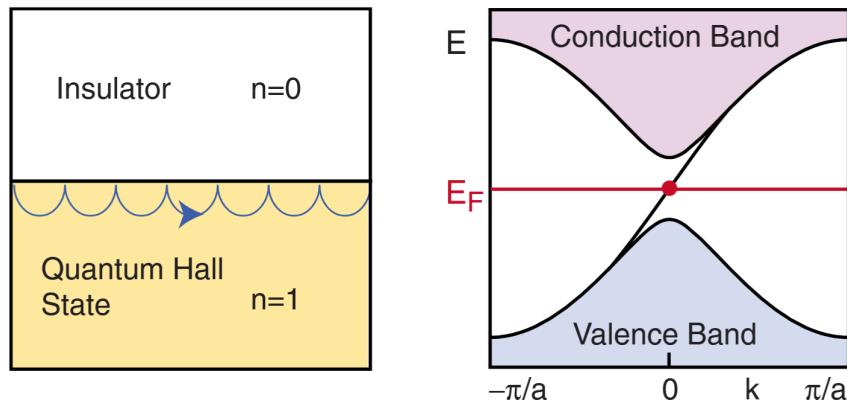


Figure 3.4: Figure from [53]. Left: The edge current in a quantum Hall state exists on the interface between a topological and a trivial insulator (i.e. the vacuum). Right: The conducting edge state corresponds to a chiral band crossing on the one-dimensional surface Brillouin zone, whose chirality is tied to the direction of the current.

crossing is a chiral feature, and it is directly related to the sign of the Chern number.

For completeness we should make mention of the quantum *anomalous* Hall effect here, which is a related realisation of the Chern insulator that does not depend on an external magnetic field [54]. This system is equally well described with a Chern number.

⁶More fundamentally, a complex line bundle called the *valence bundle* can be associated to a gapped Hamiltonian, and the second cohomology group (i.e. the Chern number) classifies the different complex line bundles over a manifold—it is an example of a so-called *characteristic class*. The vector bundle classification point of view is not one we will pursue in detail in this work, but it is in some ways more fundamental than the description in terms of Berry curvature, especially for systems with additional symmetries. This makes it the preferred point of view for precise mathematical classification schemes—often in the form of K-theory.

3.3.2 Quantum spin Hall effect

Another significant class of topological insulators is that of (fermionic) time-reversal symmetric systems in two dimensions. Table 3.1 shows that these class AII systems have a \mathbb{Z}_2 invariant associated with them; that is, they are either trivial or topological, with no distinction between different topological phases.

This symmetry class is realised in the *quantum spin Hall effect*, a variant of the quantum Hall effect which was first introduced to describe properties of graphene [55]. This description essentially consists of two copies of the quantum *anomalous* Hall effect described above, one with spin up states and another with spin down states. These copies are given opposite Chern numbers $C_\uparrow = -C_\downarrow$, so that the related edge currents run in opposite directions; see Figure 3.5.

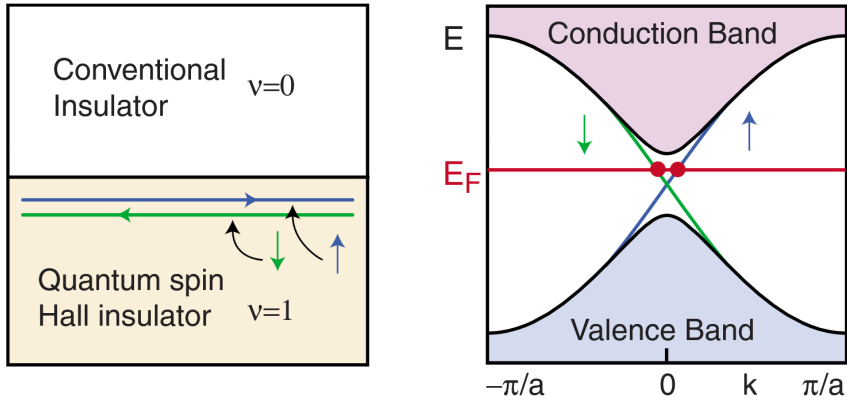


Figure 3.5: Figure from [53]. Left: Two edge currents are shown on a quantum spin Hall state: a current of spin up particles running in one direction, and a spin down current in the opposite direction. Right: The two opposing edge currents give rise to band crossings of opposite chirality.

Because the quantum spin Hall state includes two spin sectors of opposite Chern number, the total Chern number of the system is always zero; as such, it cannot be used to study the topology of such materials. The individual Chern numbers C_\uparrow and C_\downarrow do contain topological information about the system, but they are subject to additional physicality constraints, as reviewed in Ref. [6]. There are multiple equivalent ways to define the \mathbb{Z}_2 invariant on this system [56–59]. We will not review these in detail here; we only note that there are subtle ties to cohomology, made precise in Ref. [60]. This cohomology description also applies to the systems discussed in the next section, and we will postpone our review of it until Section 4.2.4, where it appears in the context of Weyl semimetals.

3.3.3 3D strong and weak insulators

The final class of insulators we will consider here is that of the three-dimensional time-reversal invariant systems. These are a higher-dimensional extension of the quantum spin Hall states discussed above, and their (3D class AII) entry in Table 3.1 suggests that they are subject to a single \mathbb{Z}_2 invariant. However, this does not paint

the complete picture. As discussed at the end of Section 3.2, the translation symmetry of the lattice may induce invariants beyond those recorded in Table 3.1. This is also the case here: there are three additional \mathbb{Z}_2 invariants related to two-dimensional subspaces of the Brillouin zone [58].

The idea is as follows. Within the three-dimensional Brillouin zone \mathbb{T}^3 , there are six special planes which respect time-reversal symmetry; see Figure 3.6. Each

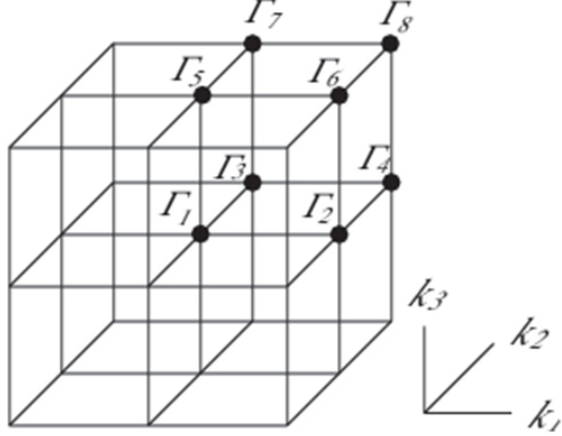


Figure 3.6: Figure from Ref. [6]. The three-dimensional Brillouin zone features eight time-reversal invariant momenta (denoted Γ_i), which satisfy $\mathbf{k} \sim -\mathbf{k}$. Six planes run through these momenta perpendicular to the coordinate directions, and these planes respect time-reversal symmetry as a whole.

of these planes has \mathbb{T}^2 topology, and so it is equivalent to the Brillouin zone of a two-dimensional quantum spin Hall system. As such, all six feature a \mathbb{Z}_2 invariant. The three planes running through the origin define the three weak \mathbb{Z}_2 invariants of the system. The topology of the remaining three planes turns out to be fixed by the single strong \mathbb{Z}_2 invariant predicted by Table 3.1. When this strong invariant is trivial, parallel planes host the same \mathbb{Z}_2 invariant and the system is called a *weak insulator*; conversely, a non-trivial strong invariant gives rise to opposite \mathbb{Z}_2 invariants on parallel planes, in what is called a *strong insulator*.

Just as in the two-dimensional case, these systems have a cohomology description which is laid out in Refs. [60, 61]; again, we will review aspects of this description in the semimetallic context of the next chapter.

Chapter 4

Weyl semimetals

In recent years, interest in topological materials has expanded beyond the purely gapped phases in insulators and superconductors, into the realm of metals and other related gapless phases. One class of topological conductors that is of great interest is that of the so-called Weyl semimetals, which form the focus of the remainder of the present work.

Weyl semimetals are materials that host gapless modes only at very specific momenta in the Brillouin zone. They have a myriad of properties that make them worthy subjects of study, not only from a theoretical perspective but also in potential experimental and engineering applications. Practically, Weyl semimetals have exotic transport properties such as a resistance which is highly sensitive to the application of a magnetic field, opening up countless possibilities for electronic applications. For example, a large photovoltaic effect has been established, prefiguring applications in solar cells and optical sensors [16, 17].

Experimentally, Weyl semimetals comprise the first platform in which the chiral fermions described by Hermann Weyl in 1929 (Ref. [9]) can be studied in nature, in the form of bulk quasiparticle excitations. Despite their mathematical simplicity, such Weyl fermions do not appear as fundamental particles in the Standard Model of particle physics.

This aspect of Weyl semimetals is also of theoretical interest, since their fermionic modes may be altered in different ways beyond the simple description originally given by Weyl. Additionally, the topology of Weyl semimetals is intrinsically rich and generalises many aspects of insulator topology. It is this latter topological point of view which is the main focus of this chapter; the interested reader is referred to Refs. [62] and [63] for more complete physically-minded overviews.

This chapter does not contain any new results; instead, its purpose is to provide the necessary context for the results presented in Chapter 5. We begin by introducing the most important physical aspects of Weyl semimetals in Section 4.1, with a focus on the features that are of topological relevance. Section 4.2 then dives deeper into the underlying topology, introducing many of the relevant mathematical concepts at a fairly elementary level.

4.1 Physical aspects

The concept of Weyl semimetals arises naturally when studying how different energy bands relate to each other in three-dimensional solids. Whereas one and two-dimensional materials are generally gapped unless additional symmetries force the bands to touch, the situation is different in three dimensions. In this context, so-called *accidental band crossings* are expected based on geometric arguments [64].

Accidental crossings can be understood by studying the interplay between any two of the energy bands. In most physically relevant scenarios these will be the valence and conduction band, since these determine the transport properties of a material. Recall that the generic Hermitian two-band Hamiltonian can be written as

$$\mathcal{H}(\mathbf{k}) = h_0(\mathbf{k})\mathbb{1} + \mathbf{h}(\mathbf{k}) \cdot \boldsymbol{\sigma},$$

where \mathbf{k} lives in the three-dimensional Brillouin torus \mathbb{T}^3 .¹ The eigenvalues of this Hamiltonian are

$$E(\mathbf{k}) = h_0(\mathbf{k}) \pm |\mathbf{h}(\mathbf{k})| = h_0(\mathbf{k}) \pm \sqrt{h_1^2(\mathbf{k}) + h_2^2(\mathbf{k}) + h_3^2(\mathbf{k})},$$

so that the two energy bands coincide exactly when $\mathbf{h}(\mathbf{k}) = 0$. That is, band crossings occur at the simultaneous zeroes of three functions h_i for $i \in \{1, 2, 3\}$, all depending on three momentum degrees of freedom. Such a system of three equations with three parameters generically has point-like solutions: the zeroes of each individual h_i normally form a surface in \mathbb{T}^3 , two such surfaces intersect in a set of curves, and the third surface intersects these curves in a set of points. This means that in a three-dimensional system, the gap between two bands generically closes at a discrete set of points, given that the bands are close enough together (i.e. the functions h_i each have zeroes to begin with). These band crossings are called accidental because they are not enforced by any symmetry of the system, but as we will review shortly, they are actually topologically robust and cannot be gapped out by small perturbations.

4.1.1 Weyl points

Near a band intersection at $\mathbf{k} = \mathbf{k}_w$, the Hamiltonian can be linearised: writing $\delta\mathbf{k} := \mathbf{k} - \mathbf{k}_w$, it can be expanded as

$$\mathcal{H}(\delta\mathbf{k}) = h_0(\mathbf{k}_w)\mathbb{1} + \mathbf{v}_0 \cdot \delta\mathbf{k}\mathbb{1} + \sum_{i=1}^3 \mathbf{v}_i \cdot \delta\mathbf{k} \sigma^i + \mathcal{O}(\delta\mathbf{k}^2), \quad (4.1)$$

where $(\mathbf{v}_\mu)_i := \partial_{k^i} h_\mu|_{\mathbf{k}=\mathbf{k}_w}$ records the rate of change of the different components of the Hamiltonian. The spectrum associated with this linear equation looks like two cones which touch at $\mathbf{k} = \mathbf{k}_w$, often collectively called the *Weyl cone*; see Figure 4.1. The different components of Equation (4.1) can all be given an interpretation in

¹The object \mathbf{h} can be interpreted either as a vector field on \mathbb{T}^3 or more abstractly as a function $\mathbf{h} : \mathbb{T}^3 \rightarrow \mathbb{R}^3$. The distinction is immaterial in this context, but we will see it become relevant in the non-orientable context. For reasons that will become clear in Section 5.2.1, we avoid some common lines of reasoning that rely on the vector field point of view in this chapter.

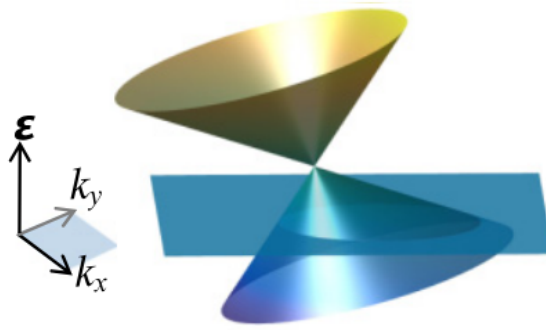


Figure 4.1: Figure from Ref. [65]. Example Weyl cone dispersion corresponding to the linearised Hamiltonian in Equation (4.1). The k_z direction is omitted, and the Fermi energy is indicated by the flat blue plane. Features of this Weyl cone can be related to the coefficients of Equation (4.1): h_0 represents the height of the band touching point above the Fermi level, and it must be reasonably close to zero for the Fermi surface (intersection of the cone with the blue plane) to be approximately point-like. The \mathbf{v}_0 and \mathbf{v}_i determine how the Weyl cone is tilted and deformed in different directions, respectively.

terms of this Weyl cone: for example, $h_0(\mathbf{k}_w)$ is the energy at which the bands touch, and it determines how far this crossing is from the Fermi energy $E_F = 0$. If h_0 is sufficiently far from the Fermi level, the Fermi surface expands to connect with those around other band crossings and gains an extensive two-dimensional structure. Normal metallic dispersive behaviour dominates in this case. However, if h_0 is close enough to zero, then the Fermi surface around \mathbf{k}_w becomes approximately point-like, and there is a low-energy bulk conducting mode at \mathbf{k}_w . In this case, the point \mathbf{k}_w is called a *Weyl point* or *Weyl node*. When all of the crossings between the valence and conduction band have this property, the material is referred to as a *Weyl semimetal*.²

This nomenclature is derived from the traceless \mathbf{v}_i term in Equation (4.1): it bears resemblance to the simple chiral fermions described by Herman Weyl in 1929 [9],

$$H_{\pm} = \mp c \mathbf{p} \cdot \boldsymbol{\sigma},$$

where the speed of light c is replaced by the smaller effective velocities \mathbf{v}_i in different directions—for this reason, the parameters \mathbf{v}_i in Equation (4.1) are often referred to as *Fermi velocities* [67]. In a Weyl semimetal, the aforementioned low-energy modes have similar dispersive properties to Weyl fermions. This is one of the reasons Weyl semimetals are a compelling object of study.

One particularly interesting feature of Weyl fermions is that they have a non-zero chirality associated with them, which leads to certain non-conserved charges upon quantisation—this is known as the chiral anomaly. It turns out that a similar truth holds for the band crossings described by Equation (4.1). They feature an intrinsic

²The term *Weyl metal* is also sometimes used for materials in which the Fermi surface is not point-like due to large h_0 , but still confined to closed surfaces around the band crossings [66]. The topology of such Weyl metals is equivalent to that of their semimetal counterparts, and we will pay them no further mind.

chirality χ , which can be calculated in generic cases by collecting the velocities \mathbf{v}_i into a 3×3 matrix $V_i^j := (\mathbf{v}_i)_j$ and computing the sign of its determinant:

$$\chi = \text{sign} |V_i^j|, \quad (4.2)$$

which yields a chirality of $\chi = \pm 1$. In special cases where the band crossing is non-linear, the chirality may take on other integer values; this is captured more generally using a Berry curvature integral on a two-dimensional sphere surrounding the Weyl point. In this light, Weyl points can be viewed as sources or sinks of the Berry field, with a quantised integer charge. This charge is topological in nature, which is exactly why Weyl points are robust to perturbations. The implications of this topological perspective will be explored in greater detail in Section 4.2.

A final feature of Equation (4.1) that bears mentioning is the inclusion of the \mathbf{v}_0 term. This term can be interpreted in terms of a tilting of the associated Weyl cone. For small \mathbf{v}_0 , the Fermi surface of a Weyl point remains point-like, and the dispersive properties of the virtual Weyl fermion are not greatly affected. However, for large enough \mathbf{v}_0 , the Weyl cone may begin to intersect the Fermi level, causing electron and hole pockets to form on either side of the Weyl point [68]; see Figure 4.2. This tipping

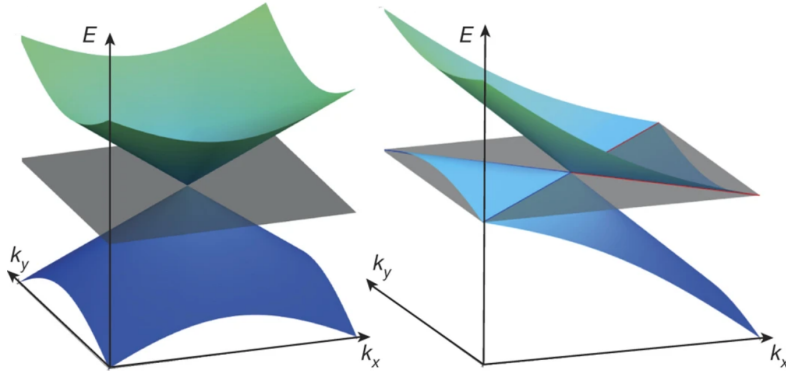


Figure 4.2: Figure from Ref. [68]. Left: Upright Weyl cone corresponding to a normal (type I) Weyl node. Right: “Over-tilted” Weyl cone associated with a type-II Weyl node. Electron and hole pockets in the Fermi surface (i.e. the intersection between the cone and the grey Fermi level plane) are outlined in red and blue, respectively; these pockets appear to continue indefinitely in this linearised picture, but in reality their size is constrained by higher-order terms in the Hamiltonian.

of the Weyl cone induces significantly altered dispersion, leading to different electronic properties. Band touching points with this property are categorised separately as so-called *type-II* Weyl nodes, and conventional Weyl points are sometimes called *type-I* in contrast. Similarly, the quasiparticle excitations associated with over-tilted cones are called *type-II* Weyl fermions, and materials hosting them are referred to as *type-II* Weyl semimetals.³ In contrast to regular *type-I* Weyl fermions, their *type-II* counterparts break Lorentz invariance, making them of some theoretical interest.

³Strictly speaking, a Weyl semimetal can host a combination of *type-I* and *type-II* nodes [69]; as such, the distinction “*type-II* Weyl semimetal” should be treated with some care.

It should be noted that the distinction between type-I and type-II features is purely physical; the different types of Weyl semimetals cannot be distinguished topologically, since Weyl cones can be tipped continuously. This manifests itself in the fact that the chirality of a Weyl point can be determined solely from its \mathbf{v}_i term.

4.1.2 Global features

One important restriction on Weyl semimetals is that the total chirality of all Weyl points in the Brillouin zone must sum to zero—that is, for every source of the Berry field (Weyl point with $\chi > 0$) there must also be a sink ($\chi < 0$), and vice versa. This result is known as the Nielsen–Ninomiya theorem, after Holger Bech Nielsen and Masao Ninomiya who proved it in a more general context in 1981 [18, 19]. We will explore the topological nature of this theorem in more detail in Section 4.2. Physically, this charge cancellation is related to the aforementioned chiral anomaly: electric charge is locally non-conserved near a Weyl point under the application of electric and magnetic fields, and this effect must be cancelled by a Weyl point of the opposite chirality. More details on the chiral anomaly in Weyl semimetals are reviewed in Ref. [63].

The Nielsen–Ninomiya theorem is an indication that Weyl points must communicate with their opposite-chirality counterparts in some way to allow transport of charge. This connection manifests itself on the surface of a Weyl semimetal: there, gapless states called *Fermi arcs* appear in the form of curves connecting the projections of oppositely-charged Weyl points; see Figure 4.3. Fermi arcs serve as

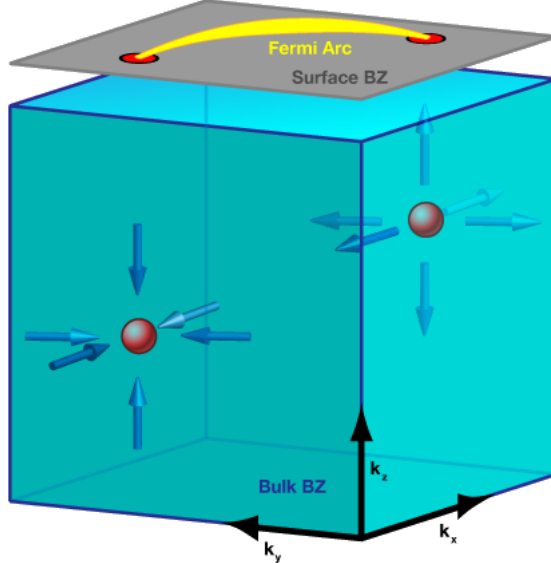


Figure 4.3: Figure from Ref. [70]. The 3D bulk Brillouin zone of a Weyl semimetal with two Weyl points of negative and positive chirality, depicted as a sink and a source of the Berry field respectively. A 2D surface Brillouin zone is depicted in grey at the top, featuring the projection of the two Weyl nodes connected by a Fermi arc of gapless states.

important experimental signatures of Weyl semimetals, and they have been observed

in both electronic and artificial crystals since 2015 [11–14, 71–73]; see Figure 4.4.

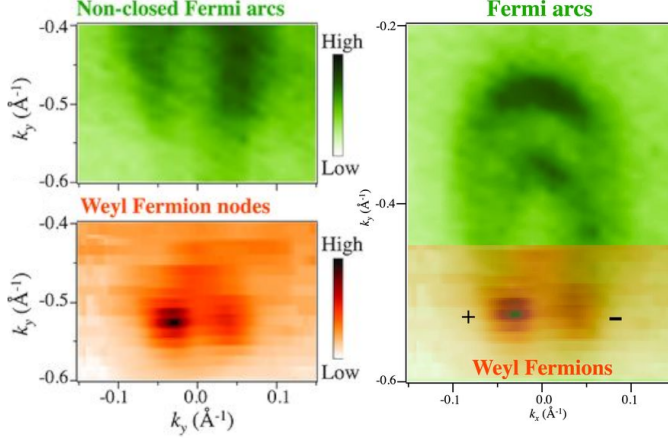


Figure 4.4: Figures from Ref. [71]. Experimental bulk (orange) and surface (green) Fermi surfaces, obtained through angle-resolved photoemission spectroscopy (ARPES). Bottom left: Two Weyl points appearing close together in the bulk. Top left: Fermi arcs are shown to terminate on the surface Brillouin zone above these Weyl points. Right: Bulk measurements are overlaid on the surface measurements at matching k_x and k_y values, showing good agreement between the position of the Weyl nodes and the tail ends of the Fermi arcs. In this case, the two distinct Fermi arcs appear because there are two separate sets of Weyl nodes with the same k_x and k_y coordinates.

4.1.3 Semimetals with symmetries

Thus far, we have discussed Weyl semimetals without assuming any additional symmetry constraints. However, real crystalline solids often naturally possess symmetries beyond simple translational symmetry. Two such symmetries which are especially relevant to the discussion of Weyl semimetals are time-reversal symmetry and inversion symmetry.

Inversion symmetry is a natural property of many real-space lattices: it implies that there is an inversion centre \mathbf{x}_0 in the unit cell around which the lattice is symmetric as $\mathbf{x} \leftrightarrow \mathbf{x}_0 - \mathbf{x}$. In momentum space, this symmetry acts on the Hamiltonian as

$$\mathcal{H}(\mathbf{k}) = U\mathcal{H}(-\mathbf{k})U^{-1}, \quad (4.3)$$

where U is some unitary transformation. In particular, this implies that a Weyl point at $\mathbf{k} = \mathbf{k}_w$ has a partner at $\mathbf{k} = -\mathbf{k}_w$ with the opposite chirality. Take, for example, the case of $U = \mathbb{1}$ and a Weyl point with the simple linearised Hamiltonian

$$\mathcal{H}(\delta\mathbf{k}) = \sum_{i,j} V_i^j \delta k_j \sigma^i.$$

This point has chirality $\chi = \text{sign} |V_i^j|$, and Equation (4.3) implies that

$$\mathcal{H}(-\delta\mathbf{k}) = \sum_{i,j} (V')_i^j (-\delta k_j) \sigma^i = \mathcal{H}(\delta\mathbf{k}),$$

meaning that there is a Weyl point at $\mathbf{k} = -\mathbf{k}_w$ with chirality $\chi' = \text{sign} |(V')_i^j| = \text{sign} |-V_i^j| = -\chi$. This reversal of chirality means Nielsen–Ninomiya is automatically satisfied under inversion symmetry. As a result, the minimum number of Weyl points in such a system is two; a Weyl point may be connected to its own symmetric partner via surface Fermi arcs.⁴

Time-reversal symmetry has a similar action in momentum space, since momentum has a time component. It differs in the sense that time-reversal is an anti-unitary symmetry, meaning it also induces complex conjugation on the Hamiltonian:

$$\mathcal{H}(\mathbf{k}) = U \mathcal{H}^*(-\mathbf{k}) U^{-1}.$$

This complex conjugation changes the sign of the $\sigma^{(2)}$ term in the Hamiltonian; for Weyl points, this changes the sign of \mathbf{v}_2 , inducing a sign change in the determinant of V_i^j . This cancels the sign change discussed above, meaning a Weyl point at $\mathbf{k} = \mathbf{k}_w$ always comes with a symmetric partner of *equal* chirality at $\mathbf{k} = -\mathbf{k}_w$. The presence of same-chirality pairs means that the minimum number of Weyl points in a time-reversal invariant Weyl semimetal is four: following Nielsen–Ninomiya, a pair of $\chi = +1$ points must always be accompanied by a pair of $\chi = -1$ points and vice versa.

The fact that the chirality of Weyl points is reflected in different ways under inversion and time-reversal symmetry immediately implies that a Weyl semimetal cannot satisfy both symmetries at once: if a Weyl point has a non-zero chirality χ , then inversion implies its partner has chirality $-\chi$, while time-reversal implies it should have chirality χ . Physically, this is because the combination of inversion and time-reversal induces a spin degeneracy in the band structure, making modes of opposite chiralities coincide. This is in close analogy to the way in which a Dirac fermion combines two Weyl fermions of opposite chirality into a single description; this is precisely why band touching points of this nature are called *Dirac cones*, and systems featuring them are referred to as *Dirac semimetals*.⁵ Because of the lack of non-zero chiralities, such materials are topologically less rich than their Weyl counterparts, and we will not expand on them further.

All in all, a candidate Weyl semimetallic material must break either inversion or time-reversal symmetry. Of the two, breaking time-reversal symmetry is conceptually simpler in theory: the minimum amount of Weyl points is lower, and the symmetry is straightforwardly broken in the presence of a magnetic field. In practice, the experimental detection of Fermi arcs and other spectral features relies on angle-resolved photoemission spectroscopy (ARPES), which is sensitive to magnetic fields.

⁴This need not be the case: Weyl points in inversion symmetric materials may also be connected to points not related by symmetry. This requires at least two symmetric pairs to be present; an example of such a configuration is shown in the later Figure 5.20(a).

⁵Incidentally, the spin degeneracy ensures that at least a four-band model is required for a proper physical description of a Dirac semimetal.

This is why the first experimental confirmations of electronic Weyl semimetals in 2015 were of materials with preserved time-reversal symmetry and broken inversion symmetry instead, and to date these are the best studied class of Weyl semimetals [11–14, 71, 72, 74–76]. However, the existence of magnetic Weyl semimetals which break time-reversal symmetry is well established, and these have been experimentally observed since 2019 [77–79]. The most widely studied magnetic Weyl semimetals are inversion symmetric, but materials that break both time-reversal and inversion symmetry have also been observed [80–82].

4.2 Topological description

In all the systems studied in Chapter 3, the underlying approach to topological classification has been to study which band structures cannot be deformed into each other without closing the band gap anywhere in the Brillouin zone. Weyl semimetals already feature band crossings in the bulk to begin with, meaning that this approach needs to be modified. The basic idea involves first fixing a number of gapless points in place, and then studying what gapped topologies are admitted on the rest of the Brillouin zone outside of these points. There are many intricacies to this idea, some of which we attempt to review pedagogically in this section.

Though most of the experimental candidates for Weyl semimetals feature either inversion or time-reversal symmetry, the conceptual topology framework is simplest in the absence of any symmetries beyond lattice translation. The majority of this section is written with this context in mind. Most of the concepts here are borrowed from two (fairly technical) works by Varghese Mathai and Guo Chuan Thiang [7, 26].

Only in the final part of this section do we return to time reversal symmetric systems, and review how the inclusion of this symmetry alters the topological description. This provides important context to our treatment of other symmetries in Chapter 5.

4.2.1 3D Chern insulators

To get a good intuition for the topological description of Weyl semimetals, it is useful to first consider a fully insulating material with similar properties. Suppose we have a three-dimensional material that is not subject to any additional symmetries. Such a material is called a 3D Chern insulator [73, 83, 84], in analogy to the 2D Chern insulator studied in Section 3.3.1. This system is not a semimetal, but it provides the relevant topological backdrop: Weyl semimetals can be obtained by letting the bands touch in a 3D Chern insulator. As we will discuss shortly, this allows them to act as transitional phases between different insulating topological states.

From the tenfold way classification in Table 3.1, one might expect such a 3D type A system to be topologically trivial. However, as discussed in Section 3.2 and exemplified in Section 3.3.3, the full topological classification of materials depends not only on the top-dimensional topology, but also on that borrowed from lower-dimensional subspaces. In the case of a 3D Chern insulator, this topology arises on two-dimensional slices of the Brillouin zone; an example of such a slice is highlighted in Figure 4.5.

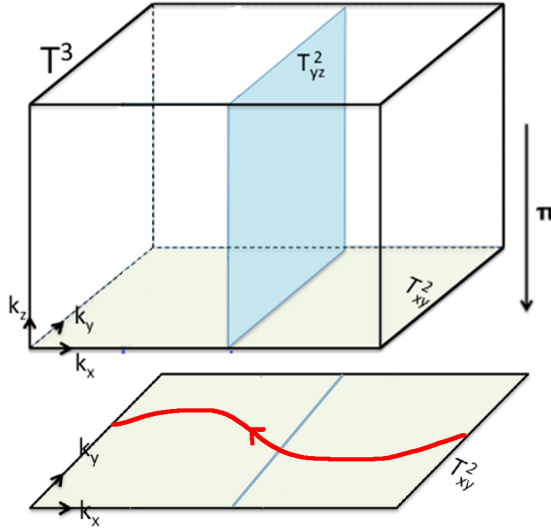


Figure 4.5: Figure adapted from Ref. [7]. The three-dimensional Brillouin torus \mathbb{T}^3 of a Chern insulator is shown, with a two-dimensional slice \mathbb{T}_{yz}^2 indicated in blue. A projection onto a surface Brillouin zone in the xy -direction is also shown, with an example Fermi loop of gapless states in red. In this example, the slice \mathbb{T}_{yz}^2 has a Chern number of $C_x = 1$. Hence, its projection onto the surface is a 1D loop (blue line) that features one chiral band crossing.

There are three topologically distinct ways to slice up the three-torus, all perpendicular to one of the three coordinate directions.⁶ These slices have the topology of a two-torus \mathbb{T}^2 , and a Chern number can be obtained by integrating the Berry curvature \mathcal{F} of the system over them, just as in Equation (3.6). For example, perpendicular to the x direction there is a Chern number⁷

$$C_x = \frac{1}{2\pi} \int_{\mathbb{T}_{yz}^2} \mathcal{F}.$$

This results in a classification by three distinct Chern numbers C_x , C_y and C_z , which are commonly arranged in a so-called *Chern vector*

$$\mathbf{C} = \begin{pmatrix} C_x \\ C_y \\ C_z \end{pmatrix} \in \mathbb{Z}^3.$$

Importantly, these three Chern numbers are all induced by a single two-form \mathcal{F} . In this sense, there is an exact correspondence between topologically distinct Berry

⁶Other 2D slices exist, such as those going diagonally across, but these can all be considered linear combinations of the three “orthogonal” slices. To be precise, the different classes of 2D subspaces of \mathbb{T}^3 form the second homology group $H_2(\mathbb{T}^3) \cong \mathbb{Z}^3$, and this group is *generated* by the orthogonal slices.

⁷Note that it does not matter where along the Brillouin zone the yz -slice \mathbb{T}_{yz}^2 is taken: the Chern number is an integer, while the system is continuous. This means the x coordinate can be changed continuously without changing the resulting Chern number.

curvatures \mathcal{F} and Chern vectors $\mathbf{C} \in \mathbb{Z}^3$. This is precisely what motivates the use of cohomology for classification: just like in the 2D Chern insulator, the two-form \mathcal{F} can be considered to represent a class in the second cohomology group,⁸

$$[\mathcal{F}] \in H^2(\mathbb{T}^3) \cong \mathbb{Z}^3. \quad (4.4)$$

As a result, this group provides a complete classification of the distinct topological phases of the system.

Boundary states

Before moving on to a system with Weyl points, it will be instructive to study the gapless modes that arise on the surface of a 3D Chern insulator with non-zero Chern vector. Figure 4.5 illustrates the case where $\mathbf{C} = (1, 0, 0)^T$. In this case, \mathbb{T}_{yz}^2 is the only orthogonal slice with a non-zero Chern number, and as such the material lattice can be thought of as a stack of 2D Chern insulators spanning the y and z directions, stacked together in the x direction. \mathbb{T}_{yz}^2 can effectively be considered the Brillouin zone of such a 2D Chern insulator.

Recall from our discussion in Section 3.3.1 that a 2D Chern insulator with a Chern number of 1 has a single chiral edge mode, which manifests as a gapless state on the one-dimensional surface Brillouin zone. This logic can be translated to the three-dimensional case, where such slices are stacked in the x direction. Suppose there is a projection π along the z direction, onto a two-dimensional surface Brillouin zone $\tilde{\mathbb{T}}_{xy}^2$. Then the two-dimensional slices \mathbb{T}_{yz}^2 project down to a one-dimensional loop $\pi(\mathbb{T}_{yz}^2) \cong S^1$ containing a single point-like gapless state. As the \mathbb{T}_{yz}^2 slice is moved around in the x direction, this band crossing point moves continuously along the y direction, by continuity of the Hamiltonian. It follows that the full two-dimensional surface Brillouin zone must contain a loop of gapless states going across the x direction, as depicted in the figure. This loop is called a *Fermi loop*, in analogy with the Fermi arcs in a Weyl semimetal. Moreover, the chirality of the edge modes can be used to assign a consistent orientation to this loop.

Fermi loops admit a natural topological description in terms of homology. Being oriented loops, they precisely represent a class in the first homology group $H_1(\tilde{\mathbb{T}}^2)$ of the surface Brillouin zone. Furthermore, it is possible to define an oriented *Dirac loop* ℓ in the bulk Brillouin zone in such a way that its projection $\pi(\ell)$ onto the surface in any direction is exactly the Fermi loop. This loop ℓ is not a physically observable feature,⁹ but it is rather interesting topologically: it represents a first homology class in the bulk Brillouin zone,

$$[\ell] \in H_1(\mathbb{T}^3) \cong \mathbb{Z}^3.$$

It is not a coincidence that this first homology group is isomorphic to the second cohomology group $H^2(\mathbb{T}^3)$ from Equation (4.4). This equivalence is a result of

⁸Just as in the two-dimensional case, \mathcal{F} technically represents a class in the real-valued de Rham cohomology group $H_{dR}^2(\mathbb{T}^3) \cong \mathbb{R}^3$.

⁹Dirac loops do still admit a physical interpretation: they represent points at which the Berry connection \mathcal{A} has a gauge singularity. Such singularities depend on the choice of gauge, meaning the loop can be moved around by gauge transformations; however, this does not change their topology. The same goes for the Dirac strings that will be discussed in a moment.

Poincaré duality, which is the statement that for any closed oriented d -dimensional manifold M , the isomorphism

$$H_n(M) \cong H^{d-n}(M)$$

holds for any integer n . In the present case, this duality can be stated intuitively in terms of Chern numbers, which count the number of signed intersections of the Dirac loop with the different two-dimensional slices of the Brillouin zone.¹⁰ This duality can be summarised schematically as follows:

$$H^2(\mathbb{T}^3) \ni [\mathcal{F}] \xrightleftharpoons{\text{integration}} \mathbf{C} \xrightleftharpoons{\text{intersections}} [\ell] \in H_1(\mathbb{T}^3). \quad (4.5)$$

This Poincaré duality ensures that the classifications in terms of first homology and second cohomology are completely equivalent in this case. Importantly, however, Poincaré duality depends on orientability, and it will not hold when we consider non-orientable Brillouin zones in the next chapter. As such, the question of which group provides the right classification of such a system will be key. For the moment, we turn our attention to the topology of Weyl points in the simpler orientable setting.

4.2.2 Topology with Weyl points

Consider a Weyl semimetal with a set of k Weyl points

$$W \equiv \{w_1, w_2, \dots, w_k\} \subset \mathbb{T}^3.$$

Then the charge of a Weyl point w_i is given by the Chern number

$$C_w = \frac{1}{2\pi} \int_{S_w^2} \mathcal{F},$$

where S_w^2 is a sufficiently small 2-sphere centred at w —in particular, it must be small enough to contain no other Weyl points in its interior. Naively, this might lead us to expect that a semimetal phase is classified by the second cohomology group of the collection of all these spheres:

$$H^2 \left(\bigcup_{i=1}^k S_{w_i}^2 \right) \cong \bigoplus_{i=1}^k H^2(S_{w_i}^2) \cong \mathbb{Z}^k. \quad (4.6)$$

However, this classification runs into two problems: it ignores the global cancellation of charge, and it also ignores the additional topology on two-dimensional slices discussed in the previous subsection. Both of these issues are due to the fact that this group only captures the *local* topology near each Weyl point, and they can be addressed by studying how the different Chern numbers on the Brillouin zone must relate to each other *globally*.

¹⁰In general, it is possible that a single Dirac loop “folds back on itself” and intersects such a slice more than once. However, any additional intersections introduced in this way always come in oppositely-oriented pairs, leaving the topology unchanged.

The Nielsen–Ninomiya charge cancellation theorem is one such global relation. It is the statement that all the Chern numbers on these 2-spheres must add to zero:

$$\sum_{i=1}^k C_{w_i} = 0. \quad (4.7)$$

This cancellation can be demonstrated using Stokes' theorem. The argument goes as follows: imagine that the interior of each sphere $S_{w_i}^2$ (i.e. a small open 3-ball centred at w_i) is removed from \mathbb{T}^3 . The resulting 3-manifold X looks like a 3-torus with k small ball-shaped holes, and its boundary is given by the collection of spheres:

$$\partial X = - \bigcup_{i=1}^k S_{w_i}^2,$$

where the minus sign induces the correct orientation. Then Stokes' theorem gives

$$0 = \frac{1}{2\pi} \int_{\partial X} d\mathcal{F} = - \sum_{i=1}^k \frac{1}{2\pi} \int_{S_{w_i}^2} \mathcal{F} = - \sum_{i=1}^k C_{w_i},$$

which is precisely the Nielsen–Ninomiya theorem.

A similar argument can also be applied to study what happens to Chern numbers on two-dimensional slices of the Brillouin zone in this context. This argument is illustrated in Figure 4.6. Here, two slices \mathbb{T}_L^2 and \mathbb{T}_R^2 are placed on either side of

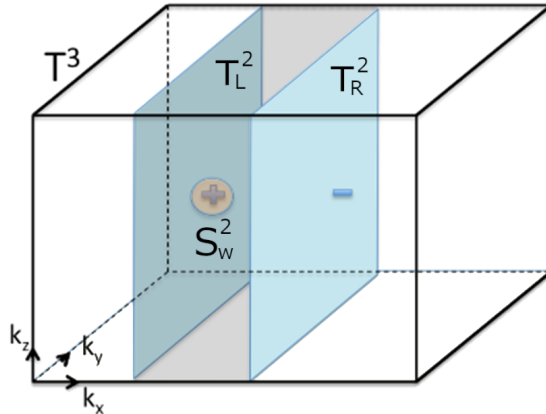


Figure 4.6: Figure adapted from Ref. [7]. Brillouin torus \mathbb{T}^3 of a Weyl semimetal with two oppositely charged Weyl points labelled + and -. Three two-dimensional subspaces are indicated in blue: a yz -like 2-torus $\mathbb{T}_{L,R}^2$ on either side of the + point, and a small 2-sphere S_w^2 surrounding it. Given the proper orientation, the blue spaces form the boundary of a three-dimensional manifold Y , shaded in grey here.

a Weyl point w with charge $C_w = q$, along with a small sphere S_w^2 surrounding it. These spaces then bound a three-dimensional manifold Y as indicated in the figure, given the following orientations:

$$\partial Y = \mathbb{T}_R^2 - \mathbb{T}_L^2 - S_w^2.$$

The same Stokes' theorem argument can then be used to relate the Chern numbers C_L and C_R on the respective slices, yielding

$$C_R = C_L + C_w = C_L + q.$$

That is, the Chern number of a two-dimensional slice increases by q every time it passes over a Weyl point with charge q . As a sanity check, it should be noted that this process respects the periodicity of the Brillouin torus: when the slice is passed over the entire torus, charge cancellation ensures that the added Chern number is zero in total.

All in all, the presence of Weyl points allows for a finer collection of Chern numbers to appear in the Brillouin zone, beyond the \mathbb{Z}^3 Chern vector of the insulating case. This behaviour can be captured using cohomology. The key idea is that the Berry curvature has a singularity at points where the gap closes.¹¹ As such, it can only be integrated over subspaces where the gap never closes, so that the set of Weyl points W needs to be excluded. This means \mathcal{F} now lives in the second cohomology group of the Brillouin zone minus W :

$$[\mathcal{F}] \in H^2(\mathbb{T}^3 \setminus W) \cong \mathbb{Z}^3 \oplus \mathbb{Z}^{k-1}, \quad (4.8)$$

where k again is the number of Weyl points. Put differently, classification of semimetallic phases given a set of Weyl points W essentially amounts to classifying the gapped phases on the punctured torus $\mathbb{T}^3 \setminus W$.

Notably, this classification addresses both issues present in the \mathbb{Z}^k classification on 2-spheres in Equation (4.6). Firstly, it incorporates 3D Chern insulator topology in the first term, in the form of the \mathbb{Z}^3 from Equation (4.4). Perhaps more subtly, charge cancellation is also incorporated in the form of the reduction by one \mathbb{Z} factor in the second term. This can be understood intuitively: for example, if $k = 1$ then the Nielsen–Ninomiya theorem implies that the single Weyl point must have a charge of 0, and so it is not topologically protected. A similar intuition holds for $k > 1$: in this case, the Weyl point charges $C_{w_i} \in \mathbb{Z}$ can be thought of as k parameters of the system, which are subject to the single constraint in Equation (4.7)—resulting in $k - 1$ effective \mathbb{Z} -valued degrees of freedom. This line of reasoning will become more explicit once the Mayer–Vietoris sequence is introduced in Section 4.2.3.

Fermi arcs

The varying Chern numbers over Weyl points help explain how Fermi arcs arise on the surface. As discussed in the case of a 3D Chern insulator, Fermi loops on the surface arise whenever there is a non-zero Chern number in some direction. Similarly, Fermi arcs begin and terminate whenever the presence of a Weyl point causes a change in the Chern number; this is illustrated in Figure 4.7.

This feature of Weyl semimetals implies they can mediate phase transitions between 3D Chern insulators with different Chern vectors. For example, suppose a pair of Weyl points is created at some point in the Brillouin zone of a trivial

¹¹Note that this singularity is required in order for the Chern number to change suddenly when a slice (i.e. the integration domain of \mathcal{F}) is moved over a Weyl point continuously.

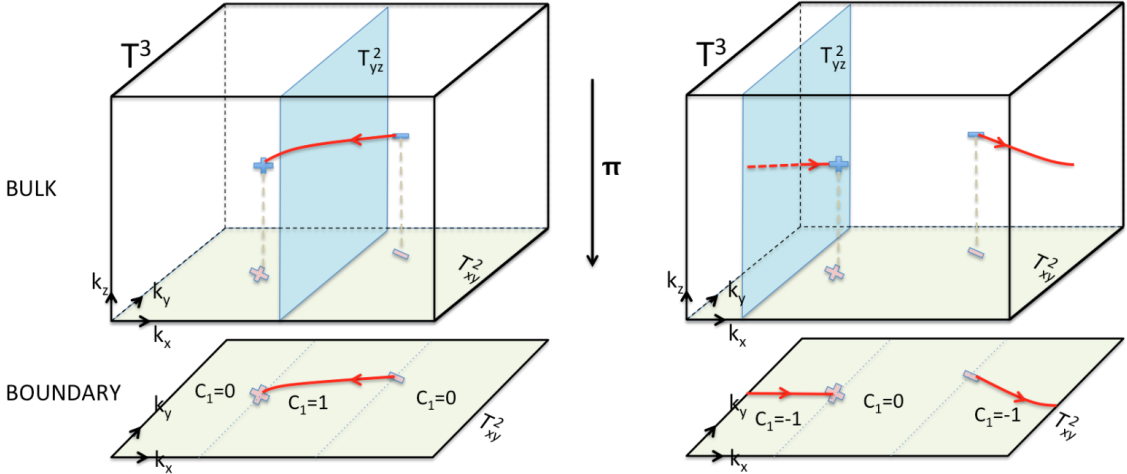


Figure 4.7: Figure from Ref. [7]. Two semimetal Brillouin zones are shown with the same configuration of Weyl points, but featuring topologically distinct Fermi arcs (shown in red on the boundary). The distinction is due to different bulk Chern numbers: Fermi arcs appear in regions where the bulk Chern number is non-zero. These Fermi arcs can be considered to be the projection of a Dirac string (shown in red in the bulk).

insulator ($\mathbf{C} = 0$). These points can then be moved apart in the z direction until they meet again and annihilate at the other end of the torus. In the process, a Fermi arc extends between the projections of the Weyl points on the xz and yz -planes, which eventually closes into a Fermi loop. In its final state, the system features a non-zero Chern vector of $\mathbf{C} = (0, 0, 1)^T$.

This process was first observed experimentally in a seminal work by Gui-Geng Liu et al. in 2022 [73]. The authors construct a photonic crystal, which is a type of artificial crystal where the different energy levels are represented by frequencies of light. Under application of a magnetic field, this crystal undergoes a transition between trivial and topological insulating phases, mediated by the creation and annihilation of two Weyl points; see Figure 4.8. This was also the first experimental realisation of a 3D Chern insulator, and of a system featuring a single Fermi arc.

Just as Fermi loops can be considered projections of a bulk Dirac loop, so too can Fermi arcs be considered a projection of a bulk *Dirac string*.¹² Like Dirac loops, these strings can be given an interpretation in terms of homology. The setup is somewhat more subtle in this case: since the Dirac strings have a boundary, they are not loops and as such do not represent homology classes in $H_1(\mathbb{T}^3)$. Instead, they represent classes in the *relative homology group*

$$H_1(\mathbb{T}^3, W) \cong \mathbb{Z}^3 \oplus \mathbb{Z}^{k-1} \quad (4.9)$$

with respect to the set of Weyl points $W \subset \mathbb{T}^3$. Intuitively, taking the relative homology means that any boundaries lying in the subset W are ignored; for a more precise definition the reader is referred to Ref. [32, §2.1].

¹²A more or less equivalent concept is referred to as *Euler chain* in Ref. [7], placing the emphasis on topology over physics: “chain” here refers the oriented subspaces that homology is founded on.

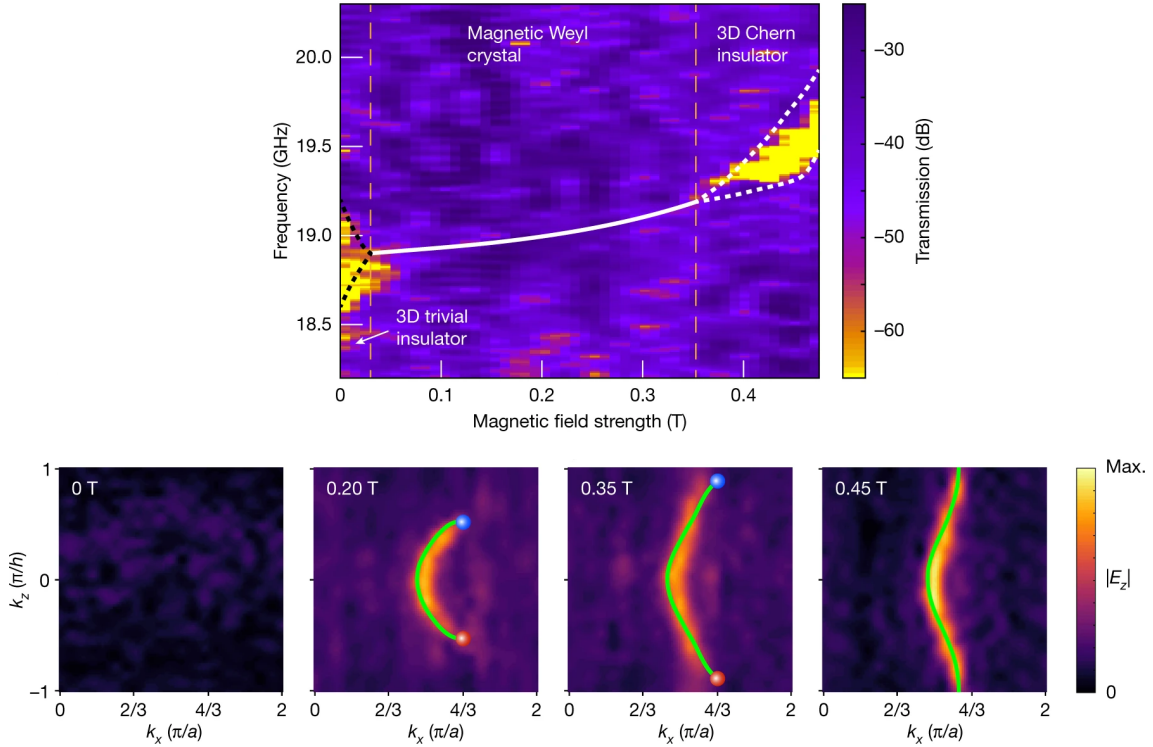


Figure 4.8: Figure from Ref. [73]. Top: measured frequency response (i.e. “band structure”) at increasing magnetic field strength. Yellow regions represent a band gap in the spectrum, indicating insulating phases. The white line represents the calculated frequency of the two Weyl nodes in the system. Bottom: measured response on a surface Brillouin zone, at the frequencies indicated on the white line above. Simulated Fermi arcs and loops are shown in green. A Fermi loop can clearly be seen to form, confirming a phase change to a topological insulator.

This homology picture provides a classification scheme that is exactly dual to the cohomology classification in Equation (4.8); that is, there is an isomorphism

$$H^2(\mathbb{T}^3 \setminus W) \cong H_1(\mathbb{T}^3, W). \quad (4.10)$$

This is not a direct Poincaré duality, but it is nevertheless mathematically rigorous and protected by orientability in the same way.¹³ The interpretation in terms of Chern numbers given in Equation (4.5) also still holds here, with the Chern vector and Dirac loops replaced with more general Chern numbers and Dirac strings, respectively.

¹³To be precise, Poincaré duality does not hold directly because $\mathbb{T}^3 \setminus W$ is not a closed manifold. Instead, for non-compact manifolds M there is a generalised duality $H^n(M) \cong H_{d-n}^{\text{BM}}(M)$ where the group on the right is the *Borel-Moore homology*, and this is in turn equivalent to the relative homology in this case. Alternatively, Equation (4.10) can be interpreted as a result of the so-called *Lefschetz duality* $H^n(M) \cong H_{d-n}(M, \partial M)$ for manifolds with a boundary.

4.2.3 The semimetal Mayer–Vietoris sequence

In the previous section, a heuristic Stokes’ theorem argument was presented for charge cancellation on Weyl points. This argument can be generalised by moving to a more abstract cohomology setting, where we are not dependent on the integration of forms; this is important because integration will not be well defined once we move to a non-orientable setting. As an added bonus, the abstract description proves to be richer and provide more detailed information on the possible topological phases for a Weyl semimetal.

The idea is that the relation between the global semimetal topology in Equation (4.8) and the local charge data in Equation (4.6) can be understood by considering how cohomology classes are mapped between them. That is, one needs to find and study a homomorphism

$$\beta : H^2(\mathbb{T}^3 \setminus W) \rightarrow \bigoplus_{w \in W} H^2(S_w^2).$$

Such a map arises naturally in the context of the *Mayer–Vietoris sequence* for cohomology.

Mayer–Vietoris sequences are used to study how the homology or cohomology groups of a topological space relate to those of subspaces that divide it up. To be precise, let X be a topological space and let $A, B \subset X$ be two subspaces that cover it (i.e. their union $A \cup B$ is equal to X). Then, there is an *exact sequence* of homomorphisms between cohomology groups,

$$\cdots \rightarrow H^n(X) \xrightarrow{\alpha} H^n(A) \oplus H^n(B) \xrightarrow{\beta} H^n(A \cap B) \rightarrow H^{n+1}(X) \rightarrow \cdots ,$$

where $A \cap B$ denotes the intersection of A and B . This sequence repeats in both directions, including all non-zero cohomology groups of the relevant spaces. Exactness means that the image of each map in the sequence is exactly equal to the kernel of the next, e.g. $\text{im}(\alpha) = \ker(\beta)$ for the labelled maps. In other words, the elements in each term in the sequence which are mapped to zero in the next term are precisely those which “descend” from the previous term. In particular, the composition of two subsequent maps always yields zero.

In the context of a Weyl semimetal, there is a natural way to divide the Brillouin torus \mathbb{T}^3 into two subspaces; this is illustrated in Figure 4.9. The first subspace in the covering is the punctured torus $\mathbb{T}^3 \setminus W$; we have already encountered this space in classifying topological semimetal phases. The other is the collection $\bigcup_{i=1}^k D_{w_i}^3$ of small open 3-balls centred on the Weyl points w_i . The intersection of these two spaces is the same collection of open balls, but each with a single puncture. For our purposes, this intersection has the same topology as the collection of 2-spheres $\bigcup_{i=1}^k S_{w_i}^2$ that we encountered in the context of local Weyl point charges.¹⁴ A Mayer–Vietoris sequence can now be written down for these subspaces. The section of this sequence which is

¹⁴To be precise, the punctured 3-balls can be *deformation retracted* into the 2-spheres, making them *homotopy equivalent*. Homotopy equivalent spaces have the same homology and cohomology groups.

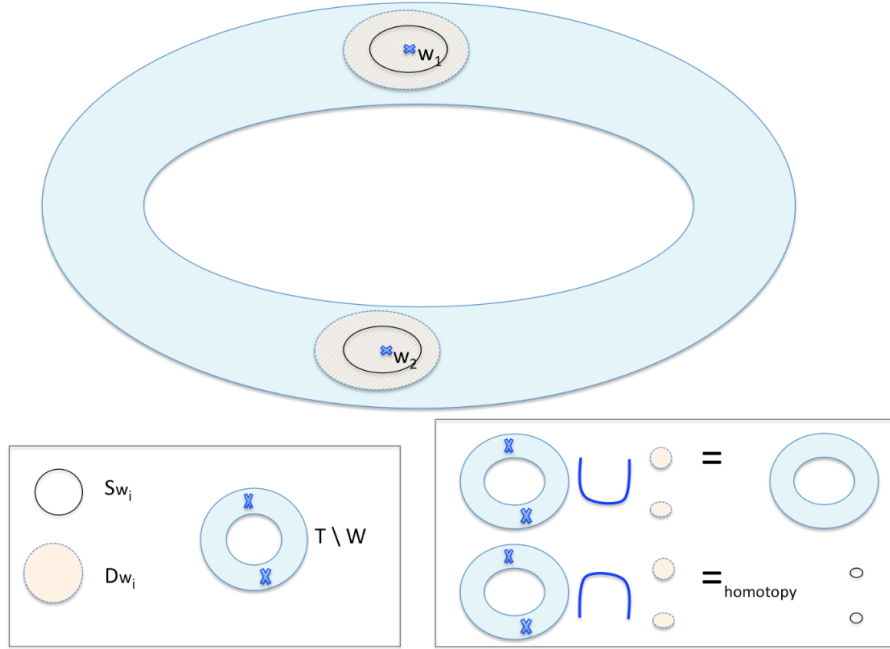


Figure 4.9: Figure from Ref. [7]. Schematic two-dimensional representation of the Brillouin torus and the subspaces used to cover it.

relevant to classification is referred to as the *semimetal Mayer–Vietoris sequence*:¹⁵

$$0 \rightarrow \underbrace{H^2(\mathbb{T}^3)}_{\text{3D Chern insulator}} \rightarrow \underbrace{H^2(\mathbb{T}^3 \setminus W)}_{\text{Semimetal}} \xrightarrow{\beta} \underbrace{\bigoplus_{w \in W} H^2(S_w^2)}_{\text{Local charges}} \xrightarrow{\Sigma} H^3(\mathbb{T}^3) \rightarrow 0. \quad (4.11)$$

The first three groups in this sequence are already familiar from Equations (4.4), (4.8), and (4.6) respectively. The last group $H^3(\mathbb{T}^3) \cong \mathbb{Z}$ is represented by volume forms¹⁶ on the torus; one notable example of such a form is the trivial 3-form

$$d\mathcal{F} = 0 \in H^3(\mathbb{T}^3)$$

which appeared in the Stokes' theorem arguments previously. Indeed, the map labelled Σ above can be loosely interpreted as the exterior derivative d . However, a more physically useful interpretation is that Σ gives the total charge in the system: it sends a set of Chern numbers on the Weyl points to their sum in \mathbb{Z} .

Explicitly, the semimetal Mayer–Vietoris sequence is¹⁷

$$0 \rightarrow \mathbb{Z}^3 \rightarrow \mathbb{Z}^3 \oplus \mathbb{Z}^{k-1} \xrightarrow{\beta} \mathbb{Z}^k \xrightarrow{\Sigma} \mathbb{Z} \rightarrow 0. \quad (4.12)$$

The exactness of this sequence can be used to extract useful information, especially around the group of local charges \mathbb{Z}^k . Here, exactness means that $\text{im}(\beta) = \ker(\Sigma)$.

¹⁵Note that the open balls $D_{w_i}^3$ do not appear in this sequence at all. This is because they can be contracted to a point, and hence are topologically trivial in a sense.

¹⁶I.e. 3-forms, which are locally proportional to $dk_x \wedge dk_y \wedge dk_z$.

¹⁷In principle the direct sum in the semimetal group has little mathematical significance; we write $\mathbb{Z}^3 \oplus \mathbb{Z}^{k-1}$ instead of \mathbb{Z}^{k+2} to aid the physical interpretation.

This implies that the local charges on the Weyl points sum to zero if and only if they descend from a semimetal. In other words, it implies not only the Nielsen–Ninomiya charge cancellation theorem, but also its converse: any set of Weyl points with charges adding to zero is admissible as a topological Weyl semimetal phase.

In fact, more can be inferred by looking at the maps around the semimetal group $\mathbb{Z}^3 \oplus \mathbb{Z}^{k-1}$. Here, exactness tells us that $\ker(\beta) \cong \mathbb{Z}^3$. This makes physical sense: β returns the local charge of each Weyl point, and if all these charges are zero, then none of the Weyl points are topologically protected and the system is really in a 3D Chern insulator phase. However, since β is a homomorphism,¹⁸ we also find $\beta^{-1}(c) \cong \mathbb{Z}^3$ for any valid charge configuration $c \neq 0 \in \text{im}(\beta)$; that is, every configuration with a total charge of zero admits a \mathbb{Z}^3 of topologically different semimetal phases, which are in one-to-one correspondence with the \mathbb{Z}^3 of insulating phases. This makes precise a principle that is also hinted at in Figure 4.7: Weyl semimetals with identical charge configurations may nevertheless be topologically distinct, and their topologies differ by a bulk Chern vector in \mathbb{Z}^3 .¹⁹

The dual homology sequence

In previous subsections, we have already seen that the cohomology invariants on Chern insulators and Weyl semimetals can be understood equally well in terms of homology groups. As it turns out, this duality can be extended to the semimetal Mayer–Vietoris sequence (4.11). The dual of the first two groups was already explored in Equations (4.5) and (4.10). The latter two groups act on closed manifolds, and so their dual can be obtained from Poincaré duality directly:

$$\bigoplus_{w \in W} H^2(S_w^2) \cong \bigoplus_{w \in W} H_0(S_w^2), \quad H^3(\mathbb{T}^3) \cong H_0(\mathbb{T}^3).$$

In both cases, we have a top-dimensional cohomology group (containing volume forms) being dualised to a zeroth homology group, which counts the number of connected components. In particular, since the connected components are the important aspect, the 2-spheres S_w may be substituted for the Weyl points w to simplify:

$$\bigoplus_{w \in W} H_0(S_w^2) \cong \bigoplus_{w \in W} H_0(w) \cong H_0(W).$$

The complete homology dual of (4.11) is then

$$0 \rightarrow \underbrace{H_1(\mathbb{T}^3)}_{\text{Dirac loops}} \rightarrow \underbrace{H_1(\mathbb{T}^3, W)}_{\text{Dirac strings}} \xrightarrow{\partial} \underbrace{H_0(W)}_{\text{Local charges}} \xrightarrow{\Sigma} H_0(\mathbb{T}^3) \rightarrow 0. \quad (4.13)$$

This exact sequence has arisen through taking Poincaré duals of groups in the Mayer–Vietoris sequence, but somewhat miraculously, it continues to be valid even in

¹⁸This is a result of the *first isomorphism theorem*, which in particular implies that all the pre-images of β are isomorphic to its kernel $\beta^{-1}(0)$.

¹⁹Properly speaking, the set of topological phases for a given charge configuration is an *affine space* for $H^2(\mathbb{T}^3)$, since there is no canonical zero Chern vector on a Weyl semimetal. This is worked out in greater mathematical detail in Section 3 of Ref. [7].

the absence of Poincaré duality (e.g. on a non-orientable manifold). In fact, it can be considered a more fundamental sequence in some ways: it describes the homology of the torus with respect to a single subspace W , whereas the Mayer–Vietoris sequence relies on multiple subspaces that cover the torus.²⁰

The map indicated by ∂ is the boundary map that is used to define homology groups in the first place.²¹ In this case, it sends classes of oriented Dirac strings in the bulk to the Weyl points that bound them, with a sign given by which end of the string the points are on. For example, for a Weyl semimetal with two Weyl points $W = \{w_1, w_2\}$ connected by a Dirac string s , we have $[s] \in H_1(\mathbb{T}^3, W)$ and

$$\partial([s]) = (1, -1) \in H_0(W) \cong \mathbb{Z}^2.$$

This gives rise to a very natural interpretation of charge cancellation: it automatically follows from the fact that Weyl points on opposite ends of a Dirac string are assigned opposite signs. These opposite charges are then summed to zero by the total charge map Σ , i.e. $\Sigma \circ \partial = 0$. This can also be inferred from the exactness of (4.13), which additionally tells us that there exists a configuration of Dirac strings compatible with any set of Weyl points with total charge zero.

As emphasised before, this homology sequence encodes exactly the same information as the cohomology Mayer–Vietoris sequence in the simple case where Poincaré duality is preserved. However, once symmetries are imposed on the system, this duality may be altered, in which case the two basic sequences become essentially different. It then becomes necessary to study how the cohomology and/or homology groups must be altered to encode relevant information about the topological phases of the system. We will review one example of this in the next section.

4.2.4 Time-reversal symmetric Weyl semimetals

The preceding topological review of Weyl semimetals has thus far been in the context of the basic symmetry class A—that is, we have not imposed any additional symmetries on the system. However, such additional symmetries are not necessarily forbidden in a Weyl semimetal: the type A classification merely tells us that the semimetal topology is very robust, not relying on any symmetry protection.²² As discussed in Section 4.1.3, most of the experimentally observed electronic Weyl semimetals actually preserve time-reversal symmetry, which is a natural condition in the absence of a magnetic field. An excellent topological description of such systems was published by Guo Chuan Thiang, Koji Sato and Kiyonori Gomi in 2017, and we will spend the rest of this section reviewing its main aspects [85].

Time-reversal symmetric systems belong to class AII of the tenfold way classification in Table 3.1, meaning that the underlying insulating topology (i.e. the

²⁰Indeed, this is the first exact sequence introduced in the standard algebraic topology textbooks, e.g. in Theorem 2.13 of Ref. [32].

²¹To be precise, homology is defined using boundaries of chains; the present map is the *pushforward* of the boundary map, and one can think of it as acting on the chains that represent different homology classes.

²²By contrast, for example, the SSH model introduced in Section 3.1 has chiral symmetry-protected topological phases.

topology with zero Weyl points) is that of the strong and weak insulators described in Section 3.3.3. The four \mathbb{Z}_2 invariants (three weak and one strong) in such systems also play a role in the semimetal topology. Just as class A Weyl semimetals can be considered intermediate phases between different 3D Chern insulators (as shown in Figure 4.8), it is shown in Ref. [85] that class AII semimetals can mediate phase transitions between different strong and weak 3D insulators via Weyl point creation and annihilation.

As discussed in Section 4.1, time reversal symmetry squaring to $T^2 = -1$ forces Weyl points to appear in pairs of the same chirality, related by $\mathbf{k} \leftrightarrow -\mathbf{k}$ in the Brillouin zone. The topology induced by the presence of these pairs must also respect the symmetry, and as such it cannot be studied by simply moving integration planes freely over the individual Weyl points (as previously shown in Figure 4.6). Indeed, recall from Section 3.3.3 that the insulating \mathbb{Z}_2 invariants must be calculated specifically at the T -invariant planes sitting at $k_{x,y,z} \in \{0, \pm\pi\}$. To study how symmetric pairs of Weyl points affect these invariants, their respective planes must be continuously deformed across them in a way that respects the symmetry, leading to the concept of *curved T-planes*; see Figure 4.10.

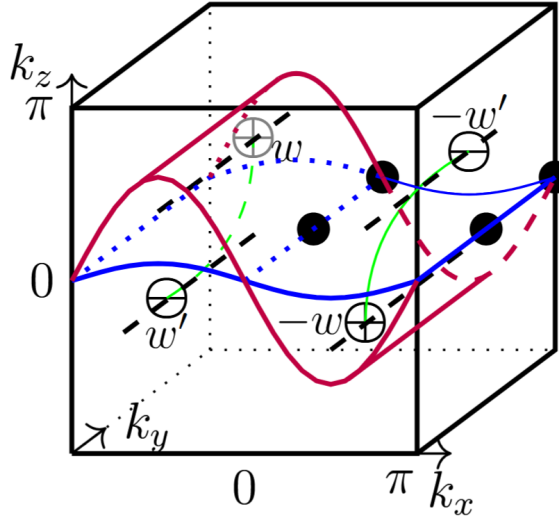


Figure 4.10: Figure from Ref. [85]. Curved T -planes are shown in blue and purple; both are deformations of the $k_z = 0$ plane. Deforming the blue plane into the purple one makes it cross the pair of Weyl points at $\mathbf{k} = \pm w$. This induces a change in the related \mathbb{Z}_2 invariant: if the points in this pair have individual charges of q , then the invariants on these planes are related by $\Delta_{z,0}^{\text{purple}} \equiv \Delta_{z,0}^{\text{blue}} + q \pmod{2}$.

The cohomology description must be altered in several ways in order to accommodate this more complex topology. First of all, the cohomology classes must respect the $\mathbf{k} \leftrightarrow -\mathbf{k}$ symmetry on the Brillouin zone, leading to the use of *equivariant* cohomology groups $H_{\mathbb{Z}_2}^n$, where the \mathbb{Z}_2 stands for the \mathbb{Z}_2 action of the symmetry. Mathematically, this is similar in spirit to studying the topology of the *effective Brillouin zone* covering half the torus \mathbb{T}^3 , obtained from the quotient $\mathbb{T}^3/\mathbb{Z}_2$ of the symmetric action. However, the presence of high-symmetry points means some

topological information is lost in passing to this effective Brillouin zone, and so a somewhat more involved construction called the *homotopy quotient* must be employed instead.²³

Secondly, the non-trivial topology existing at the time-reversal invariant momenta (TRIM) necessitates that the cohomology groups be calculated relative to these points. This relative cohomology is defined in much the same way as the relative *homology* featured in Equation (4.9).

Lastly, the cohomology must be *twisted*; that is, rather than the normal integer coefficients, it is endowed with *local coefficients* $\tilde{\mathbb{Z}}$, which change sign under the \mathbb{Z}_2 action of the symmetry. We will provide a more geometric intuition behind these local coefficients in Section 5.2.

All in all, the regular cohomology groups in the Mayer–Vietoris sequence in Equation (4.11) must be changed to rather complicated *twisted equivariant* cohomology *relative* to the TRIM. For example, the insulating invariants (i.e. Chern vectors) in $H^2(\mathbb{T}^3) \cong \mathbb{Z}^3$ are altered to

$$H_{\mathbb{Z}_2}^2(\mathbb{T}^3, \text{TRIM}; \tilde{\mathbb{Z}}) \cong \mathbb{Z}_2^4,$$

containing precisely the four \mathbb{Z}_2 invariants: three weak and one strong. The use of this form of cohomology is motivated in Ref. [85] by the classification of so-called “Quaternionic” vector bundle structures on the Brillouin zone, which are a modification of the usual complex vector bundles induced by the $T^2 = -1$ symmetry [60, 86].

The dual homology picture is somewhat simpler in this case. The only modification necessary to the groups in the homology sequence in Equation (4.13) is the use of equivariant homology $H_n^{\mathbb{Z}_2}$; that is, instead of generic Dirac loops and strings, the homology classes must be represented by their *T-stable* variants which respect the $\mathbf{k} \leftrightarrow -\mathbf{k}$ symmetry and avoid the TRIM. Just as in the type A system, this leads to an intuitive description of the associated invariants; see for example Figure 4.11.

Calculated using either homology or cohomology, the semimetal Mayer–Vietoris sequence takes on the following explicit form in a class AII system:

$$0 \rightarrow \mathbb{Z}_2^4 \rightarrow \mathbb{Z}_2^4 \oplus \mathbb{Z}^{r-1} \xrightarrow{\beta} \mathbb{Z}^r \xrightarrow{\Sigma} \mathbb{Z} \rightarrow 0, \quad (4.14)$$

where in this case, r labels the number of symmetric pairs rather than individual Weyl points. Its features are very much analogous to the class A sequence in Equation (4.12): it is essentially obtained by substituting the \mathbb{Z}^3 relating to insulating Chern vectors with a \mathbb{Z}_2^4 indexing the weak and strong invariants. Just as before, the map Σ can be used to deduce Nielsen–Ninomiya charge cancellation, and the semimetal group $\mathbb{Z}_2^4 \oplus \mathbb{Z}^{r-1}$ combines the insulating invariants on the left with a \mathbb{Z}^{r-1} representing the set of allowed Weyl point charge configurations. The main difference from the class A case is that the topology is framed in terms of pairs of

²³This homotopy quotient is obtained from the *Borel construction*, relying on the fact that there is always a contractible space EG (the total space of the so-called *universal bundle*, in this case S^∞) on which the symmetry group G acts freely. The product space $EG \times \mathbb{T}^3$ is then homotopy equivalent to \mathbb{T}^3 , but the diagonal action has no fixed points. Equivariant cohomology is defined as the cohomology of the quotient space of this action: $H_G^n(\mathbb{T}^3) := H^n(EG \times_G \mathbb{T}^3)$.

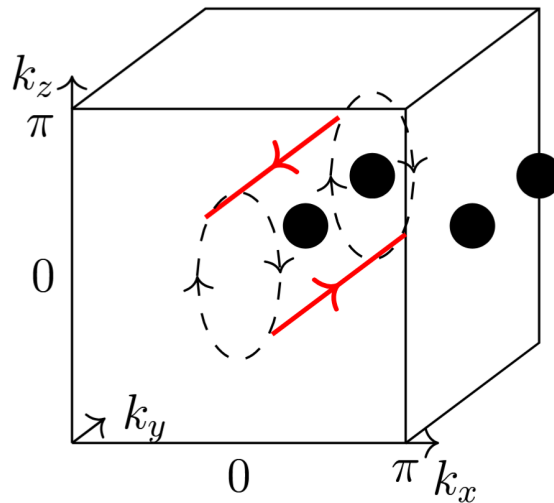


Figure 4.11: Figure from Ref. [85]. A T-stable pair of oriented Dirac loops l_y is shown spanning the k_y direction. The loops may be interchanged while maintaining T-stability, by rotating them along the dashed lines. Doing so recovers the original pair with opposite orientation. It follows that $l_y = -l_y$, that is, $2l_y = 0$; as a result, l_y generates a \mathbb{Z}_2 invariant, dual to the cohomology invariant ν_y .

Weyl points, and as such the minimum number of Weyl points is four instead of two—as we also covered in the physical setting of Section 4.1.3.

One might reasonably question whether the classification of Weyl semimetals with additional symmetries always comes down to a mere change in the underlying insulating topology, as it does in this case. In Chapter 5, we will discuss a counterexample to this: we show that the Mayer–Vietoris sequence is altered more radically under a symmetry which has previously been demonstrated to induce novel semimetal topology.

Chapter 5

Non-orientability and Weyl points

Symmetries play a crucial role in establishing and differentiating topological properties of physical systems; this is attested by the tenfold way classification discussed in Section 3.2. However, in recent years researchers have begun to recognise that symmetries beyond the standard time reversal, charge conjugation and chiral symmetries can give rise to distinct topological invariants that are not fully captured by this classification.

An important class of these extended symmetries is comprised by the space groups acting on periodic lattices. These impose additional structure on the unit cell of the lattice, such as rotational or reflection symmetry. The space groups may induce novel topological states when applied to a material lattice [87]; the classification of these states is covered exhaustively in Ref. [49]. Of special interest in this work are the so-called *non-symmorphic* space group symmetries, which combine basic rotation, reflection or inversion with fractional lattice translations. This type of symmetry features fewer high-symmetry points, and its effect on real-space lattices has been studied extensively [88–99]; a review can be found at Ref. [100].

Very recently, the feasibility of applying these non-symmorphic symmetries in momentum space has been demonstrated both theoretically and experimentally [21–25, 101–104]. This opens up new and interesting avenues of research relating to Brillouin zone topology. In particular, the Brillouin zone may become effectively non-orientable, challenging the notion of chirality for Weyl points.

We begin this chapter with a short review of existing literature surrounding these momentum-space non-symmorphic symmetries in Section 5.1, culminating in a treatment of a recent paper which applies them to Weyl semimetals. We then present a novel topological analysis of the system described in this paper in Section 5.2, in terms of the cohomology and homology tools presented in Chapter 4. We also develop a formalism for studying and interpreting semimetal invariants in a more general non-orientable setting. In Section 5.3, we provide a full classification of all possible non-orientable Brillouin zones in three dimensions, including explicit calculations of the semimetal Mayer–Vietoris sequence for each one. Finally, in Section 5.4, we apply the insights gained from these non-orientable systems to the important case of inversion-symmetric Weyl semimetals. Using a heuristic ansatz, we derive a semimetal Mayer–Vietoris sequence that appears to correctly classify the topological invariants of these systems.

5.1 Review of recent literature

Non-symmorphic symmetries have been studied somewhat extensively in real space, but their momentum space counterparts have long eluded study. There is a practical reason for this: normally, any space group symmetry in real space gives rise to a symmorphic (i.e. point group) symmetry in momentum space after Fourier transformation, regardless of the nature of the real space symmetry [101]. In order to obtain a non-symmorphic symmetry in momentum space, it is necessary to change how the real-space symmetry group acts on states in the Hilbert space. The reasoning is as follows: a symmetry group G acts on states in the Hilbert space through a representation ρ . This representation is normally a homomorphism, i.e. it obeys

$$\rho(g)\rho(h) = \rho(gh)$$

for $g, h \in G$. However, since quantum states are physically equivalent up to a $U(1)$ phase, the representation ρ may also include $U(1)$ factors:

$$\rho(g)\rho(h) = \nu(g, h)\rho(gh),$$

where $\nu : G \times G \rightarrow U(1)$ is known as a factor system [105]. Such a representation is called *projective*, and it may fundamentally alter the algebraic properties of the symmetry group—for example, it can lead symmetry operations that commute in real space to anticommute instead in Hilbert space. Projective representations have previously been studied in more abstract systems, and may give rise to novel topological phases on their own [105–110]. The usual strategy is to implement *gauge fluxes* on the real-space lattice; these are structures that induce $U(1)$ phase changes in particles hopping around the lattice.

The first theoretical realisation of non-symmorphic momentum space symmetries was published by Z. Y. Chen, Shengyuan Yang and Yuxin Zhao in 2022 [21]. In their work, the authors take a lattice with a mirror symmetry M_x and perpendicular translation symmetry L_y , and demonstrate how negative hopping amplitudes may be implemented in such a way that the resulting gauge fluxes make M_x and L_y anticommute rather than commute; see Figure 5.1(a). This anticommutation changes how the mirror operator acts in momentum space: denoting the momentum space operators by \hat{M}_x and $\hat{L}_y = e^{ik_y}$ (assuming unit lattice spacing in the real y direction), anticommutation implies

$$\hat{M}_x e^{ik_y} \hat{M}_x = -e^{ik_y} = e^{i(k_y + \pi)}.$$

That is, \hat{M}_x induces not only a mirroring $k_x \mapsto -k_x$, but also a translation by π in the k_y direction. It follows that the momentum-space Hamiltonian must obey the *glide symmetry*

$$U\mathcal{H}(k_x, k_y)U^{-1} = \mathcal{H}(-k_x, k_y + \pi). \quad (5.1)$$

Crucially, the action of this symmetry is free, i.e. there are no high-symmetry momenta that are fixed by \hat{M}_x . Similar to the way in which the free \mathbb{Z}^2 translation symmetries on the 2D lattice reduce momentum space from \mathbb{R}^2 down to the Brillouin torus \mathbb{T}^2 , this free \mathbb{Z}_2 glide symmetry reduces the Brillouin zone further down to a *fundamental domain* covering half of the torus from $k_y = -\pi$ to $k_y = 0$. Whereas the

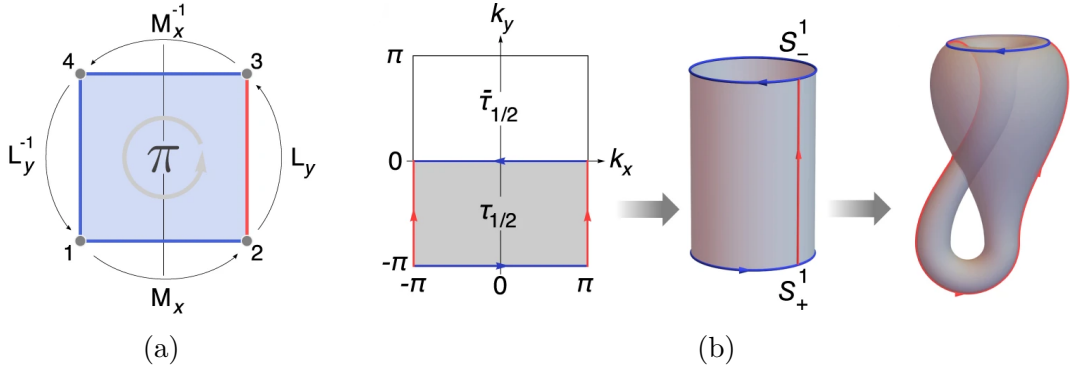


Figure 5.1: Figures adapted from Ref. [21]. (a) A square section of the lattice is shown with a negative hopping amplitude in red. This induces a phase change of π (i.e. a sign change) on a test particle which is moved around the square by successive symmetry operations $L_y^{-1}M_x^{-1}L_yM_x$. The operators M_x and L_y anticommute as a result. (b) The momentum space symmetry \hat{M}_x reduces the Brillouin torus to the fundamental domain shaded in grey on the left. The boundaries of this domain are identified along the red and blue arrows, upon which it assumes the topology of the Klein bottle K^2 (shown on the right). Much like a Möbius strip, this surface has only one side: in the illustration, the outside of the main bulb is connected to its inside via the funnel at the top. This means K^2 cannot be given a consistent orientation.

boundary conditions on the full torus are periodic, this fundamental domain features anti-periodic boundary conditions in the k_y direction, in the sense that the $k_y = -\pi$ and $k_y = 0$ boundaries must be identified with opposite orientations. Under these identifications, the fundamental domain assumes the topology of the Klein bottle K^2 , which is a non-orientable surface; see Figure 5.1(b).¹

A note on terminology is in order here: the fundamental domain is an instance of an effective Brillouin zone as we have defined it in Section 4.2.4, i.e. the quotient of the torus by the symmetry group. We use the more specific term “fundamental domain” to indicate that this region can be considered a true Brillouin zone in the absence of high-symmetry points. In this light, we avoid using the term “Brillouin zone” in isolation from here on to avoid confusion between the original Brillouin torus and this fundamental domain.

Returning to Ref. [21], the glide symmetric system is found to feature a \mathbb{Z}_2 invariant ν , different from the \mathbb{Z} invariant on the 2D Chern insulators discussed in Section 3.3.1. The difference may be explained in terms of cohomology: the regular Chern number is related to $H^2(\mathbb{T}^2) \cong \mathbb{Z}$, whereas in the case of the Klein bottle, the invariant is classified by $H^2(K^2) \cong \mathbb{Z}_2$. This \mathbb{Z}_2 invariant cannot be stated simply in terms of a Berry curvature integral on the fundamental domain: the boundaries at $k_y = -\pi$ and $k_y = 0$ are identified in opposite directions, and their contributions to the integral no longer cancel by Stokes’ theorem. Instead, the invariant takes the

¹Incidentally, Figure 5.1(b) serves as the inspiration for the cover page of this thesis.

following two forms in Ref. [21]:

$$\nu \equiv \frac{1}{2\pi} \int_{\tau_{1/2}} \mathcal{F} + \frac{1}{\pi} \gamma(0) \mod 2 \quad (5.2)$$

$$\equiv \frac{1}{2\pi} [\gamma(0) + \gamma(-\pi)] \mod 2, \quad (5.3)$$

where $\tau_{1/2}$ is the fundamental domain and $\gamma(k_y)$ is the Berry phase over the loop at k_y . These two forms are related by Stokes' theorem, and the modulus 2 is necessary to ensure gauge invariance.²

In 2023, Chen Zhang et al. (including two of the authors of the aforementioned Klein bottle paper) generalised this theoretical framework [101]. In particular, they specify how to obtain all 157 non-symmorphic symmetries in three dimensions (and all four in two dimensions) from real-space gauge symmetries.

Several experimental verifications of these momentum-space non-symmorphic symmetries were published in 2024: Ref. [22] by Yu-Liang Tao, Mou Yan et al. and Ref. [23] by Zhenxiao Zhu et al. In both works, a 3D acoustic lattice is constructed—an artificial crystal in which the band structure is represented by frequencies of sound waves—featuring negative hopping amplitudes, which induce non-symmorphic symmetries in momentum space; see Figure 5.2. These symmetries are shown to give rise to novel topological phases and surface behaviour.

Several other works have explored a specific non-symmorphic symmetry group in two dimensions, where besides the glide symmetry \hat{M}_x giving rise to Equation (5.1), there is also a perpendicular glide symmetry \hat{M}_y in which the roles of k_x and k_y are reversed [24, 102, 103]. This double glide symmetry is notable in that, even though the action of each individual glide symmetry \hat{M}_x and \hat{M}_y on the Brillouin torus is free, the combined action of the two is not. Instead, there are four high-symmetry momenta³ at $\mathbf{k} = (\pm\pi/2, \pm\pi/2)$ which are fixed under $\hat{M}_y \hat{M}_x$; see Figure 5.3. It is noted in Refs. [102] and [24] that a \mathbb{Z}_2 topological invariant can be calculated based on the eigenvalues of $\hat{M}_x \hat{M}_y$ at these high-symmetry points, similar to the \mathbb{Z}_2 invariants in the time-reversal invariant systems encountered in Section 3.3.

5.1.1 Non-orientable Weyl semimetals

The first work in which non-symmorphic symmetries were explored in the context of Weyl semimetals was a 2024 paper by André Grossi Fonseca, Sachin Vaidya et al. [25]. The remainder of this section is dedicated to summarizing the main findings in this paper.

The basic setup in Ref. [25] is that of an abstract 3D Brillouin torus featuring a glide symmetry of the form

$$\mathcal{H}(k_x, k_y, k_z) = \mathcal{H}(-k_x, k_y + \pi, k_z); \quad (5.4)$$

²Note that in the latter equation, it is important that $\gamma(0)$ and $\gamma(-\pi)$ are both calculated in the same gauge, which must be continuous across the fundamental domain $\tau_{1/2}$.

³In crystallographic terms, the 2D wallpaper group Pgg has four special Wyckoff positions.

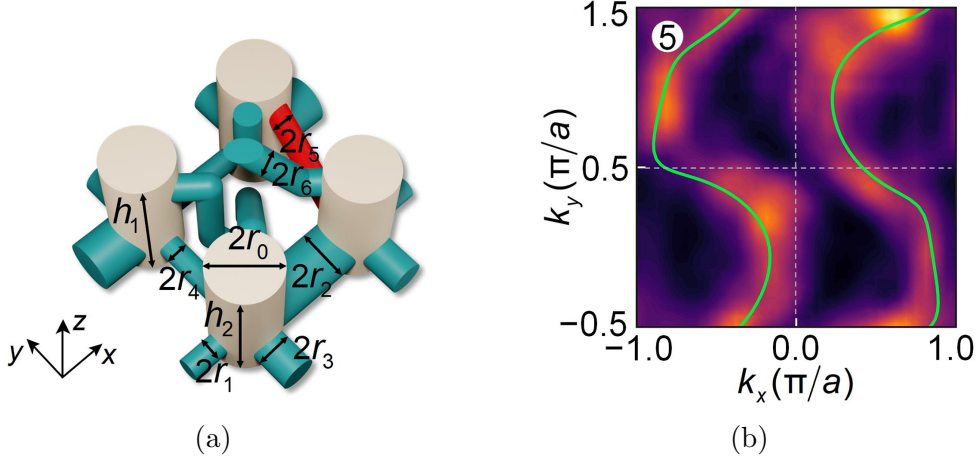


Figure 5.2: Figure adapted from Ref. [23]. (a) Unit cell of the acoustic crystal used in the experiment. The resonant cavities shown in beige approximate tight-binding orbitals in electronic systems, while the coupling tubes in green simulate hopping between lattice sites. The tube indicated in red has an effective negative hopping amplitude. (b) Experimental (colour map) and numeric (green) data from a 2D slice of the system's Brillouin torus. The figure shows the response to a specific frequency, equivalent to an equal-energy contour (i.e. section of the bands) in an electronic system. This 2D slice features a glide symmetry: the lower half can be obtained by mirroring the upper half in the horizontal k_x direction.

no assumptions are made on the source of this symmetry.⁴ The free action of this symmetry gives rise to a non-orientable fundamental domain: slices of constant k_z take on the topology of the Klein bottle K^2 in the same way as in Ref. [21] discussed above. Taking into account the additional periodic k_z direction, the total fundamental domain is topologically the non-orientable manifold $K^2 \times S^1$; see Figure 5.4. In Ref. [25], the fundamental domain is taken to be the half torus with $k_y \leq 0$, with additional boundary identifications between the planes $k_y = -\pi$ and $k_y = 0$ which respect the symmetry.

The non-orientability of the fundamental domain is shown to lead to some novel properties. Most notably, the chirality of Weyl points is no longer well-defined in a non-orientable setting: for example, when a Weyl point which has a Chern number of -1 leaves the fundamental domain at the $k_y = -\pi$ plane, it returns at the corresponding point on the $k_y = 0$ plane with a Chern number of $+1$. Physically, this is because the glide symmetry in Equation (5.4) is parity-reversing, which induces a sign change in the Berry curvature.

These chirality changes may result in a system in which the total chirality of Weyl points does not add to zero on the fundamental domain; that is, the Nielsen–Ninomiya charge cancellation theorem in Equation (4.7) is circumvented. In particular, two Weyl points with the same chirality may be connected by a Fermi arc on an xy -like

⁴The symmetry is presented without unitary conjugation, but as noted in the supplement to Ref. [25], the presence of such a conjugation [as in Equation (5.1)] makes no difference topologically.

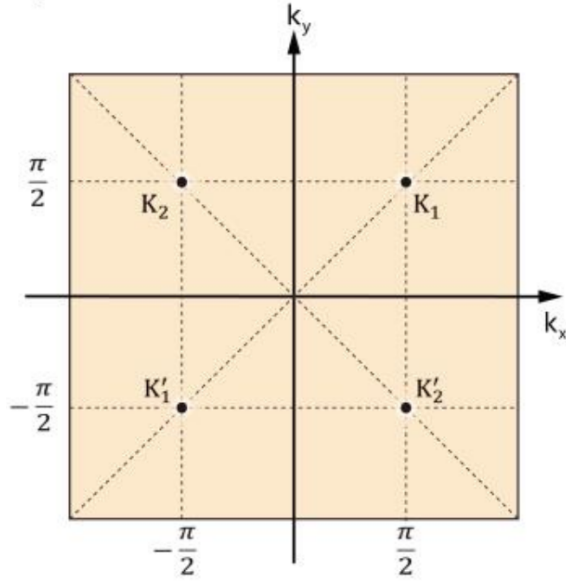


Figure 5.3: Figure from Ref. [24]. The points labelled K_a with $a \in \{1, 2\}$ are related by either single glide symmetry to those labelled K'_a respectively. As a result, applying both symmetries at once fixes all four of these points. The indicated dashed lines are also fixed sets of the combined symmetry.

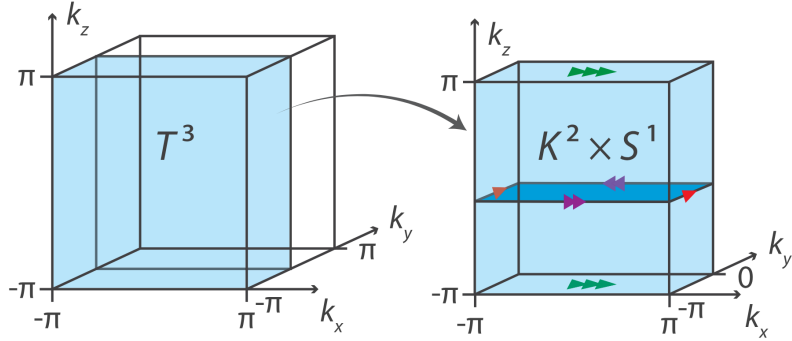


Figure 5.4: Figure adapted from Ref. [25]. The glide symmetry in Equation (5.4) acts on the Brillouin torus \mathbb{T}^3 in such a way that the fundamental domain (covering half the torus) is topologically $K^2 \times S^1$. Coloured arrows indicate the correct boundary identifications.

surface, see Figure 5.5. It is demonstrated that a Fermi arc on such a surface connects two same-chirality Weyl points if and only if it lies on an “orientation-reversing path”, i.e. it crosses the line at $k_y = 0$ an odd number of times.

Moreover, a new charge cancellation theorem is derived from a \mathbb{Z}_2 invariant ν existing on gapped K^2 -like slices of constant k_z . This invariant is equivalent to that on the Klein bottle insulator in Ref. [21], and is calculated using Equations (5.2) and (5.3). It is shown that this invariant changes whenever such a slice is moved across a Weyl point of odd chirality in the k_z direction, see Figure 5.6. It is then argued that, since the fundamental domain is periodic in the k_z direction, there must be an even number of such changes in ν . This leads to a novel \mathbb{Z}_2 charge cancellation condition

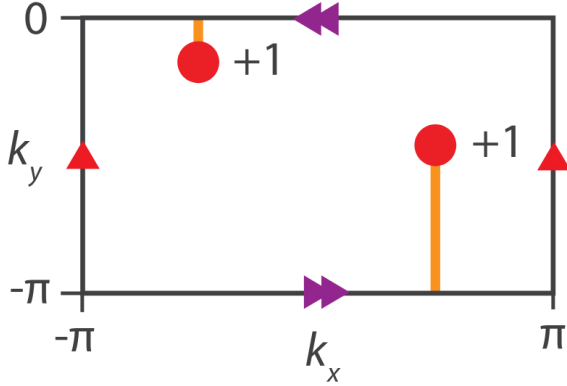


Figure 5.5: Figure from Ref. [25]. Surface Brillouin zone obtained from imposing open boundary conditions in the z direction. A Fermi arc is shown which connects (projections of) Weyl points of the same chirality. This Fermi arc crosses the orientation-reversing boundary at $k_y = 0$ once (i.e. an odd number of times).

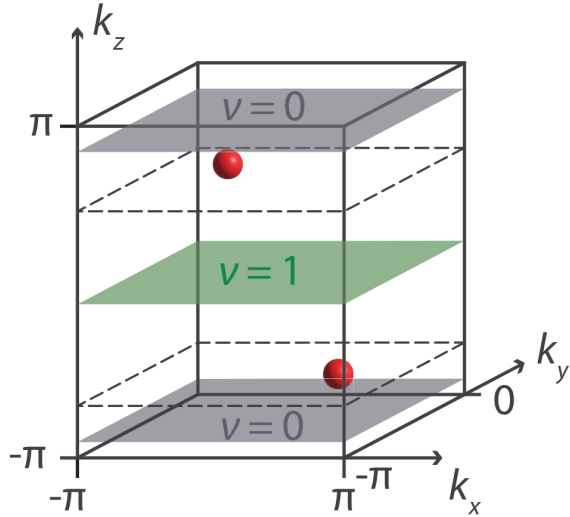


Figure 5.6: Figure from Ref. [25]. The $K^2 \times S^1$ fundamental domain is shown featuring two Weyl points, both with chirality +1. The invariant ν is shown to vary in the k_z direction, depending on the presence of Weyl points. Periodicity in the k_z direction then dictates that the total parity of the Weyl points must be even.

for Weyl points on $K^2 \times S^1$: if there are k Weyl points $w_i \in W$ in the fundamental domain, then their Chern numbers C_{w_i} must obey

$$\sum_{i=1}^k C_{w_i} = 0 \pmod{2}. \quad (5.5)$$

Finally, Ref. [25] includes an experimental realisation of a Weyl semimetal with momentum-space glide symmetry. The authors make use of one-dimensional photonic crystals, whose longitudinal coordinate z represents the z direction inside a three-dimensional semimetal. The optical properties of the unit cells of each crystal are

parametrised by two periodic variables k_1 and k_2 , which effectively act as synthetic versions of the momenta k_x and k_y . These synthetic momenta are made to obey the glide symmetry in Equation (5.4), in such a way that the resulting system acts like a Weyl semimetal with two Weyl points of equal chirality in the fundamental domain. The optical crystals are then truncated in the z direction, so that surface states on the K^2 -like (k_x, k_y) surface may be probed at specific momenta. In this way, a Fermi arc is demonstrated which terminates in two points of similar chiralities; see Figure 5.7.

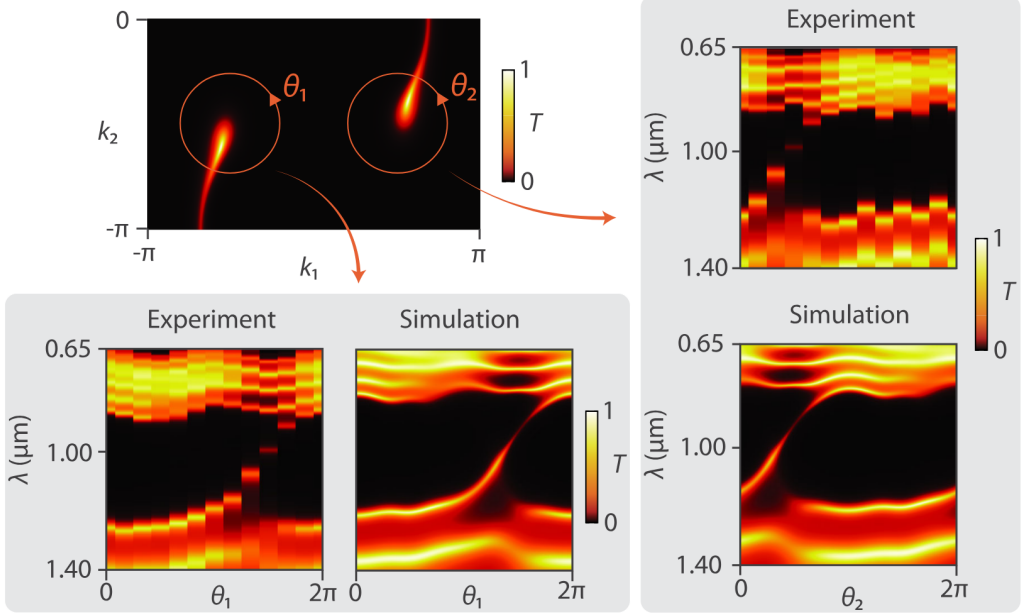


Figure 5.7: Figure from Ref. [25]. Top left: simulated K^2 surface Brillouin zone featuring a Fermi arc that crosses the orientation-reversing boundary at $k_2 = -\pi \sim 0$. Two circular contours are shown, parametrised by θ_1 and θ_2 . Bottom left: experimental (photonic) samples are prepared for several discrete values of θ_1 , with their synthetic momenta matched to the (k_1, k_2) corresponding to θ_1 . The plots show the frequency response (i.e. band structure) on the surface Brillouin zone as θ_1 runs from 0 to 2π . The rising dispersion indicates a positive chirality of the underlying Weyl point. Right: Similar samples are prepared for values of θ_2 . The dispersion is also ascending here, indicating a second positively charged Weyl node.

5.2 Topological exploration

The purpose of this section is to reframe and analyse the non-orientable Weyl semimetals described in Ref. [25] in terms of the algebraic topology language from Chapter 4. This approach has the advantage of being coordinate-free, and as such it provides a more fundamental understanding of the system's topological properties. We obtain a direct description of how the Nielsen–Ninomiya theorem is modified

into the \mathbb{Z}_2 charge cancellation condition in Equation (5.5). We also obtain a more complete picture of the different invariants associated with such a system, and are able to distinguish which are related to the topological insulator phase, and which relate to the introduction of Weyl nodes. Along the way, we develop a formalism for studying semimetal topology in a more general non-orientable setting. To the knowledge of the author, the insights contained in the remainder of this chapter are novel.

5.2.1 Preliminary clarifications

As a motivation for the proposed coordinate-free description, we begin by elucidating some minor points of confusion present in Ref. [25].

First of all, there is a relatively strong emphasis on the two “orientation-reversing planes” at $k_y = \pm\pi$ and $k_y = 0$. For example, it is stated that relative chirality can be defined unambiguously on fundamental domains that avoid these planes. This is true on a technical level, but it creates the impression that the orientation reversal occurs locally at the boundary of the fundamental domain, raising questions about the nature of Weyl points existing on these planes.

In reality, orientation reversal is a global feature. We are free to reparametrise the fundamental domain in a way that includes the planes $k_y = \pm\pi$ and $k_y = 0$, and the notion of relative chirality may change as a result; this is illustrated in Figure 5.8. For any given set of distinct Weyl points obeying the symmetry, it is possible in

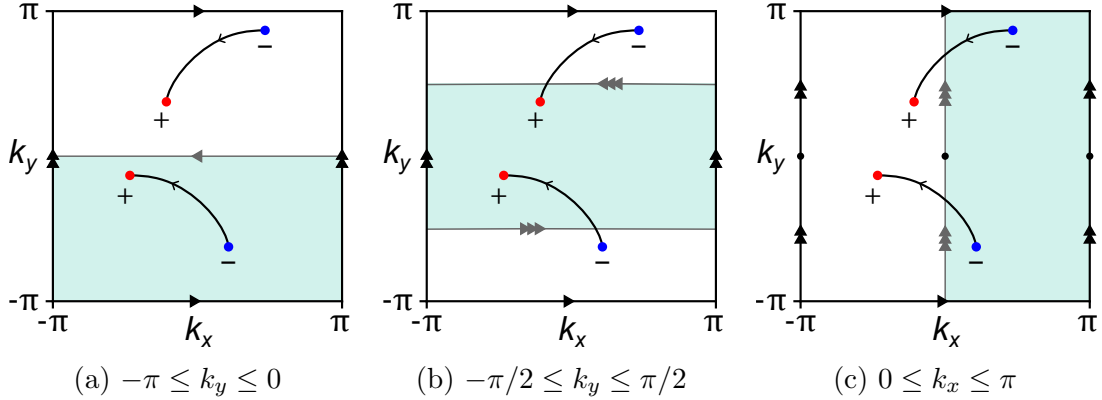


Figure 5.8: Top view of the 3D Brillouin torus (or 2D surface torus) for a given Weyl semimetal state obeying the glide symmetry in Equation (5.4), with Weyl points and oriented Dirac strings (Fermi arcs) drawn in. Different parametrisations of the fundamental domain are shaded in teal: (a) the domain outlined in Ref. [25]; (b) the same domain shifted in the k_y direction; (c) a domain spanning the k_y direction. Each of these domains is homeomorphic to $K^2 \times S^1$ (K^2) under the boundary identifications shown. Note that both the absolute and relative chirality of the two Weyl nodes in the fundamental domain change under these alternative parametrisations.

principle to achieve any relative chirality by reparametrising the fundamental domain. It should be noted that there do exist two planes that are of special significance,

namely the so-called *glide planes* at $k_x = 0$ and $k_x = \pm\pi$; these planes are (taken as a whole) invariant under the symmetry, and as such they cannot be excluded completely from any given parametrisation.

A similar point of confusion arises in explaining how the usual relation between Nielsen–Ninomiya and the Poincaré–Hopf theorem for vector fields breaks down. On the regular Brillouin torus, the factor $\mathbf{h}(\mathbf{k})$ in the Bloch Hamiltonian can be considered a continuous vector field tangent to the torus. The Poincaré–Hopf theorem then tells us that the zeroes of such vector fields must have topological indices (corresponding to Weyl point chiralities) adding up to zero.

In the supplement to Ref. [25], the failure of Poincaré–Hopf is attributed to a discontinuity of the vector field at the planes $k_y = \pm\pi$ and $k_y = 0$; see Figure 5.9. However, this mischaracterises the situation somewhat; in reality, $\mathbf{h}(\mathbf{k})$ cannot be

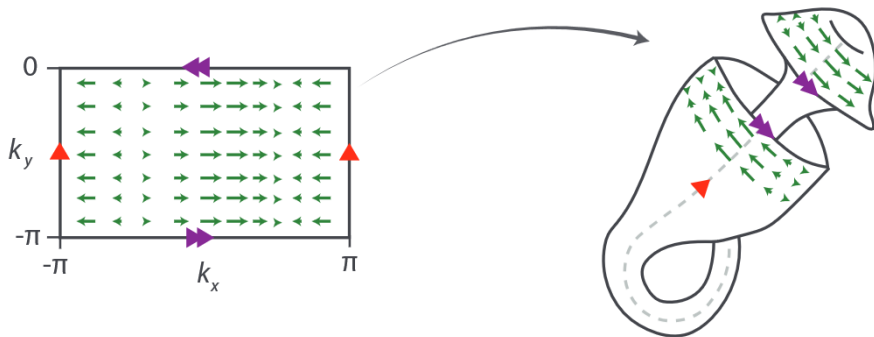


Figure 5.9: Figure from the supplement to Ref. [25]. The k_x component of an example $\mathbf{h}(\mathbf{k})$ is mapped onto a K^2 slice of the fundamental domain and then “bent into shape” to demonstrate discontinuity.

considered a well defined tangent vector field to $K^2 \times S^1$ to begin with. This is illustrated in Figure 5.10: two vectors which point away from each other in the fundamental domain may instead point towards each other after applying the glide symmetry. As such, \mathbf{h} should be thought of as a more abstract map $K^2 \times S^1 \rightarrow \mathbb{R}^3$ rather than a tangent vector field. To be precise, \mathbf{h} is a section of the trivial \mathbb{R}^3 -bundle over $K^2 \times S^1$, not of its tangent bundle.⁵ The resulting mod 2 charge cancellation is not necessarily a sign that Poincaré–Hopf has failed, but rather that we are operating outside its realm of applicability. In fact, instead of rendering the theorem broken in some way, it may be more constructive to reason the other way around. The argument goes as follows: Poincaré–Hopf usually holds because one can always locally induce a canonical orientation on the tangent bundle from an orientation on the manifold itself. However, in the case of a map $K^2 \times S^1 \rightarrow \mathbb{R}^3$, one has an orientable \mathbb{R}^3 -bundle over a non-orientable base manifold. This means that the orientation of the bundle becomes fundamentally disconnected from that of the manifold, and a relative orientation between the two must be chosen arbitrarily and—since the base manifold does not admit a global orientation—locally. The mod 2 charge cancellation then tells us how Poincaré–Hopf needs to be modified to accommodate

⁵In the usual case of the torus, these descriptions are equivalent: \mathbb{T}^3 is parallelisable, i.e. $T\mathbb{T}^3 \cong \mathbb{T}^3 \times \mathbb{R}^3$. This is what allows Poincaré–Hopf to apply naturally.

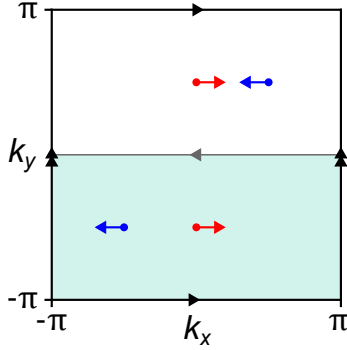


Figure 5.10: Example values of $\mathbf{h}(\mathbf{k})$, interpreted as a vector field on the glide symmetric Brillouin torus. Similar colours indicate that the points are related by glide symmetry. Between two such symmetry related points \mathbf{k} and \mathbf{k}' , the relation $\mathbf{h}(\mathbf{k}) = \mathbf{h}(\mathbf{k}')$ implies that the direction of the vector is not reversed by the glide reflection. As a result, the vector field behaves differently between the two halves of \mathbb{T}^3 , and so it is ill defined as a vector field on $K^2 \times S^1$.

this arbitrary orientation: in some sense it gives rise to a “generalised” or “modified” Poincaré–Hopf theorem. Note that choosing between different fundamental domains on the torus (in the way outlined in Figure 5.8) is precisely a way of inducing such a relative orientation between $K^2 \times S^1$ and its \mathbb{R}^3 -bundle; we will see this idea play out in more detail once we derive the mod 2 charge cancellation from more fundamental cohomology arguments.

It is worth emphasizing that this modification of Poincaré–Hopf is a general feature of non-orientable manifolds, not one that is specific to the model Hamiltonian. Smooth tangent vector fields can in fact be defined on $K^2 \times S^1$, but a Hamiltonian cannot be associated to them in a canonical way. Such a construction usually requires using gamma matrices that “twist along” with the tangent bundle of the manifold instead of the regular vector of Pauli matrices, but these gamma matrices cannot be defined consistently on a non-orientable manifold.⁶ As a result, the notion of a tangent vector field loses some of its utility in studying the topological properties of a non-orientable system. Instead, any topological analysis must be performed in terms of more fundamental algebraic topology tools, such as the homology and cohomology relied on in this work.

A final point that merits clarification is the inclusion of a second glide symmetry. The supplement to Ref. [25] discusses imposing Equation (5.4) together with a similar symmetry along the glide plane $k_y = 0$:

$$H(k_x, k_y, k_z) = H(k_x + \pi, -k_y, k_z). \quad (5.6)$$

It is claimed that this double symmetry subdivides the 3-torus into four copies of a different non-orientable manifold $\mathbb{RP}^2 \times S^1$. Here \mathbb{RP}^2 is the real projective plane,

⁶The proper construction is that of a Clifford algebra bundle over the tangent bundle, see Section 4.2 of Ref. [7]. This construction relies on the existence of a so-called *spin^c structure* (essentially a basis of spinors) on the base manifold, but non-orientable manifolds do not admit such a structure on their tangent bundle.

i.e. the space of all lines through the origin in \mathbb{R}^3 ; it can be obtained by identifying all antipodal points on a 2-sphere. In this case, $\mathbb{RP}^2 \times S^1$ is obtained by imposing anti-periodic boundary conditions in both the k_x and k_y directions on a quarter of the Brillouin torus. However, this direct identification with $\mathbb{RP}^2 \times S^1$ cannot be made as straightforwardly as in the case of a single glide symmetry. As discussed in our review of Refs. [102] and [24] in Section 5.1, the combination of two perpendicular glide symmetries in two dimensions does not have a free action, leading to the fixed points shown in Figure 5.3.

The situation is analogous in three dimensions: the four lines at the momenta $\mathbf{k} = (\pm\pi/2, \pm\pi/2, k_z)$ are fixed under application of both glide symmetries at once. As a result, a Weyl point existing on one of these lines must have an even chirality, and it only has one symmetric partner in the 3-torus rather than the three one would expect from four identical copies of $\mathbb{RP}^2 \times S^1$.⁷ Such Weyl points are physically fine-tuned and are expected to split into pairs under perturbations. Nevertheless, additional symmetries may exist which force Weyl points to exist on these lines, in which case the exceptional behaviour becomes key to the description [111]. Moreover, the reduction to a fundamental domain is predicated on a free group action in the main text of Ref. [25]. As such, analysis of a purely $\mathbb{RP}^2 \times S^1$ Brillouin zone cannot a priori be expected to provide the correct topological classification for this double glide symmetry. Indeed, similar to the case of time reversal in Section 4.2.4, a proper classification scheme should involve equivariant cohomology on the torus, bearing in mind the topological role of the high-symmetry points.⁸ This becomes manifestly clear from the existence of a topological invariant at these high-symmetry points [24, 102]. This full analysis is somewhat beyond the scope of the present text, and in what follows we will restrict our attention to the case of a single glide symmetry.

5.2.2 Classification scheme

There are two main conceptual challenges that present themselves in attempting to apply consistent cohomology and homology frameworks to non-orientable systems, and in particular in developing a physical intuition for them. First of all, the analogy between second cohomology classes and differential two-forms such as the Berry curvature \mathcal{F} breaks down in this case, and a statement like Equation (4.4) can no longer be taken to hold directly. This is because differential forms like \mathcal{F} cannot be integrated over non-orientable manifolds, and the associated (de Rham) cohomology

⁷One can also argue that this must be the case topologically: if a manifold M has an n -sheeted cover \tilde{M} , then the Euler characteristics of both spaces must be related by $\chi(\tilde{M}) = n\chi(M)$. Reducing the system down to two dimensions, we find $\chi(\mathbb{T}^2) = 0$ and $\chi(\mathbb{RP}^2) = 1$, so that the former cannot cover the latter. Instead, the only possible covering space for \mathbb{RP}^2 is the double cover $S^2 \rightarrow \mathbb{RP}^2$, since $\chi(S^2) = 2$. Technically speaking, this means the fundamental domain needs to be described as an *orbifold* rather than a manifold, i.e. a space that encodes data about orbits of a group action. For example, the Euler characteristic of \mathbb{RP}^2 is zero as an orbifold.

⁸The mathematical description may be further complicated by the fact that the high-symmetry points are fixed only by a proper subgroup of the symmetry group. Beyond equivariant cohomology, the natural setting may be to treat $\mathbb{RP}^2 \times S^1$ as an *orbifold* rather than a manifold, i.e. a space that encodes data about orbits of a group action. For example, the Euler characteristic of \mathbb{RP}^2 is zero as an orbifold. These spaces can be analysed using the highly specialised tool of *orbifold cohomology*; see for example Ref. [112] for an application to crystallographic symmetries.

group is actually real-valued—as discussed in Section 2.2.2, it cannot readily encode the \mathbb{Z}_2 invariants induced by changes in orientation. As an example, suppose we are trying to find an invariant for the 2D Klein bottle insulator obeying Equation (5.1). Integrating a Berry curvature on K^2 directly is not well defined, while integrating over the entire Brillouin torus always yields zero: the integration is over two oppositely oriented areas. The correct \mathbb{Z}_2 invariant can be interpreted as integration with different signs on both halves of the torus, bearing in mind that the result is only gauge invariant mod 2. In order to capture this behaviour generally, we need to move to the richer but more abstract integer-valued cohomology laid out in Section 2.2.

The second obstacle is that Poincaré duality is altered in this context. In Section 4.2, this form of duality was used to identify the familiar cohomology invariants with homology invariants, in the form of non-trivial oriented loops and Dirac strings. In a non-orientable system, this identification cannot be made directly; in this case, either the homology or the cohomology must be twisted by the introduction of a local coefficient system $\tilde{\mathbb{Z}}$ [32, 113]; this is the same notion of local coefficients discussed in Section 4.2.4. Such a coefficient system compensates for the twist in orientation by tracking sign changes across the manifold.⁹ Introducing local coefficients on an n -manifold M gives rise to the twisted homology and cohomology groups $H_k(M; \tilde{\mathbb{Z}})$ and $H^k(M; \tilde{\mathbb{Z}})$. Poincaré duality then takes the following forms [32, Theorem 3H.6]:

$$H_k(M; \tilde{\mathbb{Z}}) \cong H^{n-k}(M), \quad (5.7)$$

$$H^k(M; \tilde{\mathbb{Z}}) \cong H_{n-k}(M). \quad (5.8)$$

That is, twisting either one of the homology or cohomology restores Poincaré duality; if the homology is twisted, ordinary cohomology must be used and vice versa. When M is orientable, the local coefficients become trivial and the original form of Poincaré duality is recovered from both relations.¹⁰

Given the fact that Poincaré duality can be restored by twisting either the homology or the cohomology group, the correct classification of a non-orientable physical system hinges on this choice of twist. Fortunately, there is a straightforward way to decide between the two in the case of a Weyl semimetal with an orientation-reversing \mathbb{Z}_2 symmetry. In this situation, Poincaré duality is necessary in order to relate the chirality of Weyl points (which are cohomology invariants) to the orientation of their corresponding Dirac strings (which are the dual homology invariants). Under the orientation-reversing symmetry, Poincaré duality breaking manifests itself in the fact that the Weyl point chiralities are naturally reversed, while the orientation of Dirac strings is unchanged. This is illustrated schematically in Figure 5.11. The decision of which group must be twisted can thus be made by noting how the chirality of Weyl points (outside of high-symmetry points) relates to that of their symmetric

⁹Technically speaking, we are specifically describing local coefficients *in the orientation sheaf*, i.e. twisted along the local orientation of the manifold. In general, the coefficients can be twisted along any \mathbb{Z} -bundle over the manifold, and in particular the trivial bundle gives normal coefficients in \mathbb{Z} .

¹⁰The twist in the orientation sheaf is necessary to have Poincaré duality in the non-orientable case, but technically it need not be the only twist in the coefficients; additional twists may be added to both the homology and cohomology simultaneously without breaking the duality again [114, § 5.2.2.], and this is also true in the orientable case. This appears to be superfluous in this case, but it may become useful when dealing with non-trivial projections onto the surface.

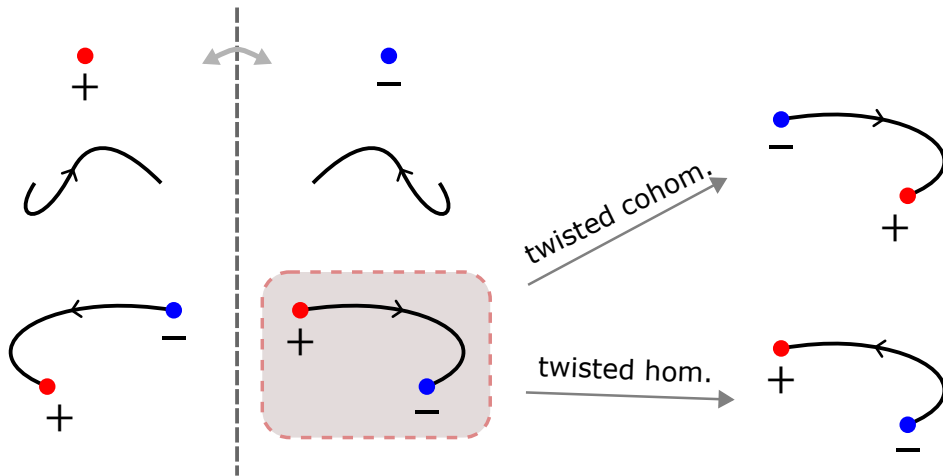


Figure 5.11: On the top left, the action of an orientation-reversing symmetry (represented by the dashed mirror axis) is shown on a Weyl point [of which the chirality is an invariant in $H^2(M \setminus W)$] and a Dirac string [representing an invariant in $H_1(M, W)$]. The Weyl point has its chirality reversed, since the Chern number is a pseudoscalar. On the other hand, the Dirac string is mirrored but maintains its internal orientation (i.e. its image is also oriented away from the “hook” at the end). As a result, when the symmetry acts on a set of two Weyl points connected by a Dirac string, the resulting structure (shown in the shaded area) has a Dirac string of which the orientation is inconsistent with the chirality of the Weyl points, pointing from positive to negative—this is a result of Poincaré duality breaking. This problem can be resolved in one of two ways: either the cohomology is twisted into $H^2(M \setminus W; \tilde{\mathbb{Z}})$ to undo the chirality reversal of the Weyl points, or the homology is twisted into $H_1(M, W; \mathbb{Z})$ to reverse the Dirac string’s orientation. Poincaré duality is restored in both cases; the correct approach depends on the physical setup.

partners in the full Brillouin torus. To be precise, the presence of same-chirality pairs indicates that the (cohomological) Chern number is not reversed as expected, and the cohomology must be twisted. Meanwhile, pairs with opposite chiralities indicate that the cohomology behaves naturally, and the homology (i.e. the Dirac string orientations) must be twisted to follow suit.

There is a natural physical constraint on this relative chirality between symmetry-related Weyl points: if the orientation-reversing symmetry is unitary, then Weyl points have symmetric partners of opposite chiralities. This can be seen as follows: in the case of a unitary symmetry relating $\mathbf{k} \leftrightarrow \mathbf{k}'$, the Hamiltonian obeys

$$U\mathcal{H}(\mathbf{k})U^{-1} = \mathcal{H}(\mathbf{k}').$$

If $|\psi(\mathbf{k})\rangle$ is an eigenstate of $\mathcal{H}(\mathbf{k})$, it follows that $|\psi(\mathbf{k}')\rangle := U|\psi(\mathbf{k})\rangle$ is an eigenstate

of $\mathcal{H}(\mathbf{k}')$, and so the Berry connection transforms as

$$\begin{aligned}\mathcal{A}(\mathbf{k}) &= i \langle \psi(\mathbf{k}) | \partial_{\mathbf{k}} \psi(\mathbf{k}) \rangle \cdot d\mathbf{k} \\ &= i \langle \psi(\mathbf{k}') | UU^{-1} | \partial_{\mathbf{k}} \psi(\mathbf{k}') \rangle \cdot d\mathbf{k} \quad \xrightarrow{UU^{-1} = \mathbb{1}, \partial_{\mathbf{k}} f \cdot d\mathbf{k} = \partial_{\mathbf{k}'} f \cdot d\mathbf{k}'} \\ &= i \langle \psi(\mathbf{k}') | \partial_{\mathbf{k}'} \psi(\mathbf{k}') \rangle \cdot d\mathbf{k}' \\ &= \mathcal{A}(\mathbf{k}').\end{aligned}$$

Since the Berry connection one-form is left invariant, so is the Berry curvature two-form. A final minus sign is then induced by the change of orientation when integrating this two-form, so that the Chern number (Weyl point chirality) changes sign under unitary orientation-reversing symmetries. This is exactly what is implied when the Chern number is called a pseudoscalar. Referring back to Figure 5.11, we conclude that twisted homology (and its dual ordinary cohomology) must be used to obtain the correct invariants under unitary symmetries.

The anti-unitary case is more difficult to pin down: the relative chirality of symmetric pairs of Weyl points may be either equal or opposite under anti-unitary symmetry [115]. This is where the line of reasoning set out in Figure 5.11 is most useful. As an example, we apply this argument to the time-reversal invariant Weyl semimetal from Section 4.2.4. This system is not usually thought of in terms of non-orientability, but the time reversal symmetry acts in an orientation-reversing way: an odd number (i.e. all three) of momentum directions are inverted, leading to a change of parity. Figure 5.12(a) illustrates that the effective Brillouin zone¹¹ is indeed non-orientable. As discussed before, the pairs of Weyl points at opposite momenta (related by $\mathbf{k} \leftrightarrow -\mathbf{k}$) always have the same chirality in this system; see Figure 5.12(b). Again, these same-chirality pairs are an indication that the Chern numbers of Weyl points do not transform as expected, and so the cohomology must be twisted. It follows that the homology should be left untwisted; this can also be seen directly from the Dirac strings in Figure 5.12(b), whose orientation is directly related by the symmetry (i.e. the arrows run in relative directions respecting $\mathbf{k} \leftrightarrow -\mathbf{k}$). This description in terms of twisted cohomology and ordinary homology agrees exactly with the one given in Section 4.2.4, which was derived from more abstract vector bundle classification arguments in Ref. [85]. In this particular case, direct calculation of the (co)homology groups on the effective Brillouin zone is complicated by the existence of high-symmetry points (i.e. the action of the symmetry is not free), which is why the authors of Ref. [85] use equivariant (co)homology on the full torus.

Returning to the case of a momentum-space glide symmetry, we can infer from Figure 5.8(a) that the situation is different here. The unitary nature of the symmetry [which is explicitly seen in Equation (5.4)] ensures that every Weyl point in the fundamental domain is related by symmetry to an oppositely charged point in the other half of the torus, while the orientation of Dirac strings is reversed under the symmetry. It follows that the classification of topological phases should rely on twisted *homology*, and equivalently, ordinary cohomology. Since there are no high-symmetry points in this case, there is no need to compute equivariant (co)homology

¹¹Recall from Section 4.2.4 that the effective Brillouin zone indicates the quotient $\mathbb{T}^3/\mathbb{Z}_2$ of the Brillouin torus by the symmetry group. In this case, the presence of high-symmetry points prevents this region from being a proper Brillouin zone, which is why we do not call it a fundamental domain.

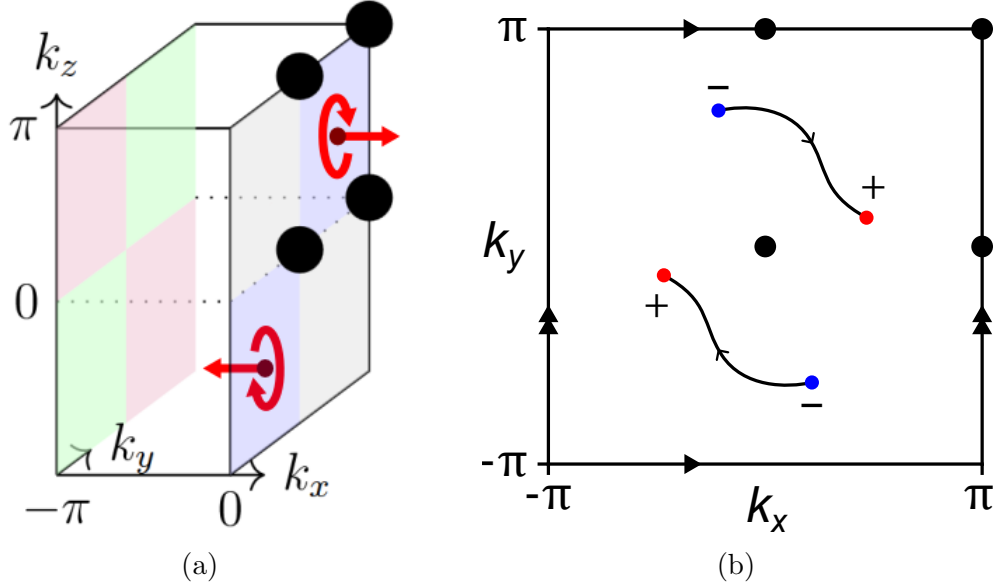


Figure 5.12: (a) Figure adapted from Ref. [85]. The effective Brillouin zone under time reversal symmetry is half of \mathbb{T}^3 , with additional identifications of the coloured areas as $k \sim -k$. The resulting space is non-orientable: a “test particle” with a given helicity (obeying a left hand rule) is shown travelling out through the top right of the $k_x = 0$ boundary, and reappearing at its bottom left with the opposite helicity (obeying a right hand rule). (b) Top view of the Brillouin torus for a time-reversal invariant Weyl semimetal. The two (red) positively charged Weyl points are interrelated by the $\mathbf{k} \leftrightarrow -\mathbf{k}$ symmetry, as are the (blue) negatively charged points. These pairs of same-chirality points indicate a twist in the cohomology. On the other hand, the orientation of Dirac strings respects the symmetry, indicating ordinary (“untwisted”) homology.

groups, and we may instead rely on ordinary cohomology and twisted homology on the fundamental domain $K^2 \times S^1$.¹²

The choice of ordinary cohomology can be corroborated in two important ways. Firstly, the use of ordinary second cohomology classes indicates that we are classifying complex line bundles over the fundamental domain. An important insight from K-theory tells us that this is equivalent to classifying equivariant line bundles over the full torus [117, Proposition 2.1].¹³ That is, we are classifying states that respect the symmetry directly. Secondly, the \mathbb{Z}_2 invariant found in Ref. [25] on K^2 -like slices of constant k_z is recovered using ordinary cohomology, related to the fact that $H^2(K^2) \cong \mathbb{Z}_2$. Twisted cohomology would give a $H^2(K^2; \mathbb{Z}) \cong \mathbb{Z}$ invariant on these slices.

All in all, we find that the correct classification of semimetal phases in this system is given by the following Mayer–Vietoris exact sequence of cohomology groups on

¹² Formally speaking, equivariant cohomology of a space M with a free action of the group G is equivalent to ordinary cohomology on the quotient space M/G [116, Corollary 9.6].

¹³This is related to footnote 12 in the sense that K-theory is a *generalised cohomology* theory.

$M := K^2 \times S^1$:

$$0 \rightarrow \underbrace{H^2(M)}_{\text{Insulator}} \rightarrow \underbrace{H^2(M \setminus W)}_{\text{Semimetal}} \rightarrow \bigoplus_{w \in W} H^2(S_w^2) \xrightarrow{\Sigma} H^3(M) \rightarrow 0, \quad (5.9)$$

where as before, W is the set of Weyl points on M and S_w^2 is a small 2-sphere surrounding the Weyl point $w \in W$. Equivalently, the classification may be given in terms of the following dual *twisted* homology sequence:

$$0 \rightarrow \underbrace{H_1(M; \tilde{\mathbb{Z}})}_{\text{Twisted Dirac loops}} \rightarrow \underbrace{H_1(M, W; \tilde{\mathbb{Z}})}_{\text{Twisted Dirac strings}} \xrightarrow{\delta} H_0(W; \tilde{\mathbb{Z}}) \xrightarrow{\Sigma} H_0(M; \tilde{\mathbb{Z}}) \rightarrow 0, \quad (5.10)$$

where we refer to the Dirac loops and Dirac strings as twisted to emphasise the non-trivial action of the symmetry on their orientation. The concept of a twisted Dirac string on $K^2 \times S^1$ can be difficult to intuit, leading to Dirac strings that appear to change orientation at orientation-reversing boundaries of the fundamental domain in a setup like Figure 5.8(c). As such, they are more readily understood as equivariant (i.e. symmetry-related) pairs of Dirac strings on the full torus \mathbb{T}^3 , of which the orientation is reversed under the symmetry.

In what follows, we will provide explicit computations of these sequences and discuss the associated invariants.

5.2.3 Computation of invariants on $K^2 \times S^1$

The use of ordinary cohomology groups in the Mayer–Vietoris sequence (5.9) means that calculations are relatively straightforward, and standard techniques such as cellular homology can be applied [32, §2.2]. Using these methods, we calculate the sequence to be

$$0 \rightarrow \mathbb{Z} \oplus \mathbb{Z}_2 \xrightarrow{\alpha} \mathbb{Z} \oplus \mathbb{Z}_2 \oplus \mathbb{Z}^k \xrightarrow{\beta} \mathbb{Z}^k \xrightarrow{\Sigma} \mathbb{Z}_2 \rightarrow 0, \quad (5.11)$$

where $k = |W|$ is the number of Weyl points. Given that the twisted homology sequence (5.10) is related to the Mayer–Vietoris sequence by Poincaré duality, it features the exact same groups in the same order; the difference is only in the interpretation.

For comparison, we recall here the semimetal Mayer–Vietoris sequence on \mathbb{T}^3 from Section 4.2.3:

$$0 \rightarrow \mathbb{Z}^3 \rightarrow \mathbb{Z}^3 \oplus \mathbb{Z}^{k-1} \xrightarrow{\beta} \mathbb{Z}^k \xrightarrow{\Sigma} \mathbb{Z} \rightarrow 0. \quad (5.12)$$

Some relevant differences between these two sequences are highlighted below.

Insulating phases

The first difference between the Mayer–Vietoris sequences on \mathbb{T}^3 and $K^2 \times S^1$ lies in the insulating topology of the system, in the absence of any Weyl points. Whereas the 3D Chern insulator on the plain torus features a Chern vector in $H^2(\mathbb{T}^3) \cong \mathbb{Z}^3$, this group is reduced to $H^2(K^2 \times S^1) \cong \mathbb{Z} \oplus \mathbb{Z}_2$ under the action of the glide symmetry.

As a result, the $K^2 \times S^1$ insulator is not classified by three Chern numbers $C_{x,y,z} \in \mathbb{Z}$, but by a \mathbb{Z} invariant ν_x and a \mathbb{Z}_2 invariant ν_z —the reasoning behind our choice of symbols will become apparent shortly.

The reduction to two invariants can be most readily understood from the twisted homology point of view. On \mathbb{T}^3 , the three generators of $H_1(\mathbb{T}^3) \cong \mathbb{Z}^3$ are represented by oriented Dirac loops $\ell_{x,y,z}$ that wind around the 3-torus once in each respective coordinate direction. Under glide symmetry, each of these loops obtains a symmetric partner $\ell'_{x,y,z}$ with a reversed internal orientation—this is due to the twist in the homology. Taken together with the original loop, $\ell_{x,y,z} + \ell'_{x,y,z}$ is equivalent to a twisted Dirac loop $\tilde{\ell}_{x,y,z}$ on $K^2 \times S^1$, representing an invariant in $H_1(K^2 \times S^1; \widetilde{\mathbb{Z}})$. The reduction to $\mathbb{Z} \oplus \mathbb{Z}_2$ is then caused by specific degeneracies in these twisted Dirac strings: $\tilde{\ell}_x$ generates the full \mathbb{Z} invariant ν_x , $\tilde{\ell}_y$ turns out to be trivial, and $\tilde{\ell}_z$ generates the \mathbb{Z}_2 invariant ν_z . This is illustrated in more detail in Figure 5.13.

The invariant $\nu_z \in \mathbb{Z}_2$ corresponds precisely to the \mathbb{Z}_2 invariant on K^2 slices described in Ref. [25], and stems from the 2D Klein bottle insulator in Ref. [21]. It may be calculated on any K^2 slice using Equations (5.2) and (5.3).

The \mathbb{Z} invariant ν_x appears to be novel; as discussed under Figure 5.13(a), it manifests as an even Chern number $C_x = 2\nu_x \in 2\mathbb{Z}$ on the full Brillouin torus, relating to the fact that the torus contains two copies of $K^2 \times S^1$. This suggests one way of calculating this invariant in practice: it may be obtained from \mathbb{T}^3 as

$$\nu_x = \frac{1}{2}C_x = \frac{1}{4\pi} \int_{\mathbb{T}_{yz}^2} \mathcal{F}, \quad (5.13)$$

where \mathbb{T}_{yz}^2 is any slice of \mathbb{T}^3 running in the yz -direction. This calculation does not generally respect the glide symmetry, since such a \mathbb{T}_{yz}^2 is not invariant outside of the glide planes at $k_x = 0$ and $k_x = \pm\pi$. Still, it results in the correct invariant in the insulating case: by regular Poincaré duality on the full torus, the integral over \mathbb{T}_{yz}^2 counts the number of ℓ_x -like Dirac loops, and the generator $\tilde{\ell}_x$ features precisely two such loops on the torus.¹⁴ We will return to the case with Weyl points when we study the full group of semimetal invariants.

Mod 2 charge cancellation

A second feature that stands out is the appearance of a \mathbb{Z}_2 group on the far right side of the exact sequence in Equation (5.11). It is worth mentioning that this is a general feature of ordinary cohomology on non-orientable manifolds: the rightmost group is the top cohomology group of the fundamental Brillouin zone, and any non-orientable n -manifold M has $H^n(M) \cong \mathbb{Z}_2$.

Recall from Section 4.2.3 that the map Σ in Equation (5.12) can be interpreted as a sum over all Weyl point charges on \mathbb{T}^3 . The Nielsen–Ninomiya charge cancellation theorem on the torus then arises from the fact that $\Sigma \circ \beta = 0$; that is, a semimetal structure $a \in \mathbb{Z}^3 \oplus \mathbb{Z}^{k-1}$ must always feature a charge configuration $\beta(a) \in \mathbb{Z}^k$ such that the charges sum to $\Sigma(\beta(a)) = 0 \in \mathbb{Z}$.

¹⁴A Dirac loop may in principle also contain y and z components, but these do not affect this integral. From a homology perspective, such loops may be decomposed into their basic $\ell_{x,y,z}$ components because the first homology group is Abelian.

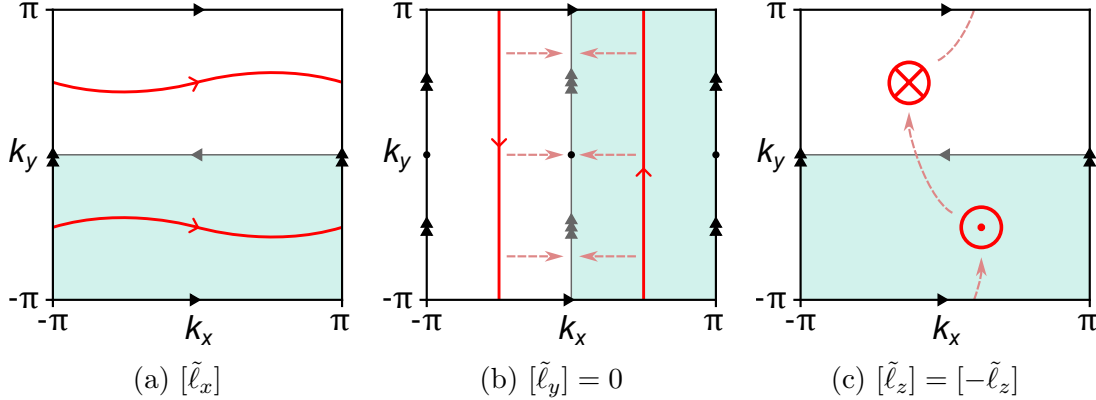


Figure 5.13: Top view of \mathbb{T}^3 . Each graphic shows one of the three basic Dirac loops $\ell_{x,y,z}$ [representing the generators of $H_1(\mathbb{T}^3)$] sitting inside a fundamental domain (shaded teal). Each loop is doubled by the action of the symmetry, into what can be considered a twisted Dirac loop $\tilde{\ell}_{x,y,z}$ [representing an invariant in $H_1(K^2 \times S^1; \mathbb{Z})$] shown in red. (a) In the case of ℓ_x , the orientation reversal cancels out the $k_x \mapsto -k_x$ parity change from the glide symmetry, and the resulting twisted Dirac string $\tilde{\ell}_x$ has a consistent orientation. It follows that the associated invariant $\nu_x \in \mathbb{Z}$ induces an even Chern number $C_x = 2\nu_x \in 2\mathbb{Z}$ on the full torus. (b) The alternative fundamental domain from Figure 5.8(c) paints a clearer picture for ℓ_y . The loop is mirrored along the glide plane $k_x = 0$ and has its orientation reversed. The resulting twisted Dirac string $\tilde{\ell}_y$ is trivial: as indicated by the dashed arrows, the two copies can be moved together while maintaining glide symmetry, and they cancel out when they meet on the glide plane. As a result, there is no invariant ν_y . (c) The Dirac loop ℓ_z running in the positive z direction (“out of the page”) in the fundamental domain is doubled to a second loop running in the negative z direction (“into the page”). In this case, the two loops cannot be brought together while respecting the symmetry, but they can be interchanged by moving them along the dashed arrows. It follows that the resulting twisted Dirac string $\tilde{\ell}_z$ is equivalent to its own inverse $-\tilde{\ell}_z$, meaning it generates a \mathbb{Z}_2 invariant ν_z .

The situation is somewhat more subtle on $K^2 \times S^1$: the \mathbb{Z}^k group $H^2\left(\bigcup_{i=1}^k S_{w_i}^2\right)$ and its dual $H_0(W; \mathbb{Z})$ no longer have a direct interpretation in terms of Weyl point charges, since both the absolute and relative chiralities of these points are ill defined (see Figure 5.8). That is, the spheres S_{w_i} no longer have a canonical orientation descending from the ambient manifold.¹⁵ Instead, $H^2\left(\bigcup_{i=1}^k S_{w_i}^2\right)$ must be interpreted as the group of charges χ_i given a choice of orientation at each Weyl point w_i . This choice of orientation is exactly what is induced by choosing a specific fundamental domain: the changes of (absolute and relative) chirality in Figure 5.8 correspond to

¹⁵This is closely related to our observation in Section 5.2.1 that Poincaré–Hopf fails to apply because the trivial \mathbb{R}^3 -bundle over $K^2 \times S^1$ does not have a canonical orientation with respect to its base manifold.

a change of basis of this \mathbb{Z}^k . Nevertheless, the map Σ can still be interpreted as a sum over these charges, precisely because it maps into \mathbb{Z}_2 :¹⁶ to be exact, the map

$$\Sigma : \mathbb{Z}^k \rightarrow \mathbb{Z}_2, \quad (\chi_1, \dots, \chi_k) \mapsto \sum_{i=1}^k \chi_i \mod 2 \quad (5.14)$$

is invariant under change of orientation at each w_i because

$$\chi_i \equiv -\chi_i \mod 2.$$

It follows that the tail end of the sequence (5.11) can be interpreted unambiguously in terms of \mathbb{Z}_2 charge cancellation: regardless of the parametrisation of the fundamental domain, the charges belonging to a semimetal (i.e. mapped into \mathbb{Z}^k by β) must sum to $0 \in \mathbb{Z}_2$. This is the same charge cancellation condition presented in Equation (5.5).

Importantly, the exactness of Equation (5.11) also implies the converse statement by $\text{im}(\beta) = \ker(\Sigma)$: for a given set of Weyl points $W \subset K^2 \times S^1$, any configuration of charges with an even total [i.e. an element of $\ker(\Sigma)$] must be realised in some set of semimetal invariants [i.e. be an element of $\text{im}(\beta)$]. In the homology picture, this means there must exist configurations of twisted Dirac strings in $H_1(M, W; \tilde{\mathbb{Z}})$ realising any given set of charges adding to $0 \in \mathbb{Z}_2$.

One must be careful in interpreting this mod 2 charge cancellation in terms of a potentially non-zero total chirality. The \mathbb{Z}_2 group in the Mayer–Vietoris sequence tells us that total charge is fundamentally a \mathbb{Z}_2 invariant, and the semimetal topology fixes it to zero. Given any particular parametrisation of the fundamental domain, there may appear to be a net non-zero chirality on the Brillouin zone $K^2 \times S^1$, but this is not a topological invariant: for example, in Figure 5.8, the net chirality of a single topological state may be found to be 0, 2 or -2 depending on the parametrisation. In other words, the total chirality is ill defined as an integer in \mathbb{Z} , while the *parity* of the total charge is well defined and topologically invariant.

The appearance of non-zero total chirality is in close analogy to the concept of ghost fields in quantum field theory. There, apparent quantum fields may arise when fixing unphysical local gauge degrees of freedom. These ghost fields can usually be removed by a suitable change of gauge, and in any case they never appear in external physical observables. Similarly, the choice of orientation for a Weyl point on $K^2 \times S^1$ is an unphysical local degree of freedom, and one can usually choose these orientations (i.e. fix a fundamental domain) in a way that results in a total chirality of zero. In particular, this implies that one cannot readily assign physical meaning (e.g. in terms of an uncancelled chiral anomaly) to the net chirality appearing in a certain fundamental domain.

This can also be understood in field theory terms: as discussed in Section 5.2.1, a Hamiltonian cannot be defined on $K^2 \times S^1$ in terms of the tangent vector field, since it lacks a spinor basis (i.e. choice of gamma/Pauli matrices). Instead, any effective field theory on $K^2 \times S^1$ must rely on a choice of coordinates, and will not be invariant under change of coordinates in general. In such a theory, a net chiral anomaly will not generally represent a physically observable phenomenon. In other words, while the

¹⁶Indeed, the group $H^3(K^2 \times S^1) \cong \mathbb{Z}_2$ is closely linked to the orientation of $K^2 \times S^1$; in technical terms, we say that $K^2 \times S^1$ is \mathbb{Z}_2 -orientable but not \mathbb{Z} -orientable [32, §3.3].

Nielsen–Ninomiya theorem is altered mathematically on $K^2 \times S^1$, its core physical implications of chiral anomaly cancellation cannot necessarily be circumvented. In this respect, the description in terms of the full Brillouin torus \mathbb{T}^3 with a glide symmetry may be more useful phenomenologically, where Nielsen–Ninomiya is more straightforwardly preserved and each Weyl point has a canonical orientation.

Semimetal invariants

Finally, central to the sequence in Equation (5.11) is the group of semimetal invariants,

$$H^2(K^2 \times S^1 \setminus W) \cong H_1(K^2 \times S^1, W; \tilde{\mathbb{Z}}) \cong \mathbb{Z} \oplus \mathbb{Z}_2 \oplus \mathbb{Z}^k. \quad (5.15)$$

Much like the $\mathbb{Z}^3 \oplus \mathbb{Z}^{k-1}$ in the case of \mathbb{T}^3 , this group does not admit a canonical basis of invariants. Rather, the exactness of Equation (5.11) around this group provides information about the structure of the different semimetallic phases. The argument is similar to that given for the torus at the end of Section 4.2.3. In what follows, we make reference to the maps α , β and Σ as defined in Equation (5.11). Given a charge configuration $c \in \mathbb{Z}^k$ in the image of the map β (i.e. any c with an even total charge), the pre-image must obey

$$\beta^{-1}(c) \cong \beta^{-1}(0) =: \ker(\beta),$$

since β is a homomorphism.¹⁷ By exactness, this can be calculated as $\ker(\beta) \cong \text{im}(\alpha) \cong \mathbb{Z} \oplus \mathbb{Z}_2$. That is, for each $c \in \text{im}(\beta)$ there is a $\mathbb{Z} \oplus \mathbb{Z}_2$ of possible semimetal invariants (or equivalently, twisted Dirac string configurations) in its pre-image, differing from each other by the bulk invariants $\nu_x \in \mathbb{Z}$ and $\nu_z \in \mathbb{Z}_2$.

There is a subtle difference from the argument on the torus: on \mathbb{T}^3 , \mathbb{Z} charge cancellation ensures that the valid charge configurations exist in

$$\text{im}(\beta) = \ker(\Sigma) = \bigoplus_{w \in W} H^2(S_w^2) / H^3(\mathbb{T}^3) \cong \mathbb{Z}^k / \mathbb{Z} \cong \mathbb{Z}^{k-1},$$

explaining the \mathbb{Z}^{k-1} summand in the semimetal group. This \mathbb{Z}^{k-1} cannot be given a basis in terms of the k different Weyl point charges on the semimetal, and it must be interpreted more abstractly as the set of valid charge configurations. On $K^2 \times S^1$, the \mathbb{Z}_2 charge cancellation implies that

$$\text{im}(\beta) = \ker(\Sigma) \cong \mathbb{Z}^k / \mathbb{Z}_2 \cong \mathbb{Z}^k,$$

and this is the \mathbb{Z}^k which appears in the semimetal group in Equation (5.15). Just as on the torus, we should be careful not to interpret this \mathbb{Z}^k directly in terms of the charges of the k Weyl points. Even though it contains k factors of \mathbb{Z} , not all possible combinations of charges are contained in this subgroup: after all, charge configurations with an odd total are not in the kernel of Σ . Instead, it should be considered an index 2 subgroup of the charge configurations, containing only those with an even total.

¹⁷As before, this is a consequence of the first isomorphism theorem.

Physically, the \mathbb{Z}^k summand in the semimetal group implies that a system with a single Weyl point ($k = 1$) on $K^2 \times S^1$ may already feature semimetal topology, unlike the torus where a minimum of two points are needed. The single Weyl point must have even charge by \mathbb{Z}_2 charge cancellation; an example of such a system is featured in the supplement to Ref. [25] and reproduced in Figure 5.14.

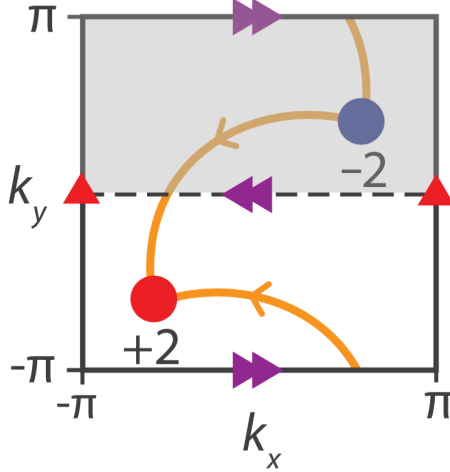


Figure 5.14: Figure adapted from the supplement to Ref. [25]. Interpreted here as a top view of the Brillouin torus. The upper half lies outside of the fundamental domain and has been greyed out to emphasise that there is only one Weyl point on $K^2 \times S^1$. Both Dirac strings are oriented towards the positively charged point on the torus; from the perspective of the fundamental domain, there is a single twisted Dirac string, which reverses orientation as it crosses $k_y = 0$ and is connected to the same Weyl point at both ends. Thinking more abstractly in terms of $K^2 \times S^1$, such an orientation-reversing boundary cannot be pointed out, and a consistent orientation cannot be assigned to this Dirac string—this is exactly what necessitates the use of twisted homology.

Finally, we have seen in Section 4.2.2 that the Chern number on a 2D slice of T^3 changes by $q \in \mathbb{Z}$ as the slice is passed over a Weyl point of charge q . We might expect this to be problematic in the non-orientable case, given that the fundamental Brillouin zone is (anti-)periodic and the total charge need not add up to zero. This is resolved in two different ways for the two invariants ν_x and ν_z . The latter is saved by being a \mathbb{Z}_2 invariant, restoring the periodicity over an even total charge—as was also observed in Ref. [25].

The \mathbb{Z} invariant ν_x requires us to define the integration more carefully: as noted before, the integration in Equation (5.13) does not respect the symmetry, and it may not yield the right invariant when Weyl points are introduced. This is illustrated in Figure 5.15(a). Instead, it becomes necessary to integrate over a symmetry-invariant surface S which is continuously deformable to a \mathbb{T}_{yz}^2 , such as that shown in Figure 5.15(b). This is similar in spirit to the T -invariant surfaces used to calculate invariants in the time-reversal symmetric case [85]. In principle, only the half of the surface $S_{1/2}$ which intersects the fundamental domain at $k_y \leq 0$ needs to be integrated over; this half surface can be considered a compact surface subspace of

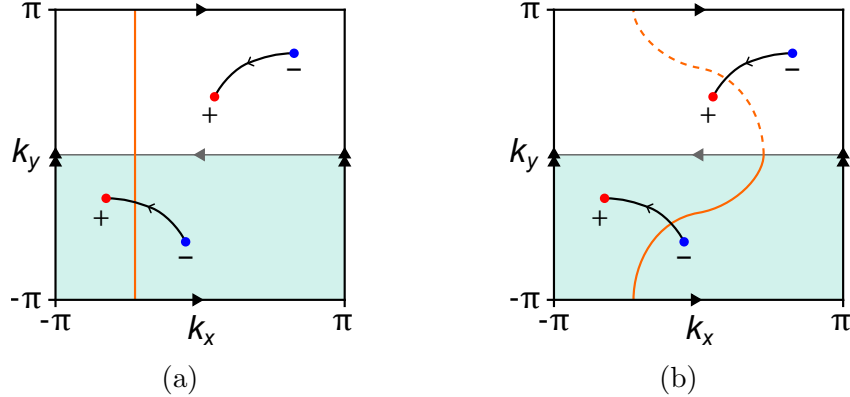


Figure 5.15: (a) In the presence of Weyl points, a given \mathbb{T}_{yz}^2 (orange) may only intersect a single Dirac string, leading to a non-integer value of $1/2$ from Equation (5.13). (b) Integration over an invariant surface always yields a well defined ν_x outside of Weyl points, since it intersects the twisted Dirac strings in a consistent manner. The dashed half of the surface is redundant, since both halves yield the same integral. The pictured setup yields $\nu_x = 1$.

$K^2 \times S^1$. The calculation then takes the form

$$\nu_x = \frac{1}{2\pi} \int_{S_{1/2}} \mathcal{F}. \quad (5.16)$$

The question of periodicity is now resolved by the fact that the surface S cannot be moved across the entire Brillouin torus without breaking the symmetry: any such surface can be deformed equivariantly into exactly one of the glide planes at $k_x = 0$ and $k_x = \pm\pi$, but one cannot be deformed into the other. For example, if we start with S at the $k_x = 0$ plane and perturb a small section of S continuously in the positive x direction, then another section must be moved in the negative x direction at the same time to maintain glide symmetry. By continuity, it follows that S must still intersect $k_x = 0$ somewhere.¹⁸ As such, there is no deformation that can completely remove S from the $k_x = 0$ plane, and in particular it cannot be taken fully to the glide plane at $k_x = \pm\pi$. An analogous argument holds the other way around.¹⁹

As a final remark, we note that the only \mathbb{Z}_2 factor in the semimetal group in Equation (5.15) stems directly from the underlying insulating topology; any Weyl points that are added only introduce additional \mathbb{Z} factors. As such, it is the opinion of the author that no intrinsic \mathbb{Z}_2 charge should be assigned to Weyl points, as is

¹⁸The argument can be formalised using the mean-value theorem if we take the momenta to live in \mathbb{R}^3 rather than identifying equivalent momenta into a torus.

¹⁹By the same logic, we can generally infer which of the two glide planes S deforms to by studying these intersections: for example, the surface in Figure 5.15(b) does not intersect the plane at $k_x = \pm\pi$, and so it must deform to $k_x = 0$. In general, we can count the number of times S intersects with $k_x = 0$ in the range $-\pi < k_y \leq 0$ (at any k_z); an odd number of intersections [such as the single crossing in the fundamental domain in Figure 5.15(b)] indicates that the surface deforms to $k_x = 0$.

done in Ref. [25].²⁰ Instead, the \mathbb{Z}_2 invariant on gapped K^2 -like slices should be taken to be directly influenced by the \mathbb{Z} charge on Weyl points. To be precise, if such a slice with invariant ν_z is moved over a Weyl point of charge C in the k_z direction, the new \mathbb{Z}_2 invariant is

$$\nu'_z = \nu_z + C \mod 2,$$

requiring no \mathbb{Z}_2 charge on the Weyl point. This is also the position taken with respect to time-reversal invariant Weyl semimetals in Ref. [85].

5.2.4 Classification of K^2 surface states

We now turn our attention to the classification of surface states (i.e. Fermi arcs) on the two-dimensional surfaces of the $K^2 \times S^1$ system obeying the glide symmetry in Equation (5.4). As mentioned in Section 4.2.2, Fermi arcs may be considered projections of the topological Dirac strings existing in the bulk. The same line of reasoning holds in this case: the twisted Dirac strings may be projected onto a surface Brillouin zone to obtain oriented Fermi arcs.

Of the three coordinate directions that we may project along, the k_z direction is the most tractable, since there is no additional symmetry in this direction beyond the usual lattice translation. As such projecting along k_z amounts to integrating out the periodic S^1 direction in $K^2 \times S^1$, to obtain a Klein bottle shaped K^2 surface Brillouin zone spanning the k_x and k_y directions. This is the surface that is discussed extensively and probed experimentally in Ref. [25].

Because the projection π_z along the k_z direction loses no essential information about the symmetries of the system, it has a clear interpretation in terms of homology groups. Recall that, given a set of Weyl points $W \subset K^2 \times S^1$, a configuration of twisted Dirac strings c defines a twisted relative homology class:

$$[c] \in H_1(K^2 \times S^1, W; \tilde{\mathbb{Z}}).$$

The projection π_z acts on c to give a configuration of Fermi arcs $\pi_z(c)$. Taking into account the twist in orientation, $\pi_z(c)$ can be taken to represent a homology class:

$$[\pi_z(c)] \in H_1(K^2, W'; \tilde{\mathbb{Z}}),$$

where $W' := \pi_z(W)$ denotes the projection of the Weyl points on the surface. Formally, there is a surjective map

$$(\pi_z)_*: H_1(K^2 \times S^1, W; \tilde{\mathbb{Z}}) \rightarrow H_1(K^2, W'; \tilde{\mathbb{Z}}), \quad [c] \mapsto [\pi_z(c)]$$

called the *pushforward* of π_z on homology classes. The surjectivity of this map ensures that all possible configurations of Fermi arcs in $H_1(K^2, W'; \tilde{\mathbb{Z}})$ are physically realisable, meaning this group provides a full classification of Fermi arcs on the K^2 surface.

²⁰Explicit calculations are provided for this \mathbb{Z}_2 charge in Ref. [25], but these rely on integration over K^2 -like tubes spanning the fundamental domain in the k_y direction. As a result, these invariants are an expression of the global topology of $K^2 \times S^1 \setminus W$, not the local topology around a Weyl point.

The other groups in the twisted homology semimetal sequence in Equation (5.10) may also be mapped by similar pushforwards of π_z , and in particular this operation preserves the nature of the maps featured in the sequence. This then gives rise to a similar exact sequence of twisted homology groups on the K^2 surface:

$$0 \rightarrow \underbrace{H_1(K^2; \tilde{\mathbb{Z}})}_{\text{Twisted Fermi loops}} \rightarrow \underbrace{H_1(K^2, W'; \tilde{\mathbb{Z}})}_{\text{Twisted Fermi arcs}} \xrightarrow{\partial} H_0(W'; \tilde{\mathbb{Z}}) \rightarrow H_0(K^2; \tilde{\mathbb{Z}}) \rightarrow 0. \quad (5.17)$$

We can then make use of twisted Poincaré duality in order to turn this into a more computable Mayer–Vietoris sequence of ordinary cohomology groups:²¹

$$\dots \xrightarrow{0} H^1(K^2) \rightarrow H^1(K^2 \setminus W') \rightarrow \bigoplus_{w' \in W'} H^1(S^1_{w'}) \rightarrow H^2(K^2) \rightarrow 0. \quad (5.18)$$

Note that compared to the bulk sequence in Equation (5.9), this sequence classifies topological states in terms of first cohomology groups H^1 rather than second cohomology groups H^2 . This is indicative of the fact that the chiralities of surface states are given by winding numbers of the Berry connection 1-form \mathcal{A} , rather than Chern numbers obtained from the Berry curvature 2-form \mathcal{F} .

Just as in the bulk, the Mayer–Vietoris sequence in Equation (5.18) can be computed using standard tools such as cellular homology. The resulting explicit sequence is as follows:

$$\dots \xrightarrow{0} \mathbb{Z} \rightarrow \mathbb{Z} \oplus \mathbb{Z}^k \rightarrow \mathbb{Z}^k \xrightarrow{\Sigma} \mathbb{Z}_2 \rightarrow 0. \quad (5.19)$$

This sequence is very similar in nature and interpretation to the bulk sequence in Equation (5.11). The only essential difference is that the insulating \mathbb{Z}_2 invariant ν_z has disappeared as a result of the projection in the k_z direction.

In particular, this sequence features a similar mod 2 charge cancellation property to the one seen in the bulk, implying that the winding numbers of the Berry connection \mathcal{A} around each projected Weyl node must add to a total of $0 \in \mathbb{Z}_2$. Just as in the bulk, there is an important caveat regarding the physical interpretation of this: the sign of the winding number at a Weyl node w depends on a choice of orientation for the circle S^1_w that surrounds it. Just as in the bulk, this choice of orientation can be induced from a chosen fundamental domain, and this may lead to different relative chiralities between projected Weyl points.

As an example, the experimentally observed dispersion in Figure 5.7 depends on the choice of fundamental domain. That is, one can extend the K^2 surface Brillouin zone to the full \mathbb{T}^2 in this figure by including momenta with $0 < k_2 \leq \pi$, and then choose a different fundamental domain to change the relative chirality. This is illustrated in Figure 5.16.

The surface states obtained by truncating the system in the x and y directions cannot quite as readily be expressed in terms of a similar surface Mayer–Vietoris sequence. For example, an straightforward projection in the k_x direction loses

²¹One needs to be a bit careful here in the sense that there is no longer a zero group to the left of the proper Mayer–Vietoris sequence, owing to the appearance of $H^0(S^1_{w'}) \cong \mathbb{Z}$ terms instead of the $H^1(S^2_w) = 0$ in the bulk sequence. However, this does not change the interpretation of the sequence at all: the leftmost map into $H^1(K^2)$ is still trivial, since the circles $S^1_{w'}$ are contractible inside K^2 .

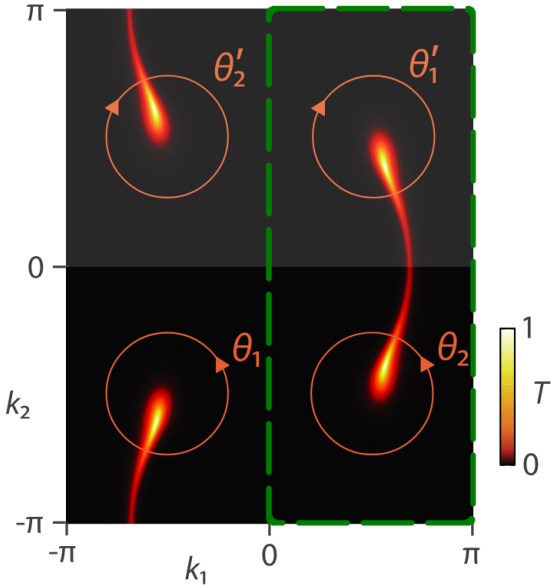


Figure 5.16: Figure adapted from Ref. [25], depicting the same system as Figure 5.7. The lower black region is the K^2 -like fundamental domain used by the authors. The upper grey region is obtained by mirroring this domain horizontally, completing the surface Brillouin torus. The two circular integration domains parametrised by θ_1 and θ_2 are mirrored to oppositely oriented circles parametrised by θ'_1 and θ'_2 respectively. Because the system respects this symmetry, the clockwise dispersion along θ'_1 and θ'_2 will look identical to the counter-clockwise dispersion along θ_1 and θ_2 . In other words, if the contour around the upper points is taken along the more conventional counter-clockwise direction, the dispersion is mirrored with respect to the lower points (i.e. it descends from the conduction band to the valence band instead of ascending as it does in Figure 5.7). As a result, the fundamental domain chosen as in Figure 5.8(c) (here outlined in green) features two oppositely charged points with conventional dispersion characteristics.

information about the $k_x \leftrightarrow -k_x$ action of the glide symmetry. One result of this is that the surface Brillouin zone is orientable in this direction—it has the topology of the 2-torus \mathbb{T}^2 , and the glide symmetry reduces to a half lattice translation. Still, this symmetry appears to reverse the orientation of the surface Weyl points and their associated Fermi arcs; see Figure 5.17. This seemingly tells us that the coefficients of both the homology and cohomology should be twisted. This seems to disagree with Equations (5.7) and (5.8), but in reality, those relations specifically hold for twists which respect the orientation of the manifold. In general, simultaneous twists in the homology and cohomology are permitted, as long as the *relative* twist between the coefficients respects the orientation. In this case, then, the correct description might be constructed in terms of twisted homology and cohomology, where the coefficients are twisted in such a way that they change sign under the $k_y \mapsto k_y + \pi$ symmetry. There may even be a canonical way to induce this twist from the projection π_x , based on the action of the glide reflection in the k_x direction. These ideas certainly deserve

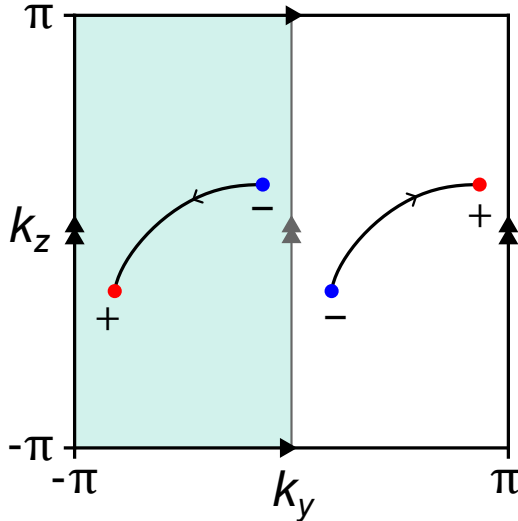


Figure 5.17: Surface Brillouin zone in the yz direction, with the projected fundamental domain indicated in teal and a possible configuration of Fermi arcs. This surface features an orientation-preserving translation symmetry in the k_y direction. This symmetry still reverses both the chirality of the projected Weyl points (which is not expected under an orientation-preserving symmetry) and the orientation of the Fermi arc, appearing to indicate that both the cohomology and the homology must be twisted.

further thought; for one thing, it becomes necessary to calculate the twisted groups without resorting to an ordinary Poincaré dual group.²²

The projection in the k_y direction comes with challenges of its own, owing to the fact that the half lattice translation is projected out. The resulting surface of the Brillouin torus is mirror symmetric, and from its perspective, it appears as though the surface could host a single pair of Weyl points connected by a symmetric Fermi arc. In reality, such a configuration would require double charges to be physical, resulting from the projection of a configuration such as that in Figure 5.14. Tentatively, this may indicate that the pushforward of the projection π_y simply is not surjective, and attempting to calculate (co)homology groups on this surface may fundamentally “overclassify” the possible topology.

5.3 Other non-orientable Brillouin zones

As we have reviewed in Sections 5.1 and 5.2.1, the fact that a single glide symmetry has a free action on the Brillouin torus does not guarantee that a combination of multiple glide symmetries also acts freely. This raises the question of whether there are any other momentum space symmetries besides the single glide reflection which give rise to a proper non-orientable fundamental Brillouin zone without high-

²²The application of different twisted groups to topological matter has been studied in some detail in the more abstract setting of K-theory [35, 36]. The cohomology setting that we are working in is essentially a more tractable specialised version of this.

symmetry points. Indeed, there are several in three dimensions; the aim of this section is to provide a complete overview of these symmetries.

We also provide a cohomological classification of the insulator and Weyl semimetal invariants existing on these three-dimensional non-orientable Brillouin zones, under the assumption that the symmetry has its usual unitary action on the Hamiltonian. That is, we present the invariants obtained from ordinary cohomology and twisted homology, similar to the $K^2 \times S^1$ case discussed in the previous section. All explicitly calculated cohomology groups in this section are obtained using cellular homology.

In order to ensure completeness, the classification of fundamental Brillouin zones must rely on the theory of *space groups*, which fully categorise the possible symmetry operations on periodic systems [118]. We begin by briefly reviewing the two-dimensional case.

In two dimensions, the situation is quite manageable: there are only 17 space groups in total, which are referred to as the *wallpaper groups*. Of these, 13 are *symmorphic*, meaning their generators are symmetries with fixed points (i.e. mirror reflections and rotations in 2D). As a result, these groups cannot have a non-trivial free action. The four remaining non-symmorphic groups include at least one glide symmetry. Of these, it turns out that only the wallpaper group pg featuring a single glide symmetry has a free action [119]. This is precisely the symmetry that gives rise to the Klein bottle shaped fundamental domain first discussed in Ref. [21]. We conclude that the Klein bottle K^2 is the only non-orientable two-dimensional manifold that can act as the Brillouin zone of a crystalline system.²³ We have already studied its topology as a surface Brillouin zone in Equation (5.19).

In three dimensions, there are a total of 230 space groups. Among these, 73 are *symmorphic* (i.e. generated by point-fixing symmetries such as inversion, reflection and rotation) and the remaining 157 are *non-symmorphic*, featuring at least one glide reflection or screw rotation—the latter being a combination of a rotation and fractional lattice translation. Of the non-symmorphic space groups, a total of 12 have a group action that is free [119, Eq. (110)]. Of these, eight are generated only by screw rotations, which are orientation-preserving—just like ordinary rotations. This means they give rise to orientable fundamental domains, which can be classified using ordinary homology and cohomology. Nevertheless, these orientable Brillouin zones may feature non-orientable subspaces giving rise to \mathbb{Z}_2 invariants. Furthermore, we will discuss instances in which screw rotations are combined with glide reflections. For these reasons, we briefly expand on one of these space groups here before moving on to the four orientation-reversing cases.

The simplest space group featuring a screw rotation is $P2_1$, which is a \mathbb{Z}_2 group generated by a combined half turn and half lattice translation. For example, taking the screw axis to be the y axis, a Hamiltonian with momentum space $P2_1$ symmetry obeys the relation

$$\mathcal{H}(k_x, k_y, k_z) = U\mathcal{H}(-k_x, k_y + \pi, -k_z)U^{-1}.$$

The fundamental domain of this symmetry can be taken to be the half torus with $-\pi \leq k_y \leq 0$ just as for the glide symmetry, but the boundary identifications are

²³Again, this related to the fact that it is the only non-orientable manifold with a vanishing Euler characteristic.

different: instead of mirroring the $k_y = -\pi$ face before identifying it with the $k_y = 0$ face, it must be rotated by a half turn. The resulting Brillouin zone topology is dubbed a “half-turn space” in Ref. [23], which probes a system with such a momentum space symmetry experimentally.²⁴ The explicit semimetal Mayer–Vietoris sequence of this space is as follows:

$$0 \rightarrow \mathbb{Z} \oplus \mathbb{Z}_2^2 \rightarrow \mathbb{Z} \oplus \mathbb{Z}_2^2 \oplus \mathbb{Z}^{k-1} \rightarrow \mathbb{Z}^k \rightarrow \mathbb{Z} \rightarrow 0. \quad (5.20)$$

That is, the insulating invariants on the half-turn space are classified by $\mathbb{Z} \oplus \mathbb{Z}_2^2$, and Weyl points in the fundamental domain obey the regular Nielsen–Ninomiya theorem. The two \mathbb{Z}_2 invariants stem from K^2 -like subspaces of the half-turn space, one of which is illustrated in Figure 5.18.

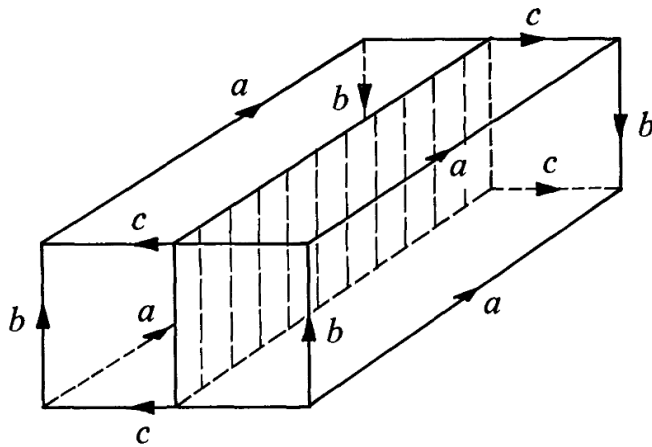


Figure 5.18: Figure from Ref. [120]. The half-turn space (called a “twisted cube” in that work) is shown with a two-dimensional subspace, which has the topology of a Klein bottle.

Free orientation-reversing space groups in 3D

We now turn our attention to the four remaining space groups with free actions, all of which give rise to a non-orientable Brillouin zone. The first and simplest of these is Pc , and it is precisely the \mathbb{Z}_2 group generated by a single glide symmetry that we have discussed at length in this chapter. Its semimetal Mayer–Vietoris sequence is given in Equation (5.11), and we refer to Section 5.2.3 for its interpretation.

The remaining three groups— Cc , $Pca2_1$ and $Pna2_1$ —all combine a glide symmetry with another operation to form a $\mathbb{Z}_2 \oplus \mathbb{Z}_2$ group. As such, the fundamental Brillouin zones that they induce cover exactly one fourth of the full Brillouin torus T^3 . Just as in the $K^2 \times S^1$ case, these fundamental domains can be parametrised in any number of ways, without changing the topology of the underlying manifolds. As such, we will remain agnostic about the choice of fundamental domain here, and simply provide the relevant Mayer–Vietoris sequences. The reader wishing to develop

²⁴To be precise, the full space group obeyed by the system in Ref. [23] is $P2_1/c$, which also features a glide symmetry; the action of this space group is not free.

an intuition for the ways in which these spaces can be partitioned is referred to a space group atlas such as Ref. [121].

The group Cc combines a glide symmetry and a diagonal half-lattice translation, in such a way that the Hamiltonian obeys the following relations under momentum space Cc symmetry (up to coordinate permutations):

$$\begin{aligned}\mathcal{H}(k_x, k_y, k_z) &= U\mathcal{H}(k_x, -k_y, k_z + \pi)U^{-1}, \\ \mathcal{H}(k_x, k_y, k_z) &= U\mathcal{H}(k_x + \pi, k_y + \pi, k_z)U^{-1}.\end{aligned}$$

The Mayer–Vietoris sequence associated with the non-orientable Brillouin zone under this symmetry is as follows:

$$0 \rightarrow \mathbb{Z} \oplus \mathbb{Z}_2^2 \rightarrow \mathbb{Z} \oplus \mathbb{Z}_2^2 \oplus \mathbb{Z}^k \rightarrow \mathbb{Z}^k \rightarrow \mathbb{Z}_2 \rightarrow 0. \quad (5.21)$$

Again, this is the sequence in terms of ordinary cohomology or twisted homology.

The space group $Pca2_1$ features a glide reflection and a screw rotation. The momentum space $Pca2_1$ symmetry acts on the Hamiltonian in the following way:

$$\begin{aligned}\mathcal{H}(k_x, k_y, k_z) &= U\mathcal{H}(k_x + \pi, -k_y, k_z)U^{-1}, \\ \mathcal{H}(k_x, k_y, k_z) &= U\mathcal{H}(-k_x, -k_y, k_z + \pi)U^{-1}.\end{aligned}$$

The associated Mayer–Vietoris sequence of ordinary cohomology groups is then

$$0 \rightarrow \mathbb{Z}_2^2 \rightarrow \mathbb{Z}_2^2 \oplus \mathbb{Z}^k \rightarrow \mathbb{Z}^k \rightarrow \mathbb{Z}_2 \rightarrow 0. \quad (5.22)$$

Finally, the group $Pna2_1$ is generated by similar operations as $Pca2_1$, but with the glide reflection plane offset from $k_y = 0$ by $\pi/2$; the resulting action on the Hamiltonian is

$$\begin{aligned}\mathcal{H}(k_x, k_y, k_z) &= U\mathcal{H}(k_x + \pi, \pi - k_y, k_z)U^{-1}, \\ \mathcal{H}(k_x, k_y, k_z) &= U\mathcal{H}(-k_x, -k_y, k_z + \pi)U^{-1}.\end{aligned}$$

The semimetal Mayer–Vietoris sequence in ordinary cohomology is

$$0 \rightarrow \mathbb{Z}_4 \rightarrow \mathbb{Z}_4 \oplus \mathbb{Z}^k \rightarrow \mathbb{Z}^k \rightarrow \mathbb{Z}_2 \rightarrow 0.$$

On the whole, all of these space groups share the same mod 2 charge cancellation seen on $K^2 \times S^1$, as is to be expected from the non-orientability of the underlying Brillouin zone. Incidentally, all three Mayer–Vietoris sequences feature different insulating invariants, which immediately confirms that the underlying manifold is different for each of these space groups (and also different from $K^2 \times S^1$). The insulating topology under $Pna2_1$ symmetry is especially interesting, being classified by a single \mathbb{Z}_4 invariant. Such invariants are fairly uncommon; for example, they do not appear in the tenfold way classification in Table 3.1. The derivation of an explicit expression and physical interpretation for this invariant is somewhat beyond the scope of this work, but a twisted homology argument similar to that provided in Figure 5.13 may provide intuitive insight.

We would be remiss not to mention Ref. [49] again in this context. Similar cellular decompositions are used in that work to arrive at a comprehensive K-theory classification of invariants related to space group symmetries. In comparison, the present

calculations in terms of Mayer–Vietoris sequences may offer more specific insights into the structure of the semimetal invariants, and the dual twisted homology picture may prove invaluable in interpretation. Another nuance is that our classification stems from a two band model, whereas that in Ref. [49] is a many band scheme; in principle, this makes for a more general description, but it may also give rise to invariants that are not reflected in the transport properties of the material.

5.4 Inversion-symmetric semimetal topology

In this final section, we turn our attention to a very important class of Weyl semimetals: those obeying inversion symmetry. As discussed in Section 4.1.3, all Weyl semimetals must break either time-reversal or inversion symmetry. Those with broken time-reversal symmetries are called magnetic Weyl semimetals, and many of their prominent physical realisations are inversion-symmetric [77–79]. Here, we develop an ansatz for the classification of these systems, and demonstrate that the resulting Mayer–Vietoris sequence agrees precisely with their relevant features.

Recall that inversion symmetry acts on the momentum space Hamiltonian as

$$\mathcal{H}(\mathbf{k}) = U\mathcal{H}(-\mathbf{k})U^{-1}.$$

That is, it induces the same symmetry on the Brillouin torus as time-reversal symmetry, but without complex conjugation on the Hamiltonian. The classification of time-reversal symmetric (class AII) Weyl semimetals was completed in Ref. [85], and we have reviewed it in some detail in Section 4.2.4. The description provided there relies on ordinary equivariant homology, and twisted equivariant cohomology relative to the set of time-reversal invariant momenta (TRIM). As previously explained in Section 5.2.2, the use of twisted cohomology can be motivated by noting that the symmetry is orientation-reversing, and that each Weyl node in the Brillouin torus has a symmetric partner which has the same chirality.

The same orientation-reversing symmetry is present under inversion symmetry. However, the lack of complex conjugation ensures that symmetric pairs of Weyl nodes have opposite chiralities instead of equal chiralities in this case. Using the same heuristic from Section 5.2.2, we find that a proper (co)homology classification of inversion-symmetric Weyl semimetals should rely on some form of twisted equivariant homology and ordinary equivariant cohomology. To the knowledge of the author, the use of twisted homology for classification of topological phases is novel to this work, and such a description has not yet been published. Nevertheless, the insulating case has been studied in some detail using different topological tools. Since any semimetal Mayer–Vietoris sequence also includes the insulating invariants of a system, we offer a brief review of these invariants for later comparison. We recommend our construction of the semimetal sequence in Section 5.4.2; the eager reader may choose to skip straight there without loss of continuity.

5.4.1 Existing insulating classifications

The two first and most detailed classifications of three-dimensional inversion-symmetric topological insulators were developed in parallel and published independently:

Ref. [122] in 2011 by Taylor Hughes, Emil Prodan and Andrei Bernevig, and Ref. [123] in 2012 by Ari Turner et al. The works differ somewhat in scope and methodology (the latter is more explicitly topological in nature, making use of homotopy theory on the space of Hamiltonians), but both treat essentially the same invariants and draw all the conclusions relevant to us. As such, we will treat them in tandem. Both works treat systems with an arbitrary number of bands, but for simplicity we will take the liberty of specialising their results to our preferred setting of a traceless two band model, where a single band is always occupied.

Two types of insulating invariants are distinguished under inversion symmetry. The first are three Chern numbers $C_{x,y,z} \in \mathbb{Z}$. These are the same Chern numbers that make up the \mathbb{Z}^3 Chern vector discussed in Section 4.2.1. The second type of invariant is defined at each of the eight high-symmetry points in the Brillouin torus (i.e. the TRIM): since inversion is an order two operation squaring to 1, its eigenvalues on states at the invariant momenta must be ± 1 . At each TRIM κ , the eigenvalue of the occupied state under inversion is a \mathbb{Z}_2 topological invariant $\zeta(\kappa) = \pm 1$. It is shown in Ref. [123] that there are no other types of invariants, so that inversion-symmetric insulators are fully classified by three Chern numbers and eight \mathbb{Z}_2 invariants.

These eleven numbers are not independent; it is shown in both works that they are subject to certain internal relations, illustrated in Figure 5.19. First of all, the

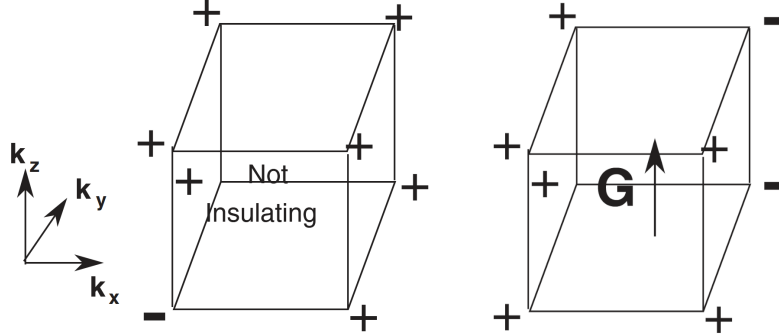


Figure 5.19: Figure from Ref. [123]. Each cube represents one eighth of the Brillouin torus, with the eight TRIM at the corners (e.g. $0 \leq k_{x,y,z} \leq \pi$). Signs indicate the value of ζ at each TRIM. Left: an odd number of negative ζ indicates that the material is not an insulator, and must instead be a Weyl semimetal. Right: Both planes parallel to the k_z axis feature odd numbers of negative ζ , indicating that there is non-zero odd Chern number C_z .

product of all \mathbb{Z}_2 invariants must be positive in an insulator:

$$\prod_{\kappa \in \text{TRIM}} \zeta(\kappa) = 1.$$

In fact, it is argued in Ref. [123] that a value of -1 indicates that the material is a Weyl semimetal: at a TRIM κ , a negative value of $\zeta(\kappa)$ indicates that a Dirac string or loop passes through κ , and a closed inversion-symmetric Dirac loop must always pass through an even number of TRIM.

Secondly, the parity of each Chern number can be related to the product of ζ at four TRIM lying on a plane perpendicular to that Chern number's label: for example, C_z is subject to the relation

$$\prod_{\kappa \in \text{TRIM}_{xy}} \zeta(\kappa) = (-1)^{C_z},$$

where TRIM_{xy} denotes the set of TRIM lying on the xy -plane.

We note that the restrictions on the total product of signs and the three Chern number parities remove four \mathbb{Z}_2 degrees of freedom from three $C_{x,y,z} \in \mathbb{Z}$ and eight $\zeta(\kappa) \in \mathbb{Z}_2$, so that the effective group structure of the insulating invariants ends up being $\mathbb{Z}^3 \oplus \mathbb{Z}_2^4$ instead of $\mathbb{Z}^3 \oplus \mathbb{Z}_2^8$.²⁵ As a result, any semimetal Mayer–Vietoris sequence which we find must account for this $\mathbb{Z}^3 \oplus \mathbb{Z}_2^4$ classification of insulating invariants.

As a final note before we return to our semimetal description, there have been several later papers which also identify certain invariants on inversion-symmetric systems using different methods: Refs. [124, 125] use K-theory (which is closely related to cohomology) and Ref. [126] uses a construction in terms of layered lower dimensional systems. However, all these works give different invariants on 2D and 3D type A systems under inversion, and none of them straightforwardly accounts for both the \mathbb{Z} and \mathbb{Z}_2 invariants present in the two-band model.

The latter observation might be taken to indicate a shortcoming of the two-band model. However, we note that a lot of the physical discussion in Ref. [123] appears to actually attest to its relative usefulness instead. This can be seen as follows: in the full N -band model discussed there, one is left with a $\mathbb{Z}^3 \oplus \mathbb{Z}^8$ of invariants instead of the $\mathbb{Z}^3 \oplus \mathbb{Z}_2^4$ derived above for the two-band model. It is then derived that for any given Chern number in \mathbb{Z}^3 , there are 16 different equivalence classes among the remaining \mathbb{Z}^8 of insulators that have distinguishable transport properties. We note that this is in good agreement with the 16 elements of \mathbb{Z}_2^4 , which appears to speak in favour of the physical effectiveness of the two-band model. In other words, while the full $\mathbb{Z}^3 \oplus \mathbb{Z}^8$ of invariants are indeed all *topologically* distinct, the two-band approximation may more naturally classify phases that are *physically* distinct.

5.4.2 Semimetal classification ansatz

We have already established that a (co)homology description of inversion-symmetric Weyl semimetals must rely on some form of ordinary equivariant cohomology and twisted equivariant homology. However, this does not tell us how the TRIM should be treated; for example, we have no information on whether the equivariant cohomology should be taken relative to the TRIM, excluding the TRIM, or as is without assigning the TRIM special status. In principle it should be possible to infer this information from careful mathematical study of the vector bundle structures that are induced by

²⁵In a description with more occupied bands, the initial set of invariants is larger and this reduction is less dramatic as a result. However, even in this setting it is shown in Ref. [123] that for any given Chern number, there are 16 different classes of insulators with distinguishable transport properties. We note that this corresponds precisely to the 16 elements of \mathbb{Z}_2^4 , which speaks in favour of the effectiveness of the two-band model.

the symmetry. This precisely how the use of twisted equivariant cohomology relative to the TRIM is motivated for the time-reversal symmetric case in Ref. [85], based on extensive mathematical analysis in Refs. [60, 86].

Instead of going to great lengths to perform such analysis, we will take a much more ad hoc approach: we develop an ansatz through some mathematical hand waving, and then show that this yields the correct invariants. The reasoning is as follows: in the cases of a free \mathbb{Z}_2 action that we have seen before, the effective Brillouin zone takes on precisely the topology of the quotient space $\mathbb{T}^3/\mathbb{Z}_2$ —for example, the $K^2 \times S^1$ space that we have studied extensively—and this allows the equivariant (co)homology on \mathbb{T}^3 to be reduced to their more computable ordinary counterparts. Under the present \mathbb{Z}_2 inversion symmetry, the effective Brillouin zone [i.e. the half torus with the identifications pictured in Figure 5.12(a)] has the topology of $\mathbb{T}^3/\mathbb{Z}_2$ “almost everywhere”: only the eight TRIM do not act as the quotient of two separate points in \mathbb{T}^3 . The idea is now that we may still be able to use ordinary (co)homology on the effective Brillouin zone, as long as we can find a consistent and unambiguous way to make sense of the behaviour at the TRIM.

As was the case with the interpretation of the insulating invariants on $K^2 \times S^1$ in Section 5.2.3, the best intuition for this scheme is afforded by the twisted homology picture. In particular, it becomes apparent that the TRIM can act as endpoints of twisted Dirac strings from the perspective of the effective Brillouin zone; this is illustrated in Figure 5.20. In the same way that homology relative to the set of Weyl points W encodes endpoints of Dirac strings, we propose that the correct effective description on the effective Brillouin zone M is that of twisted homology relative to the TRIM. Explicitly, the twisted homology sequence in Equation (5.10) then becomes²⁶

$$\begin{aligned} 0 &\rightarrow H_1(M, \text{TRIM}; \tilde{\mathbb{Z}}) \rightarrow H_1(M, W \cup \text{TRIM}; \tilde{\mathbb{Z}}) \\ &\xrightarrow{\partial} H_0(W; \tilde{\mathbb{Z}}) \rightarrow H_0(M, \text{TRIM}; \tilde{\mathbb{Z}}) \rightarrow 0. \end{aligned}$$

This sequence can be turned into a semimetal Mayer–Vietoris sequence in cohomology, using a twisted version of the modified Poincaré duality in Equation (4.10). This duality tells us that the cohomology must be taken *excluding* the TRIM rather than relative to it:

$$\begin{aligned} 0 &\rightarrow H^2(M \setminus \text{TRIM}) \rightarrow H^2(M \setminus W \cup \text{TRIM}) \\ &\rightarrow \bigoplus_{w \in W} H^2(S_w^2) \rightarrow H^3(M \setminus \text{TRIM}) \rightarrow 0. \end{aligned}$$

This exclusion of the TRIM has an interesting side effect: it ensures that the action of inversion symmetry is completely free on the remaining space, so that the groups in this sequence are fully equivalent to the equivariant cohomology which we are trying to emulate.

²⁶One might expect the third group in this sequence to become either $H_0(W, \text{TRIM}; \tilde{\mathbb{Z}})$ or (given the boundary map before it) $H_0(W \cup \text{TRIM}; \tilde{\mathbb{Z}})$. In fact, both are isomorphic to $H_0(W; \tilde{\mathbb{Z}})$. The former directly so because there are no TRIM in the set W ; the latter is a consequence of the twist in the coefficients, which ensures that $H_0(\text{TRIM}; \tilde{\mathbb{Z}}) = -H_0(\text{TRIM}; \tilde{\mathbb{Z}}) = 0$ under the action of the symmetry.

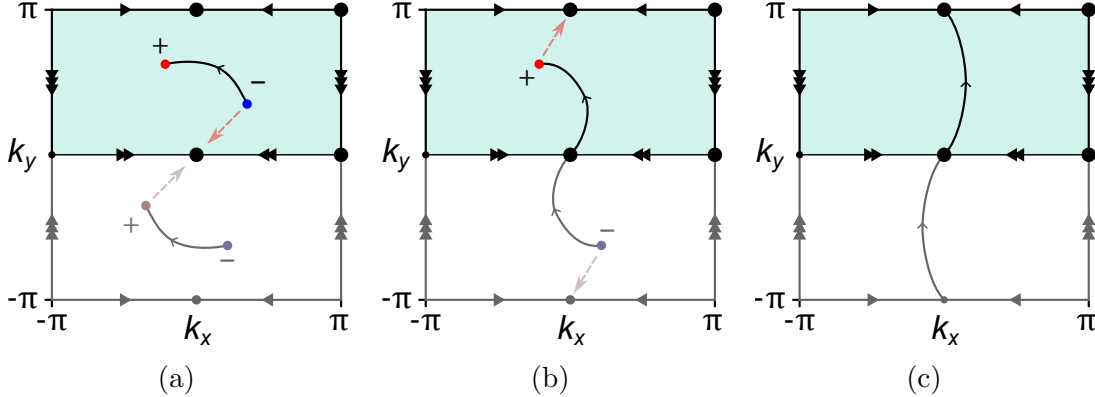


Figure 5.20: A slice of the inversion symmetric Brillouin torus at $k_z = 0$. The (arbitrarily chosen) effective Brillouin zone M is shaded in teal, the four TRIM in this plane are indicated with big dots, and arrows indicate the correct boundary identifications. From left to right, a process of Weyl point annihilation is played out on the torus, while the apparent topology of (twisted) Dirac strings and loops is studied in isolation within M ; the area outside of M is greyed out as a reminder of this. (a) At first, the Dirac string contained within M looks like a “normal” element of $H_1(M, W; \tilde{\mathbb{Z}})$. The negative Weyl point in M and its symmetric partner can be brought together along the orange arrows and annihilated at the TRIM at $\mathbf{k} = 0$. (b) From the perspective of M , the TRIM at $\mathbf{k} = 0$ seems to have absorbed the negative Weyl point, and the Dirac string appears to have a boundary at this TRIM as well as at the remaining Weyl point, meaning it looks like an element of $H_1(M, W \cup \text{TRIM}; \tilde{\mathbb{Z}})$. The remaining two Weyl points on the torus can be brought towards the TRIM at $\mathbf{k} = (0, \pm\pi, 0)$ to annihilate. (c) After this final annihilation, the resulting Dirac loop looks like it runs between two different TRIM inside M , i.e. it looks like an element of $H_1(M, \text{TRIM}; \tilde{\mathbb{Z}})$.

Now that we have reduced our tentative invariant groups to untwisted, non-equivariant cohomology, they may once again be calculated using basic cellular homology. The removal of the TRIM makes this calculation somewhat more cumbersome than the others appearing in this chapter,²⁷ but the conceptual basis is still relatively simple. The explicit semimetal Mayer–Vietoris we obtain in this way is as follows:²⁸

$$0 \rightarrow \mathbb{Z}^3 \oplus \mathbb{Z}_2^4 \rightarrow \mathbb{Z}^3 \oplus \mathbb{Z}_2^4 \oplus \mathbb{Z}^r \rightarrow \mathbb{Z}^r \rightarrow 0 \rightarrow 0, \quad (5.23)$$

where r is the number of Weyl points in the fundamental domain, i.e. there are $2r$

²⁷To be specific, M is no longer closed after removing the TRIM. In order to find a cell structure, one can “grow” the holes in the space while maintaining the correct boundary identifications, until only a set of surfaces remains (in technical terms, one can deformation retract M onto a 2-skeleton). The resulting cell structure is relatively complex, so that extracting its homology takes some work. This work can be facilitated using a computational tool such as the Smith normal form [127].

²⁸The \mathbb{Z}_2^4 components stem from $H_1(M \setminus \text{TRIM}) \cong \mathbb{Z}_2^4$. Interestingly, this is essentially equivalent to the equivariant homology calculation that is performed in Ref. [85] to obtain the four \mathbb{Z}_2 invariants under time reversal: both groups end up classifying T-stable loops on the torus that avoid the TRIM.

Weyl points on the full torus \mathbb{T}^3 .

There are two features of this sequence that stand out immediately. The first is that the insulating invariant group on the left precisely matches the $\mathbb{Z}^3 \oplus \mathbb{Z}_2^4$ derived from the literature in Section 5.4.1. The second is the appearance of a trivial 0 group on the right, as opposed to the \mathbb{Z} or \mathbb{Z}_2 we have seen in other contexts. This implies that there is no notion of charge cancellation at all on the effective Brillouin zone, i.e. the total Weyl point charge contained in it can take on any integer value. This agrees exactly with the existence of states such as the one pictured in Figure 5.20(b), which feature only single Weyl point of charge ± 1 in the effective Brillouin zone; any number of such states can be stacked in order to obtain different total net chiralities.

We should reiterate in this context that the lack of charge cancellation that arises in the mathematical description is not reflective of a physical anomaly of any sort. Rather, not unlike on $K^2 \times S^1$ and other cases we have seen, it results from the fact that each Weyl point comes with its own charge cancelling partner. This is perhaps easier to accept for the system under consideration here; inversion symmetric Weyl semimetals are exceedingly well studied from a physical point of view, and to the knowledge of the author, this non-standard charge cancellation is never a real consideration. One simply studies the behaviour of the material across the entire Brillouin torus, where no such issues arise. Arguably, the situation is somewhat different from $K^2 \times S^1$ because the lack of a free group action implies that the Brillouin zone cannot truly be reduced to a fundamental domain, but for all physical intents and purposes, this changes little about the interpretation of features like charge cancellation. We maintain that even for systems like the single glide symmetry, the most natural setting to study phenomenological features is the complete Brillouin torus.

For completeness, we offer a basis of the insulating invariant group

$$H_1(M, \text{TRIM}; \widetilde{\mathbb{Z}}) \cong \mathbb{Z}^3 \oplus \mathbb{Z}_2^4 \quad (5.24)$$

in terms of twisted Dirac loops, just as we did in Figure 5.13 for the $\mathbb{Z} \oplus \mathbb{Z}_2$ that generates the two invariants on $K^2 \times S^1$. There, we represented the twisted Dirac loops on $K^2 \times S^1$ by glide symmetric sets of loops on the whole torus \mathbb{T}^3 ; we will proceed similarly here by considering inversion symmetric loops on the torus. To this end, we introduce some notation. Taking Figure 5.20(c) as an example, it depicts the loop on the torus that runs through the two TRIM at $\mathbf{k} = 0$ and $\mathbf{k} = (0, \pi, 0)$ in the positive k_y direction. This loop is inversion symmetric, and we denote it by ℓ_{0y0} . Had the loop run up through $\mathbf{k} = (\pi, 0, 0)$ and $\mathbf{k} = (\pi, \pi, 0)$, we would notate $\ell_{\pi y 0}$ instead. Similarly, the loop $\ell_{x0\pi}$ runs through $\mathbf{k} = (0, 0, \pi)$ and $\mathbf{k} = (\pi, 0, \pi)$ in the positive k_x direction, those representing $\ell_{\pi\pi z}$ run through $\mathbf{k} = (\pi, \pi, 0)$ and $\mathbf{k} = (\pi, \pi, \pi)$ with increasing k_z , and so on. There are twelve of these loops in total: four for each coordinate direction.

These loops have a key property that allows them to generate the group in Equation (5.24): while they cannot individually be detached from the TRIM that they run through without breaking inversion symmetry, they can be once they are doubled up; see Figure 5.21(a). In this way it can be shown that $2\ell_{0y0}$ has the same twisted homology class as $2\ell_{\pi y 0}$. This means the classes $[\ell_{0y0}]$ and $[\ell_{\pi y 0}]$ cannot

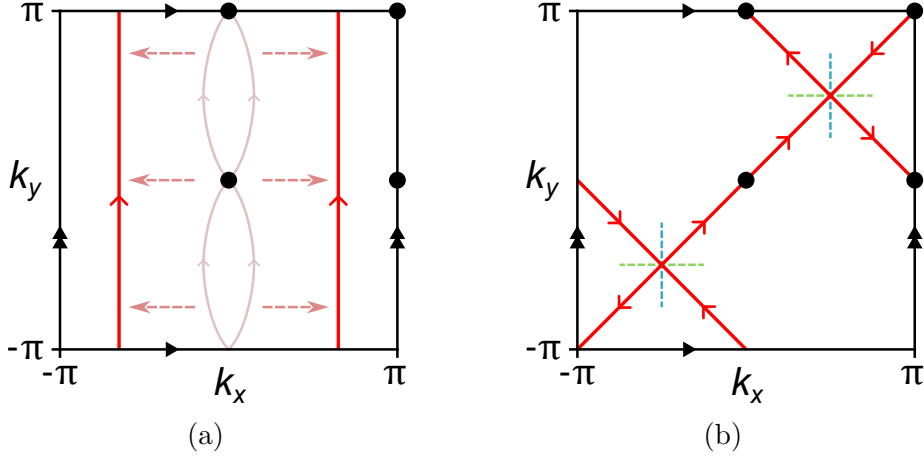


Figure 5.21: (a) Two copies of ℓ_{0y0} can be moved apart in opposite directions while respecting inversion symmetry. Moving the loops even further apart makes them intersect the TRIM at $k_x = \pi$ simultaneously, proving that in terms of twisted homology classes, $2[\ell_{0y0}] = 2[\ell_{\pi y0}]$. (b) Intermediate state between $\ell_{0y0} - \ell_{\pi y0}$ and $\ell_{x00} - \ell_{x\pi0}$. Detaching the intersections along the vertical blue dashed lines (as though cutting them with scissors) yields $\ell_{0y0} - \ell_{\pi y0}$, whereas cutting along the horizontal green lines gives $\ell_{x00} - \ell_{x\pi0}$.

generate independent \mathbb{Z} invariants. Instead, their difference must be a \mathbb{Z}_2 invariant:

$$2[\ell_{0y0}] = 2[\ell_{\pi y0}] \implies 2[\ell_{0y0} - \ell_{\pi y0}] = 0.$$

Furthermore, it can be shown that $[\ell_{0y0} - \ell_{\pi y0}] = [\ell_{x00} - \ell_{x\pi0}]$; this is illustrated in Figure 5.21(b). Using these and other similar relations, we find that the invariant group in Equation (5.24) is generated by the three \mathbb{Z} generators

$$\nu_x := [\ell_{x00}], \quad \nu_y := [\ell_{0y0}], \quad \nu_z := [\ell_{00z}],$$

and four \mathbb{Z}_2 generators

$$\begin{aligned} \nu_{xy} &:= [\ell_{x00} - \ell_{x\pi0}] = [\ell_{0y0} - \ell_{\pi y0}], & \nu_{xyz} &:= [\ell_{x00} - \ell_{x\pi0} - \ell_{x0\pi} + \ell_{x\pi\pi}] \\ \nu_{yz} &:= [\ell_{0y0} - \ell_{0y\pi}] = [\ell_{00z} - \ell_{0\pi z}], & &= [\ell_{0y0} - \ell_{\pi y0} - \ell_{0y\pi} + \ell_{\pi y\pi}] \\ \nu_{xz} &:= [\ell_{00z} - \ell_{\pi 0z}] = [\ell_{x00} - \ell_{x0\pi}], & &= [\ell_{00z} - \ell_{\pi 0z} - \ell_{0\pi z} + \ell_{\pi\pi z}]. \end{aligned}$$

We can translate directly between these twisted homology invariants and the invariants discussed in Section 5.4.1, namely the three Chern numbers $C_{x,y,z}$ and eight inversion eigenvalues $\zeta(\kappa)$ at the TRIM κ . First, note that the \mathbb{Z} generators all induce a Chern number of 1 in their respective directions, while the \mathbb{Z}_2 generators all have a zero Chern vector due to the loops running in opposite directions. This implies that the Chern vector is precisely indexed by the \mathbb{Z}^3 subgroup of the twisted homology.

The inversion eigenvalues ζ can be inferred by checking which TRIM are crossed by the loops in each of the generators: such crossings induce a sign change in the inversion eigenvalue. For example, each copy of ν_x changes the sign of ζ for the two

TRIM on the x axis, ν_{yz} affects the four TRIM on the yz -plane, and ν_{xyz} inverts the sign of ζ at all eight TRIM simultaneously. The total set of invariants can then be deduced from the combination of these actions. For instance, a topological state with twisted homology class $2\nu_x - \nu_y + \nu_{yz}$ has a Chern vector of $\mathbf{C} = (2, -1, 0)$ and negative inversion eigenvalues only at the two TRIM $\mathbf{k} = (0, 0, \pi)$ and $\mathbf{k} = (0, \pi, \pi)$.

Finally, the construction of all twisted Dirac string configurations, which exist in

$$H_1(M, W \cup \text{TRIM}; \tilde{\mathbb{Z}}) \cong \mathbb{Z}^3 \oplus \mathbb{Z}_2^4 \oplus \mathbb{Z}^r,$$

proceeds more or less the same as in Ref. [7]: any given charge configuration on the set W of Weyl points in the effective Brillouin zone fixes a unique element in the summand \mathbb{Z}^r . There then remain $\mathbb{Z}^3 \oplus \mathbb{Z}_2^4$ different twisted Dirac string configurations, which are precisely generated by the action of the insulating group. To be precise, there is no canonical “zero” configuration, so one needs to fix a reference configuration and then obtain all other configurations by adding twisted Dirac loops from $\mathbb{Z}^3 \oplus \mathbb{Z}_2^4$. It should be noted that this choice of a reference configuration means that the $\mathbb{Z}^3 \oplus \mathbb{Z}_2^4$ subgroup does not correspond to the Chern numbers and inversion eigenvalues in the same canonical way as before. However, the inversion eigenvalues can still be obtained from the twisted Dirac strings by inspection: each TRIM κ that is crossed by a Dirac string has $\zeta(\kappa) = -1$.

All in all, our heuristic approach to describing the invariants for this system has yielded a classification that appears highly plausible, in that all its major features agree with the properties of the system. Not only does this offer a useful platform for studying the semimetal invariants of this system directly, but it also demonstrates again the usefulness of the twisted homology point of view, and serves as a jumping off point for the classification of other symmetries featuring high-symmetry points. It also shows that the need for fully rigorous mathematical descriptions in terms of vector bundle classification can be bypassed based on more direct reasoning, at least in some cases. There is unquestionable value in these more rigorous methods, but it is often the more direct approaches which afford the greatest intuition—a quality that can be invaluable in developing proper physical understanding.

Chapter 6

Conclusions and outlook

In this chapter, we take stock of the current state of the research performed in this work. We begin in Section 6.1 by briefly summarising the key results presented in Chapter 5. We then expand on some avenues of possible further research in Section 6.2, speculating on specific lines of inquiry where appropriate.

6.1 Summary of main results

The central results of this thesis are focused around gaining a deeper understanding of how non-orientability in momentum space alters the topological description of Weyl semimetals—a state of matter that is fundamentally chiral in nature. This was achieved in large part by applying the appropriate tools from algebraic topology to a glide symmetric system featuring a Brillouin zone with $K^2 \times S^1$ topology, of which some important properties had already been established in Ref. [25].

Contextualisation of the Poincaré–Hopf theorem

An important aspect of obtaining a cogent topological description lies in deciding which tools from topology are suitable to use in the first place. To this end, we have placed the role that the Poincaré–Hopf theorem plays in deriving the Nielsen–Ninomiya charge cancellation on firmer theoretical footing. In three dimensions, Poincaré–Hopf states that the singularities of a tangent vector field on a compact manifold should have topological indices which sum to zero. Nielsen–Ninomiya is then usually derived by noting that the $\mathbf{h}(\mathbf{k})$ appearing in the model Hamiltonian can be considered such a tangent vector field. We note that this is categorically not the case on non-orientable manifolds; in this context, \mathbf{h} is a section of the trivial \mathbb{R}^3 -bundle over the manifold, rather than the tangent bundle on which tangent vector fields are defined. The mismatch in orientability between the base manifold and the \mathbb{R}^3 -bundle is precisely what causes the Poincaré–Hopf/Nielsen–Ninomiya theorems to become modified to a mod 2 charge cancellation.

Formalism for obtaining twisted coefficients

In order to obtain a full classification in terms of homology and cohomology on a non-orientable system, one needs to decide how to restore Poincaré duality. This is

done by twisting the coefficients of either the homology or the cohomology; only one of these choices yields accurate topological invariants. The correct twisting is usually motivated using arguments relating to vector bundle classification. These arguments are relatively tractable for a free unitary action such as the one featured in the $K^2 \times S^1$ system, but they quickly become conceptually involved when studying more complex symmetries (i.e. those that have fixed points, are anti-unitary, etc.), requiring much mathematical legwork to be done in order to obtain the final topological invariants.

To remedy this situation, we have demonstrated that a highly straightforward heuristic arises in the specific context of Weyl semimetals: one can study how a given orientation-reversing symmetry acts on Weyl points. If the symmetric partner of a Weyl point has the same chirality, this indicates a twist in the cohomology, and if it has the opposite chirality, the twist is in the homology. This twist then carries over to the underlying insulating topology, so that this heuristic is also useful for classifying those insulating phases which are mediated by transitional Weyl semimetals. In particular, we demonstrate that orientation-reversing unitary symmetries must always be described using twisted homology.

This formalism does not always uniquely identify the correct classifying groups; if the symmetry is not free, one needs to study how its fixed points are treated in the equivariant homology and cohomology. Nevertheless, these features may also be assessable using heuristic approaches, depending on the system. In any case, the formalism is useful for developing physical intuition, and it serves as a good sanity check in classification schemes making use of these twisted groups—especially those involving anti-unitary symmetries.

Classification of $K^2 \times S^1$ bulk and K^2 surface invariants

We have provided a full classification and interpretation of the topological invariants on the $K^2 \times S^1$ system arising from a single momentum space glide symmetry, based on the explicitly calculated Mayer–Vietoris sequence in Equation (5.11). This includes both the insulating invariants, which are classified by $\mathbb{Z} \oplus \mathbb{Z}_2$, and the semimetal invariants, classified by $\mathbb{Z} \oplus \mathbb{Z}_2 \oplus \mathbb{Z}^k$ with k the number of Weyl points on $K^2 \times S^1$. Aside from the \mathbb{Z}_2 invariant ν_z which has been well studied previously, we have also described a seemingly novel \mathbb{Z} invariant ν_x . We have demonstrated how ν_x and ν_z can be obtained from the action of the glide symmetry on two of the basic homology invariants in $H_1(\mathbb{T}^3) \cong \mathbb{Z}^3$, and how the third invariant is trivialised by the same action. Based on these observations, we have provided two integral equations for explicit calculation of ν_x : Equation (5.13) in terms of a simple Chern number in the insulating context, and Equation (5.16) in terms of curved planes in the semimetallic context. This illustrates the usefulness of the twisted homology point of view.

We have also provided a classification of the surface states arising from truncation in the periodic S^1 direction, in the form of the Mayer–Vietoris sequence in Equation (5.19). This sequence has very similar features to the bulk $K^2 \times S^1$ sequence, save for the fact that the \mathbb{Z}_2 invariant ν_z is projected out.

Clarification of mod 2 charge cancellation

The Mayer–Vietoris sequence in Equation (5.11) also provides a more solid conceptual basis for the mod 2 charge cancellation on $K^2 \times S^1$ described in Ref. [25]. It relates to the fact that the charges of all Weyl points must sum to zero in the group $H^2(K^2 \times S^1) \cong \mathbb{Z}_2$, which appears where a \mathbb{Z} group would usually be in the orientable case. This is closely related to the lack of a canonical orientation at each Weyl point. In particular, it follows that the total chirality is ill defined as an integer, being sensitive to arbitrary local choices of orientation (or equivalently, choice of a fundamental domain). We assert that this amounts to an unphysical degree of freedom, so that any apparent net non-zero chirality should have no phenomenological consequences.

Classification of non-orientable Brillouin zones

Through use of the theory of space groups, we have ascertained that there are exactly three other symmetry groups in three dimensions besides the single glide symmetry which have a free action giving rise to a non-orientable fundamental Brillouin zone: Cc , $Pca2_1$ and $Pna2_1$. Just as for $K^2 \times S^1$, we have provided explicitly calculated Mayer–Vietoris sequences for each of these three systems. Each of them features the same \mathbb{Z}_2 charge cancellation as $K^2 \times S^1$; the differences lie in the insulating invariants. Explicitly, the insulating phases under Cc symmetry are classified by $\mathbb{Z} \oplus \mathbb{Z}_2^2$, those under $Pca2_1$ are given by \mathbb{Z}_2^2 and those under $Pna2_1$ are given by \mathbb{Z}_4 . This latter group is especially interesting, featuring a topological invariant of order four.

Classification of inversion symmetric invariants

Finally, we have used a heuristic ansatz to derive a Mayer–Vietoris sequence for Weyl semimetals with inversion symmetry. These materials comprise an important class of experimentally verified magnetic Weyl semimetals. The Mayer–Vietoris sequence given in Equation (5.23) correctly predicts that no form of charge cancellation occurs within the effective Brillouin zone, and it classifies a set of insulating invariants that agrees precisely with existing works. Consequently, our ansatz leads to the correct classification of semimetallic invariants.

Importantly, this demonstrates that there are cases in which a system with high-symmetry points can nonetheless be correctly classified using relatively elementary tools such as ordinary cellular homology. This alleviates the need to resort to more conceptually involved arguments relying on equivariant cohomology and the related vector bundle classification, which often lead to challenging calculations.

6.2 Research recommendations

We close this thesis by making an inventory of the open questions that remain, along with some possible applications and experimental realisations.

The biggest caveat that comes with the results contained in this work is that the Bloch Hamiltonian formalism that we have relied on necessarily gives rise to a

two-band description. As a result, the applicability of our results may be limited under addition of more bands, especially when those bands are non-trivial—for example, four-band models incorporating both spin and orbital degrees of freedom may not be readily captured using cohomology in two or three dimensions. Defining more precisely what the scope of such descriptions is would be a great step forward in generality.

One of the biggest questions that merit more exploration with regards to the classification on $K^2 \times S^1$ is that relating to its surface states. In particular, while we have classified the surface states resulting from truncation in the periodic S^1 direction, the projections in the other two coordinate directions are more difficult to make sense of. In particular, it is worth exploring whether the yz surface can be described using the unusual twist in both homology and cohomology that we have described, and how the groups should be calculated explicitly if this is the case.

On the topic of two-dimensional descriptions, the two-dimensional surface Mayer–Vietoris sequence in Equation (5.19) may find some applications outside of its original context of surface modes. Perhaps the most straightforward of these are the proper two-dimensional Weyl semimetals, which are usually protected by chiral symmetry [115]. Class AIII 2D semimetals in particular have very similar topological features to those on the surface of 3D class A semimetals. Despite their apparent topological similarity, the two descriptions are substantially different: the surface of a three-dimensional Weyl semimetal hosts gapless Fermi arcs, while their topological equivalent in 2D class AIII features bulk Dirac strings which project onto Fermi arcs on the one-dimensional surfaces. Finding a canonical topological mapping between these two types of systems may be an important step in the full classification of two-dimensional Weyl semimetals. Incidentally, the two-dimensional chiral Weyl semimetals in classes BDI and CII both feature orientation-preserving symmetries which nevertheless invert Weyl point chiralities, and just as on the yz surface of $K^2 \times S^1$, a description in terms of more generalised twisted coefficients may prove useful.

A somewhat more indirect, but at least as important application of the two-dimensional topology may come in the classification of certain non-Hermitian systems. This rapidly-growing field of physics uses non-Hermitian Hamiltonians in order to model systems with, e.g., physical gains and losses. Non-Hermitian systems feature special band degeneracies called *exceptional points*, where not only the (complex) energy eigenvalues, but also their associated eigenstates coincide. These exceptional points have important features in common with Weyl points. Two works have recently gone into preprint which link this non-Hermitian physics quite directly to the work performed in this thesis. First, Lukas König, Kang Yang et al. have studied how exceptional points behave when the Brillouin zone is a two-dimensional non-orientable manifold [104]. Similar features were observed to those of the Weyl points on $K^2 \times S^1$, including the reversal of chirality across certain boundaries of the Brillouin zone. Second, a work by Marcus Stålhammar and Lukas Rødland details how non-Hermitian systems with exceptional points can be canonically mapped to equivalent Hermitian Weyl semimetals, upon which they can be classified topologically using the same machinery we have employed here [128]. Based on this description, it should be relatively straightforward to study the non-orientable features in Ref. [104]

in terms of the analysis that we have already performed on Weyl semimetals.

Another aspect of our results that can be expanded upon is that of the three additional fundamental non-orientable Brillouin zones we have identified, i.e. those arising under the action of the space groups Cc , $Pca2_1$ and $Pna2_1$. We have provided a full classification of invariants for each of these spaces in terms of a Mayer–Vietoris sequence, but the physical interpretation of these invariants and the topology of the underlying Brillouin zone can certainly be elucidated further. As we have demonstrated in this work, twisted homology tends to provide an intuitive platform for the study of these invariants, and so we recommend that the relevant homology description be given attention especially. The space group $Pna2_1$ seems to give rise to particularly promising topology, being classified by a single \mathbb{Z}_4 insulating invariant. The insulating invariants of these spaces may also be probed experimentally in the context of acoustic crystals; as we have reviewed, the gauge fluxes necessary to realise momentum-space non-symmorphic symmetries can be implemented with ease there. The precise projective representations that these fluxes need to enact to give rise to each of these symmetries can be found listed in the supplement of Ref. [101].

On the topic of acoustic crystals, Weyl semimetals have been successfully reproduced experimentally in these materials [129–132]. Combining these semimetal realisations with gauge fluxes may provide a platform to study semimetal physics directly under non-symmorphic symmetries. Veering into speculation for a moment, being able to study the transport properties of such materials may help confirm that no net chiral anomaly appears at sufficiently large scales.

Finally, it may be worth exploring whether there are other symmetries besides inversion for which a similarly heuristic line of reasoning to that given in Section 5.4.2 can be given. Alternatively, it may be possible to further develop a formalism for treating high-symmetry points in symmetric semimetals. Such a formalism would allow for rapid calculation and interpretation of invariants for any given orientation-reversing symmetry.

Bibliography

- [1] David S Simon. “Topology and physics: a historical overview”. In: *Tying Light in Knots*. 2053-2571. Morgan & Claypool Publishers, 2018, 1-1 to 1–7. ISBN: 978-1-64327-234-4. DOI: 10.1088/2053-2571/aadd5ch1.
- [2] *Press release: The 1985 Nobel Prize in Physics*. 1985. URL: <https://www.nobelprize.org/prizes/physics/1985/press-release/> (visited on 07/03/2025).
- [3] Pascal Gehring et al. “A Natural Topological Insulator”. In: *Nano Letters* 13.3 (Mar. 2013), pp. 1179–1184. ISSN: 1530-6992. DOI: 10.1021/nl304583m. URL: <http://dx.doi.org/10.1021/nl304583m>.
- [4] Wendel S. Paz et al. “Franckeite as an Exfoliable Naturally Occurring Topological Insulator”. In: *Nano Letters* 21.18 (2021). PMID: 34461016, pp. 7781–7788. DOI: 10.1021/acs.nanolett.1c02742.
- [5] *Press release: The Nobel Prize in Physics 2016*. 2016. URL: <https://www.nobelprize.org/prizes/physics/2016/press-release/> (visited on 07/03/2025).
- [6] Masatoshi Sato and Yoichi Ando. “Topological superconductors: a review”. In: *Reports on Progress in Physics* 80.7 (May 2017), p. 076501. ISSN: 1361-6633. DOI: 10.1088/1361-6633/aa6ac7. URL: <http://dx.doi.org/10.1088/1361-6633/aa6ac7>.
- [7] Varghese Mathai and Guo Chuan Thiang. “Differential Topology of Semimetals”. In: *Communications in Mathematical Physics* 355.2 (July 2017), pp. 561–602. ISSN: 1432-0916. DOI: 10.1007/s00220-017-2965-z. URL: <http://dx.doi.org/10.1007/s00220-017-2965-z>.
- [8] Wenting Cheng et al. “Revealing topology in metals using experimental protocols inspired by K-theory”. In: *Nature Communications* 14.1 (May 2023), p. 3071. ISSN: 2041-1723. DOI: 10.1038/s41467-023-38862-2.
- [9] Hermann Weyl. “Gravitation and the Electron”. In: *Proc Natl Acad Sci U S A* 15.4 (Apr. 1929), pp. 323–334. URL: <https://www.jstor.org/stable/85331>.
- [10] Xiangang Wan et al. “Topological semimetal and Fermi-arc surface states in the electronic structure of pyrochlore iridates”. In: *Phys. Rev. B* 83 (20 May 2011), p. 205101. DOI: 10.1103/PhysRevB.83.205101. URL: <https://link.aps.org/doi/10.1103/PhysRevB.83.205101>.

- [11] Su-Yang Xu et al. “Discovery of a Weyl fermion semimetal and topological Fermi arcs”. In: *Science* 349.6248 (Aug. 2015), pp. 613–617. DOI: [10.1126/science.aaa9297](https://doi.org/10.1126/science.aaa9297).
- [12] Su-Yang Xu et al. “Experimental discovery of a topological Weyl semimetal state in TaP”. In: *Science Advances* 1.10 (Nov. 2015). DOI: [10.1126/sciadv.1501092](https://doi.org/10.1126/sciadv.1501092).
- [13] Lexian Yang, Zhongkai Liu, Yan Sun et al. “Weyl semimetal phase in the non-centrosymmetric compound TaAs”. In: *Nature Physics* 11.9 (Sept. 2015), pp. 728–732. DOI: [10.1038/nphys3425](https://doi.org/10.1038/nphys3425).
- [14] Baiqing Lyu et al. “Observation of Weyl nodes in TaAs”. In: *Nature Physics* 11.9 (Sept. 2015), pp. 724–727. DOI: [10.1038/nphys3426](https://doi.org/10.1038/nphys3426).
- [15] Chandra Shekhar et al. “Extremely large magnetoresistance and ultrahigh mobility in the topological Weyl semimetal candidate NbP”. In: *Nature Physics* 11.8 (Aug. 2015), pp. 645–649. ISSN: 1745-2481. DOI: [10.1038/nphys3372](https://doi.org/10.1038/nphys3372).
- [16] Gavin B. Osterhoudt et al. “Colossal mid-infrared bulk photovoltaic effect in a type-I Weyl semimetal”. In: *Nature Materials* 18.5 (May 2019), pp. 471–475. DOI: [10.1038/s41563-019-0297-4](https://doi.org/10.1038/s41563-019-0297-4).
- [17] Xu Yang, Kenneth Burch, and Ying Ran. *Divergent bulk photovoltaic effect in Weyl semimetals*. 2018. arXiv: 1712.09363 [cond-mat.mes-hall]. URL: <https://arxiv.org/abs/1712.09363>.
- [18] Holgar B. Nielsen and Masao Ninomiya. “Absence of neutrinos on a lattice: (I). Proof by homotopy theory”. In: *Nuclear Physics B* 185.1 (1981), pp. 20–40. ISSN: 0550-3213. DOI: [https://doi.org/10.1016/0550-3213\(81\)90361-8](https://doi.org/10.1016/0550-3213(81)90361-8). URL: <https://www.sciencedirect.com/science/article/pii/0550321381903618>.
- [19] Holgar B. Nielsen and Masao Ninomiya. “Absence of neutrinos on a lattice: (II). Intuitive topological proof”. In: *Nuclear Physics B* 193.1 (1981), pp. 173–194. ISSN: 0550-3213. DOI: [https://doi.org/10.1016/0550-3213\(81\)90524-1](https://doi.org/10.1016/0550-3213(81)90524-1). URL: <https://www.sciencedirect.com/science/article/pii/0550321381905241>.
- [20] Shumeng Chi et al. “Symmetrical broken and nonlinear response of Weyl semimetal TaAs influenced by the topological surface states and Weyl nodes”. In: *Annalen der Physik* 529.4 (Feb. 2017). ISSN: 1521-3889. DOI: [10.1002/andp.201600359](https://doi.org/10.1002/andp.201600359). URL: <http://dx.doi.org/10.1002/andp.201600359>.
- [21] Z. Y. Chen, Shengyuan A. Yang, and Yuxin Zhao. “Brillouin Klein bottle from artificial gauge fields”. In: *Nature Communications* 13.2215 (Apr. 2022). DOI: [10.1038/s41467-022-29953-7](https://doi.org/10.1038/s41467-022-29953-7).
- [22] Yu-Liang Tao, Mou Yan et al. “Higher-order Klein bottle topological insulator in three-dimensional acoustic crystals”. In: *Phys. Rev. B* 109 (13 Apr. 2024), p. 134107. DOI: [10.1103/PhysRevB.109.134107](https://doi.org/10.1103/PhysRevB.109.134107). URL: <https://link.aps.org/doi/10.1103/PhysRevB.109.134107>.

- [23] Zhenxiao Zhu et al. “Brillouin Klein space and half-turn space in three-dimensional acoustic crystals”. In: *Science Bulletin* 69.13 (2024), pp. 2050–2058. ISSN: 2095-9273. DOI: <https://doi.org/10.1016/j.scib.2024.05.003>. URL: <https://www.sciencedirect.com/science/article/pii/S2095927324003372>.
- [24] Yanqiu Wang, Chen Zhang et al. *Chess-board Acoustic Crystals with Momentum-space Nonsymmorphic Symmetries*. 2023. arXiv: 2305.07174 [cond-mat.mes-hall]. URL: <https://arxiv.org/abs/2305.07174>.
- [25] André Grossi Fonseca, Sachin Vaidya et al. “Weyl Points on Nonorientable Manifolds”. In: *Phys. Rev. Lett.* 132 (26 June 2024), p. 266601. DOI: 10.1103/PhysRevLett.132.266601. URL: <https://link.aps.org/doi/10.1103/PhysRevLett.132.266601>.
- [26] Varghese Mathai and Guo Chuan Thiang. “Global topology of Weyl semimetals and Fermi arcs”. In: *Journal of Physics A: Mathematical and Theoretical* 50.11 (Feb. 2017), 11LT01. ISSN: 1751-8121. DOI: 10.1088/1751-8121/aa59b2. URL: <http://dx.doi.org/10.1088/1751-8121/aa59b2>.
- [27] Neil W Ashcroft and N David Mermin. *Solid state physics*. New York, NY: Holt, Rinehart and Winston, 1976. ISBN: 978-0030839931.
- [28] Felix Bloch. “Über die Quantenmechanik der Elektronen in kristallgittern”. In: *Zeitschrift für Physik* 52.7–8 (July 1929), pp. 555–600. DOI: 10.1007/bf01339455.
- [29] Sophia N. Potoczak. *Survey of Graph Embeddings into Compact Surfaces*. 2014. URL: <https://digitalcommons.library.umaine.edu/etd/2155> (visited on 07/04/2025).
- [30] Michael V. Berry. “Quantal phase factors accompanying adiabatic changes”. In: *Proc. R. Soc. Lond. A* 392 (Nov. 1984), pp. 45–57. DOI: 10.1098/rspa.1984.0023.
- [31] Douglas Natelson. *What is Berry phase?* 2018. URL: <https://nanoscale.blogspot.com/2018/07/what-is-berry-phase.html> (visited on 07/04/2025).
- [32] Allen Hatcher. *Algebraic Topology*. Cambridge: Cambridge Univ. Press, 2002. URL: <https://pi.math.cornell.edu/~hatcher/AT/ATpage.html> (visited on 10/07/2024).
- [33] Glen E. Bredon. *Topology and geometry*. 139. Springer International Publishing, 1993. ISBN: 978-1-4419-3103-0. DOI: 10.1007/978-1-4757-6848-0.
- [34] Raoul Bott and Loring W. Tu. *Differential Forms in Algebraic Topology*. 82. New York, NY: Springer Science+Business Media New York, 1982. ISBN: 978-1-4419-2815-3. DOI: 10.1007/978-1-4757-3951-0.
- [35] Daniel S. Freed and Gregory W. Moore. “Twisted Equivariant Matter”. In: *Annales Henri Poincaré* 14.8 (Dec. 2013), pp. 1927–2023. DOI: 10.1007/s00023-013-0236-x.

- [36] Guo Chuan Thiang. “On the K-Theoretic classification of topological phases of matter”. In: *Annales Henri Poincaré* 17.4 (Apr. 2016), pp. 757–794. DOI: 10.1007/s00023-015-0418-9.
- [37] Anton Akhmerov et al. *Online course on topology in condensed matter*. URL: <https://topocondmat.org/> (visited on 10/07/2024).
- [38] János K. Asbóth, László Oroszlány, and András Pályi. *A Short Course on Topological Insulators*. Springer International Publishing, 2016. ISBN: 9783319256078. DOI: 10.1007/978-3-319-25607-8. URL: <http://dx.doi.org/10.1007/978-3-319-25607-8>.
- [39] B. Andrei Bernevig and Taylor L. Hughes. *Topological insulators and topological superconductors*. Princeton University Press, 2013. ISBN: 978-0-691-15175-5. URL: <http://www.jstor.org/stable/j.ctt19cc2gc>.
- [40] Wu-Pei Su, John R. Schrieffer, and Alan J. Heeger. “Solitons in Polyacetylene”. In: *Phys. Rev. Lett.* 42 (25 June 1979), pp. 1698–1701. DOI: 10.1103/PhysRevLett.42.1698. URL: <https://link.aps.org/doi/10.1103/PhysRevLett.42.1698>.
- [41] Wu-Pei Su, John R. Schrieffer, and Alan J. Heeger. “Soliton excitations in polyacetylene”. In: *Phys. Rev. B* 22 (4 Aug. 1980), pp. 2099–2111. DOI: 10.1103/PhysRevB.22.2099. URL: <https://link.aps.org/doi/10.1103/PhysRevB.22.2099>.
- [42] Michael Freedman et al. “A class of P,T-invariant topological phases of interacting electrons”. In: *Annals of Physics* 310.2 (2004), pp. 428–492. ISSN: 0003-4916. DOI: <https://doi.org/10.1016/j.aop.2004.01.006>. URL: <https://www.sciencedirect.com/science/article/pii/S0003491604000260>.
- [43] Eric J. Meier, Fangzhao Alex An, and Bryce Gadway. “Observation of the topological soliton state in the Su–Schrieffer–Heeger model”. In: *Nat. Commun.* 7.1 (Dec. 2016), p. 13986. DOI: 10.1038/ncomms13986.
- [44] Marcos Atala et al. “Direct measurement of the Zak phase in topological Bloch bands”. In: *Nature Physics* 9.12 (Nov. 2013), pp. 795–800. ISSN: 1745-2481. DOI: 10.1038/nphys2790. URL: <http://dx.doi.org/10.1038/nphys2790>.
- [45] Andreas W W Ludwig. “Topological phases: classification of topological insulators and superconductors of non-interacting fermions, and beyond”. In: *Physica Scripta* T168 (Dec. 2015), p. 014001. ISSN: 1402-4896. DOI: 10.1088/0031-8949/2015/t168/014001.
- [46] Martin R. Zirnbauer. “Riemannian symmetric superspaces and their origin in random-matrix theory”. In: *Journal of Mathematical Physics* 37.10 (Oct. 1996), pp. 4986–5018. ISSN: 1089-7658. DOI: 10.1063/1.531675.
- [47] Alexander Altland and Martin R. Zirnbauer. “Nonstandard symmetry classes in mesoscopic normal-superconducting hybrid structures”. In: *Phys. Rev. B* 55 (2 Jan. 1997), pp. 1142–1161. DOI: 10.1103/PhysRevB.55.1142. URL: <https://link.aps.org/doi/10.1103/PhysRevB.55.1142>.

- [48] P. Heinzner, A. Huckleberry, and M.R. Zirnbauer. "Symmetry Classes of Disordered Fermions". In: *Communications in Mathematical Physics* 257.3 (May 2005), pp. 725–771. ISSN: 1432-0916. DOI: 10.1007/s00220-005-1330-9.
- [49] Ken Shiozaki, Masatoshi Sato, and Kiyonori Gomi. "Atiyah-Hirzebruch spectral sequence in band topology: General formalism and topological invariants for 230 space groups". In: *Phys. Rev. B* 106 (16 Oct. 2022), p. 165103. DOI: 10.1103/PhysRevB.106.165103. URL: <https://link.aps.org/doi/10.1103/PhysRevB.106.165103>.
- [50] Klaus v. Klitzing, G. Dorda, and M. Pepper. "New Method for High-Accuracy Determination of the Fine-Structure Constant Based on Quantized Hall Resistance". In: *Phys. Rev. Lett.* 45 (6 Aug. 1980), pp. 494–497. DOI: 10.1103/PhysRevLett.45.494. URL: <https://link.aps.org/doi/10.1103/PhysRevLett.45.494>.
- [51] Klaus von Klitzing. "The quantized Hall effect". In: *Rev. Mod. Phys.* 58 (3 July 1986), pp. 519–531. DOI: 10.1103/RevModPhys.58.519. URL: <https://link.aps.org/doi/10.1103/RevModPhys.58.519>.
- [52] David J. Thouless et al. "Quantized Hall Conductance in a Two-Dimensional Periodic Potential". In: *Phys. Rev. Lett.* 49 (6 Aug. 1982), pp. 405–408. DOI: 10.1103/PhysRevLett.49.405. URL: <https://link.aps.org/doi/10.1103/PhysRevLett.49.405>.
- [53] M. Zahid Hasan and Charles L. Kane. "Colloquium: Topological insulators". In: *Rev. Mod. Phys.* 82 (4 Nov. 2010), pp. 3045–3067. DOI: 10.1103/RevModPhys.82.3045. URL: <https://link.aps.org/doi/10.1103/RevModPhys.82.3045>.
- [54] F. Duncan M. Haldane. "Model for a Quantum Hall Effect without Landau Levels: Condensed-Matter Realization of the "Parity Anomaly"". In: *Phys. Rev. Lett.* 61 (18 Oct. 1988), pp. 2015–2018. DOI: 10.1103/PhysRevLett.61.2015. URL: <https://link.aps.org/doi/10.1103/PhysRevLett.61.2015>.
- [55] Charles L. Kane and Eugene J. Mele. "Quantum Spin Hall Effect in Graphene". In: *Phys. Rev. Lett.* 95 (22 Nov. 2005), p. 226801. DOI: 10.1103/PhysRevLett.95.226801. URL: <https://link.aps.org/doi/10.1103/PhysRevLett.95.226801>.
- [56] Charles L. Kane and Eugene J. Mele. " Z_2 Topological Order and the Quantum Spin Hall Effect". In: *Phys. Rev. Lett.* 95 (14 Sept. 2005), p. 146802. DOI: 10.1103/PhysRevLett.95.146802. URL: <https://link.aps.org/doi/10.1103/PhysRevLett.95.146802>.
- [57] Don-Ning Sheng et al. "Quantum Spin-Hall Effect and Topologically Invariant Chern Numbers". In: *Phys. Rev. Lett.* 97 (3 July 2006), p. 036808. DOI: 10.1103/PhysRevLett.97.036808. URL: <https://link.aps.org/doi/10.1103/PhysRevLett.97.036808>.

- [58] Joel E. Moore and Leon Balents. “Topological invariants of time-reversal-invariant band structures”. In: *Phys. Rev. B* 75 (12 Mar. 2007), p. 121306. DOI: 10.1103/PhysRevB.75.121306. URL: <https://link.aps.org/doi/10.1103/PhysRevB.75.121306>.
- [59] Xiao-Liang Qi, Taylor L. Hughes, and Shou-Cheng Zhang. “Topological field theory of time-reversal invariant insulators”. In: *Phys. Rev. B* 78 (19 Nov. 2008), p. 195424. DOI: 10.1103/PhysRevB.78.195424. URL: <https://link.aps.org/doi/10.1103/PhysRevB.78.195424>.
- [60] Giuseppe De Nittis and Kiyonori Gomi. “The cohomological nature of the Fu–Kane–Mele invariant”. In: *Journal of Geometry and Physics* 124 (2018), pp. 124–164. ISSN: 0393-0440. DOI: <https://doi.org/10.1016/j.geomphys.2017.10.007>. URL: <https://www.sciencedirect.com/science/article/pii/S0393044017302607>.
- [61] Severin Bunk and Richard J. Szabo. *Topological Insulators and the Kane-Mele Invariant: Obstruction and Localisation Theory*. 2019. arXiv: 1712.02991 [math-ph]. URL: <https://arxiv.org/abs/1712.02991>.
- [62] N. Peter Armitage, Eugene J. Mele, and Ashvin Vishwanath. “Weyl and Dirac semimetals in three-dimensional solids”. In: *Rev. Mod. Phys.* 90 (1 Jan. 2018), p. 015001. DOI: 10.1103/RevModPhys.90.015001. URL: <https://link.aps.org/doi/10.1103/RevModPhys.90.015001>.
- [63] Pavan Hosur and Xiaoliang Qi. “Recent developments in transport phenomena in Weyl semimetals”. In: *Comptes Rendus Physique* 14.9 (2013). Topological insulators / Isolants topologiques, pp. 857–870. ISSN: 1631-0705. DOI: <https://doi.org/10.1016/j.crhy.2013.10.010>. URL: <https://www.sciencedirect.com/science/article/pii/S1631070513001710>.
- [64] Conyers Herring. “Accidental Degeneracy in the Energy Bands of Crystals”. In: *Phys. Rev.* 52 (4 Aug. 1937), pp. 365–373. DOI: 10.1103/PhysRev.52.365. URL: <https://link.aps.org/doi/10.1103/PhysRev.52.365>.
- [65] Yang Zhang, Yan Sun, and Binghai Yan. “Berry curvature dipole in Weyl semimetal materials: An ab initio study”. In: *Phys. Rev. B* 97 (4 Jan. 2018), p. 041101. DOI: 10.1103/PhysRevB.97.041101. URL: <https://link.aps.org/doi/10.1103/PhysRevB.97.041101>.
- [66] Anton A. Burkov. “Weyl Metals”. In: *Annual Review of Condensed Matter Physics* 9.1 (Mar. 2018), pp. 359–378. ISSN: 1947-5462. DOI: 10.1146/annurev-conmatphys-033117-054129.
- [67] C. N. Wang et al. “Weyl fermion excitations in the ideal Weyl semimetal CuTlSe₂”. In: *Phys. Rev. Res.* 6 (3 Sept. 2024), p. 033229. DOI: 10.1103/PhysRevResearch.6.033229. URL: <https://link.aps.org/doi/10.1103/PhysRevResearch.6.033229>.
- [68] Alexey A. Soluyanov et al. “Type-II Weyl semimetals”. In: *Nature* 527.7579 (Nov. 2015), pp. 495–498. DOI: 10.1038/nature15768.

- [69] Minping Zhang, Zongxian Yang, and Guangtao Wang. “Coexistence of Type-I and Type-II Weyl Points in the Weyl-Semimetal OsC₂”. In: *The Journal of Physical Chemistry C* 122.6 (Feb. 2018), pp. 3533–3538. ISSN: 1932-7447. DOI: 10.1021/acs.jpcc.8b00920.
- [70] Leon Balents. “Weyl electrons kiss”. In: *Physics* 4.36 (May 2011). DOI: 10.1103/Physics.4.36.
- [71] Su-Yang Xu et al. “Discovery of a Weyl fermion state with Fermi arcs in niobium arsenide”. In: *Nature Physics* 11.9 (Sept. 2015), pp. 748–754. DOI: 10.1038/nphys3437.
- [72] Ilya Belopolski et al. “Signatures of a time-reversal symmetric Weyl semimetal with only four Weyl points”. In: *Nature Communications* 8.1 (Oct. 2017), p. 942. DOI: 10.1038/s41467-017-00938-1.
- [73] Gui-Geng Liu et al. “Topological Chern vectors in three-dimensional photonic crystals”. In: *Nature* 609 (2022), pp. 925–930. DOI: 10.1038/s41586-022-05077-2.
- [74] Hongming Weng et al. “Weyl Semimetal Phase in Noncentrosymmetric Transition-Metal Monophosphides”. In: *Phys. Rev. X* 5 (1 Mar. 2015), p. 011029. DOI: 10.1103/PhysRevX.5.011029. URL: <https://link.aps.org/doi/10.1103/PhysRevX.5.011029>.
- [75] Shin-Ming Huang et al. “A Weyl Fermion semimetal with surface Fermi arcs in the transition metal monopnictide TaAs class”. In: *Nature Communications* 6.1 (June 2015), p. 7373. DOI: 10.1038/ncomms8373.
- [76] Ilya Belopolski et al. “Discovery of a new type of topological Weyl fermion semimetal state in Mo_xW_{1-x}Te₂”. In: *Nature Communications* 7.1 (Dec. 2016), p. 13643. DOI: 10.1038/ncomms13643.
- [77] Defa Liu, Aiji Liang, Enke Liu, Qiunan Xu et al. “Magnetic Weyl semimetal phase in a Kagomé Crystal”. In: *Science* 365.6459 (Sept. 2019), pp. 1282–1285. DOI: 10.1126/science.aav2873.
- [78] Ilya Belopolski et al. “Discovery of topological Weyl fermion lines and drum-head surface states in a room temperature magnet”. In: *Science* 365.6459 (Sept. 2019), pp. 1278–1281. DOI: 10.1126/science.aav2327.
- [79] Noam Morali et al. “Fermi-arc diversity on surface terminations of the magnetic Weyl semimetal Co₃Sn₂S₂”. In: *Science* 365.6459 (Sept. 2019), pp. 1286–1291. DOI: 10.1126/science.aav2334.
- [80] Daniel S. Sanchez et al. “Observation of Weyl fermions in a magnetic non-centrosymmetric crystal”. In: *Nature Communications* 11.1 (July 2020), p. 3356. DOI: 10.1038/s41467-020-16879-1.
- [81] Anup Pradhan Sakhya et al. “Observation of Fermi arcs and Weyl nodes in a noncentrosymmetric magnetic Weyl semimetal”. In: *Phys. Rev. Mater.* 7 (5 May 2023), p. L051202. DOI: 10.1103/PhysRevMaterials.7.L051202. URL: <https://link.aps.org/doi/10.1103/PhysRevMaterials.7.L051202>.

- [82] Cong Li et al. “Emergence of Weyl fermions by ferrimagnetism in a noncentrosymmetric magnetic Weyl semimetal”. In: *Nature Communications* 14.1 (Nov. 2023), p. 7185. DOI: 10.1038/s41467-023-42996-8.
- [83] David Vanderbilt. *Berry Phases in Electronic Structure Theory: Electric Polarization, Orbital Magnetization and Topological Insulators*. Cambridge University Press, 2018, pp. 215–218. DOI: <https://doi.org/10.1017/9781316662205>.
- [84] Chiara Devescovi et al. “Cubic 3D Chern photonic insulators with orientable large Chern vectors”. In: *Nature Communications* 12.1 (Dec. 2021), p. 7330. DOI: 10.1038/s41467-021-27168-w.
- [85] Guo Chuan Thiang, Koji Sato, and Kiyonori Gomi. “Fu–Kane–Mele monopoles in semimetals”. In: *Nuclear Physics B* 923 (Oct. 2017), pp. 107–125. ISSN: 0550-3213. DOI: 10.1016/j.nuclphysb.2017.07.018. URL: <http://dx.doi.org/10.1016/j.nuclphysb.2017.07.018>.
- [86] Giuseppe De Nittis and Kiyonori Gomi. “Classification of “Quaternionic” Bloch-Bundles”. In: *Communications in Mathematical Physics* 339.1 (Oct. 2015), pp. 1–55. DOI: 10.1007/s00220-015-2390-0.
- [87] Hoi Chun Po, Ashvin Vishwanath, and Haruki Watanabe. “Symmetry-based indicators of band topology in the 230 space groups”. In: *Nature Communications* 8.1 (June 2017), p. 50. ISSN: 2041-1723. DOI: 10.1038/s41467-017-00133-2.
- [88] Zhijun Wang et al. “Hourglass fermions”. In: *Nature* 532.7598 (Apr. 2016), pp. 189–194. DOI: 10.1038/nature17410.
- [89] Yige Chen, Heung-Sik Kim, and Hae-Young Kee. “Topological crystalline semimetals in nonsymmorphic lattices”. In: *Phys. Rev. B* 93 (15 Apr. 2016), p. 155140. DOI: 10.1103/PhysRevB.93.155140. URL: <https://link.aps.org/doi/10.1103/PhysRevB.93.155140>.
- [90] Heejae Kim and Shuichi Murakami. “Emergent spinless Weyl semimetals between the topological crystalline insulator and normal insulator phases with glide symmetry”. In: *Phys. Rev. B* 93 (19 May 2016), p. 195138. DOI: 10.1103/PhysRevB.93.195138. URL: <https://link.aps.org/doi/10.1103/PhysRevB.93.195138>.
- [91] Ken Shiozaki, Masatoshi Sato, and Kiyonori Gomi. “Topology of nonsymmorphic crystalline insulators and superconductors”. In: *Phys. Rev. B* 93 (19 May 2016), p. 195413. DOI: 10.1103/PhysRevB.93.195413. URL: <https://link.aps.org/doi/10.1103/PhysRevB.93.195413>.
- [92] Tomáš Bzdušek et al. “Nodal-chain metals”. In: *Nature* 538.7623 (Aug. 2016), pp. 75–78. DOI: 10.1038/nature19099.
- [93] Benjamin J. Wieder and C. L. Kane. “Spin-orbit semimetals in the layer groups”. In: *Phys. Rev. B* 94 (15 Oct. 2016), p. 155108. DOI: 10.1103/PhysRevB.94.155108. URL: <https://link.aps.org/doi/10.1103/PhysRevB.94.155108>.

- [94] Yuxin Zhao and Andreas P. Schnyder. “Nonsymmorphic symmetry-required band crossings in topological semimetals”. In: *Phys. Rev. B* 94 (19 Nov. 2016), p. 195109. DOI: 10.1103/PhysRevB.94.195109. URL: <https://link.aps.org/doi/10.1103/PhysRevB.94.195109>.
- [95] Bohm-Jung Yang et al. “Topological semimetals protected by off-centered symmetries in nonsymmorphic crystals”. In: *Phys. Rev. B* 95 (7 Feb. 2017), p. 075135. DOI: 10.1103/PhysRevB.95.075135. URL: <https://link.aps.org/doi/10.1103/PhysRevB.95.075135>.
- [96] Luyang Wang, Shao-Kai Jian, and Hong Yao. “Hourglass semimetals with nonsymmorphic symmetries in three dimensions”. In: *Phys. Rev. B* 96 (7 Aug. 2017), p. 075110. DOI: 10.1103/PhysRevB.96.075110. URL: <https://link.aps.org/doi/10.1103/PhysRevB.96.075110>.
- [97] Shan-Shan Wang et al. “Hourglass Dirac chain metal in rhenium dioxide”. In: *Nature Communications* 8.1 (Nov. 2017), p. 1844. DOI: 10.1038/s41467-017-01986-3.
- [98] Benjamin J. Wieder et al. “Wallpaper fermions and the nonsymmorphic Dirac insulator”. In: *Science* 361.6399 (July 2018), pp. 246–251. ISSN: 1095-9203. DOI: 10.1126/science.aan2802. URL: <http://dx.doi.org/10.1126/science.aan2802>.
- [99] Xiaoliang Xiao et al. “Ideal hourglass-type charge-three Weyl fermions in spinless systems”. In: *Phys. Rev. B* 109 (7 Feb. 2024), p. 075160. DOI: 10.1103/PhysRevB.109.075160. URL: <https://link.aps.org/doi/10.1103/PhysRevB.109.075160>.
- [100] Rui-Xing Zhang and Chao-Xing Liu. *Nonsymmorphic Symmetry Protected Dirac, Möbius, and Hourglass Fermions in Topological Materials*. 2022. arXiv: 2207.00020 [cond-mat.mes-hall]. URL: <https://arxiv.org/abs/2207.00020>.
- [101] Chen Zhang et al. “General Theory of Momentum-Space Nonsymmorphic Symmetry”. In: *Phys. Rev. Lett.* 130 (25 June 2023), p. 256601. DOI: 10.1103/PhysRevLett.130.256601. URL: <https://link.aps.org/doi/10.1103/PhysRevLett.130.256601>.
- [102] Jinbing Hu, Songlin Zhuang, and Yi Yang. “Higher-Order Topological Insulators via Momentum-Space Nonsymmorphic Symmetries”. In: *Phys. Rev. Lett.* 132 (21 May 2024), p. 213801. DOI: 10.1103/PhysRevLett.132.213801. URL: <https://link.aps.org/doi/10.1103/PhysRevLett.132.213801>.
- [103] Yu-Liang Tao, Jiong-Hao Wang, and Yong Xu. *Quadrupole Insulator without Corner States in the Energy Spectrum*. 2023. arXiv: 2307.00486 [cond-mat.mes-hall]. URL: <https://arxiv.org/abs/2307.00486>.
- [104] J. Lukas K. König, Kang Yang et al. *Exceptional Topology on Nonorientable Manifolds*. 2025. arXiv: 2503.04889 [cond-mat.mes-hall]. URL: <https://arxiv.org/abs/2503.04889>.

- [105] Z. Y. Chen et al. “Classification of time-reversal-invariant crystals with gauge structures”. In: *Nature Communications* 14.1 (Feb. 2023), p. 743. DOI: 10.1038/s41467-023-36447-7.
- [106] Yuxin Zhao, Yue-Xin Huang, and Shengyuan A. Yang. “ \mathbb{Z}_2 -projective translational symmetry protected topological phases”. In: *Phys. Rev. B* 102 (16 Oct. 2020), p. 161117. DOI: 10.1103/PhysRevB.102.161117. URL: <https://link.aps.org/doi/10.1103/PhysRevB.102.161117>.
- [107] Yuxin Zhao et al. “Switching Spinless and Spinful Topological Phases with Projective PT Symmetry”. In: *Phys. Rev. Lett.* 126 (19 May 2021), p. 196402. DOI: 10.1103/PhysRevLett.126.196402. URL: <https://link.aps.org/doi/10.1103/PhysRevLett.126.196402>.
- [108] L. B. Shao et al. “Gauge-Field Extended $k \cdot p$ Method and Novel Topological Phases”. In: *Phys. Rev. Lett.* 127 (7 Aug. 2021), p. 076401. DOI: 10.1103/PhysRevLett.127.076401. URL: <https://link.aps.org/doi/10.1103/PhysRevLett.127.076401>.
- [109] Haoran Xue, Zihao Wang et al. “Projectively Enriched Symmetry and Topology in Acoustic Crystals”. In: *Phys. Rev. Lett.* 128 (11 Mar. 2022), p. 116802. DOI: 10.1103/PhysRevLett.128.116802. URL: <https://link.aps.org/doi/10.1103/PhysRevLett.128.116802>.
- [110] Tianzi Li, Juan Du et al. “Acoustic Möbius Insulators from Projective Symmetry”. In: *Phys. Rev. Lett.* 128 (11 Mar. 2022), p. 116803. DOI: 10.1103/PhysRevLett.128.116803. URL: <https://link.aps.org/doi/10.1103/PhysRevLett.128.116803>.
- [111] Andreas Leonhardt et al. “Symmetry-enforced topological band crossings in orthorhombic crystals: Classification and materials discovery”. In: *Phys. Rev. Mater.* 5 (12 Dec. 2021), p. 124202. DOI: 10.1103/PhysRevMaterials.5.124202. URL: <https://link.aps.org/doi/10.1103/PhysRevMaterials.5.124202>.
- [112] Alejandro Adem, Ali Nabi Duman, and José Manuel Gómez. “Cohomology of toroidal orbifold quotients”. In: *Journal of Algebra* 344.1 (2011), pp. 114–136. ISSN: 0021-8693. DOI: <https://doi.org/10.1016/j.jalgebra.2011.08.004>. URL: <https://www.sciencedirect.com/science/article/pii/S0021869311004443>.
- [113] George William Whitehead. *Elements of Homotopy Theory*. Graduate Texts in Mathematics. Springer, 2012. ISBN: 978-1-4612-6320-3. DOI: 10.1007/9781-4612-6318-0.
- [114] James F. Davis and P. Kirk. *Lecture Notes in Algebraic Topology*. Vol. 35. Graduate Studies in Mathematics. Providence, Rhode Island: American Mathematical Society, 2001. ISBN: 9781470420888 1470420880 978-0-8218-2160-2. URL: <https://bookstore.ams.org/gsm-35/>.
- [115] Faruk Abdulla. *Protected Weyl semimetals within 2D chiral classes*. 2024. arXiv: 2401.04656 [cond-mat.mes-hall]. URL: <https://arxiv.org/abs/2401.04656>.

- [116] Loring W. Tu. *Introductory Lectures on Equivariant Cohomology: (AMS-204)*. Princeton University Press, Mar. 2020. ISBN: 9780691191751. DOI: 10.23943/princeton/9780691191751.001.0001. URL: <https://doi.org/10.23943/princeton/9780691191751.001.0001>.
- [117] Graeme Segal. “Equivariant K-theory”. In: *Publications Mathématiques de l’IHÉS* 34 (Jan. 1968), pp. 129–151. DOI: 10.1007/BF02684593.
- [118] Theo Hahn, ed. *International Tables for Crystallography, Volume A: Space-Group Symmetry*. Dordrecht; London: Springer, 2002.
- [119] Louis Michel. “Fundamental concepts for the study of crystal symmetry”. In: *Physics Reports* 341.1 (2001). Symmetry, invariants, topology, pp. 265–336. ISSN: 0370-1573. DOI: [https://doi.org/10.1016/S0370-1573\(00\)00091-0](https://doi.org/10.1016/S0370-1573(00)00091-0). URL: <https://www.sciencedirect.com/science/article/pii/S0370157300000910>.
- [120] John W. Woll Jr. “One-Sided Surfaces and Orientability”. In: *The Two-Year College Mathematics Journal* 2.1 (1971), pp. 5–18. DOI: 10.1080/00494925.1971.11973990. URL: <https://www.tandfonline.com/doi/abs/10.1080/00494925.1971.11973990>.
- [121] Jeremy Karl Cockcroft. *A Hypertext Book of Crystallographic Space Group Diagrams and Tables*. 1999. URL: <http://img.chem.ucl.ac.uk/sgp/mainmenu.htm> (visited on 06/16/2025).
- [122] Taylor L. Hughes, Emil Prodan, and B. Andrei Bernevig. “Inversion-symmetric topological insulators”. In: *Phys. Rev. B* 83 (24 June 2011), p. 245132. DOI: 10.1103/PhysRevB.83.245132. URL: <https://link.aps.org/doi/10.1103/PhysRevB.83.245132>.
- [123] Ari M. Turner et al. “Quantized response and topology of magnetic insulators with inversion symmetry”. In: *Phys. Rev. B* 85 (16 Apr. 2012), p. 165120. DOI: 10.1103/PhysRevB.85.165120. URL: <https://link.aps.org/doi/10.1103/PhysRevB.85.165120>.
- [124] Yuan-Ming Lu and Dung-Hai Lee. *Inversion symmetry protected topological insulators and superconductors*. 2014. arXiv: 1403.5558 [cond-mat.mes-hall]. URL: <https://arxiv.org/abs/1403.5558>.
- [125] Ken Shiozaki and Masatoshi Sato. “Topology of crystalline insulators and superconductors”. In: *Phys. Rev. B* 90 (16 Oct. 2014), p. 165114. DOI: 10.1103/PhysRevB.90.165114. URL: <https://link.aps.org/doi/10.1103/PhysRevB.90.165114>.
- [126] Eslam Khalaf. “Higher-order topological insulators and superconductors protected by inversion symmetry”. In: *Phys. Rev. B* 97 (20 May 2018), p. 205136. DOI: 10.1103/PhysRevB.97.205136. URL: <https://link.aps.org/doi/10.1103/PhysRevB.97.205136>.

- [127] Samuel Peltier et al. “Computation of Homology Groups and Generators”. In: *Discrete Geometry for Computer Imagery*. Ed. by Eric Andres, Guillaume Damiand, and Pascal Lienhardt. Berlin, Heidelberg: Springer Berlin Heidelberg, 2005, pp. 195–205. ISBN: 978-3-540-31965-8. DOI: 10.1007/978-3-540-31965-8_19.
- [128] Marcus Stålhammar and Lukas Rødland. *Abelian Spectral Topology of Multifold Exceptional Points*. 2025. arXiv: 2412.15323 [cond-mat.mes-hall]. URL: <https://arxiv.org/abs/2412.15323>.
- [129] Meng Xiao et al. “Synthetic gauge flux and Weyl points in acoustic systems”. In: *Nature Physics* 11.11 (Nov. 2015), pp. 920–924. DOI: 10.1038/nphys3458.
- [130] Hao Ge et al. “Experimental Observation of Acoustic Weyl Points and Topological Surface States”. In: *Phys. Rev. Appl.* 10 (1 July 2018), p. 014017. DOI: 10.1103/PhysRevApplied.10.014017.
- [131] Qiang Wang et al. “Vortex states in an acoustic Weyl crystal with a topological lattice defect”. In: *Nature Communications* 12.1 (June 2021), p. 3654. DOI: 10.1038/s41467-021-23963-7.
- [132] Meng Xiao et al. “Experimental demonstration of acoustic semimetal with topologically charged nodal surface”. In: *Science Advances* 6.8 (2020), eaav2360. DOI: 10.1126/sciadv.aav2360. URL: <https://www.science.org/doi/abs/10.1126/sciadv.aav2360>.